Model-driven registration for multi-parametric renal MRI.

Fotios Tagkalakis

Submitted in accordance with the requirements for the degree of

Master of Science by Research

University of Leeds

Biomedical Imaging Sciences Department,

Faculty of Medicine & Health

29 / 01 / 2021

Supervisors

Prof. Steven Sourbron

Dr. Kanishka Sharma

Prof. Sven Plein

UNIVERSITY OF LEEDS

The candidate confirms that the work submitted is his own and that appropriate credit has been given where reference has been made to the work of others.

Acknowledgements

I would like to take this opportunity to first and foremost thank God for giving me strength and keeping me and my loved ones safe, especially during the pandemic of covid-19, which coincided with the writing of this thesis.

My gratitude goes to Professor Steven Sourbron for giving me the opportunity to pursue my research under his guidance, support and assistance. I would also like to thank Dr. Kanishka Sharma for the help, advice and mentoring that she provided to me, during my attempt. My thanks also go to Professor Sven Plein for his overall supervision. Special thanks to Dr. John Huntriss for his advice, guidance and willingness to help me throughout the whole project. My warm thanks to Peter Thelwall, Dr. Jehill Parikh and Professor Neil Sheerin (from the Newcastle University) and Professor Patrick Mark and Dr. Alexandra Radjenovic (from the Glasgow University) for providing me the Dynamic Contrast Enhanced MRI datasets used to perform the experiments presented in chapter 3. I would also like to thank: Dr. Irvin Tech and Dr. Christopher Kelly for their assistance with the Diffusion Tensor Imaging experiments and for their useful pieces of advice, Bashair AlHummiany for kindly providing me the arterial input functions for the Dynamic Contrast Enhanced MRI experiments presented in chapter 4 and Dr. Susmita Basak for all her assistance and useful advice. I am also grateful to the BEAt-DKD for their assistance and support.

On a personal note, I would like to thank first and foremost from the bottom of my heart Konstantina for always being on my side, supporting me and having faith in me. Also, I want to thank all of my friends for always being there, assisting and encouraging me. Finally, I would like to express my gratitude to my beloved family for the love and support that they have shown to me. I consider myself extremely fortunate to have such a great group of people in my life.

Abstract

The use of MR imaging biomarkers is a promising technique that may assist towards faster prognosis and more accurate diagnosis of diseases like diabetic kidney disease (DKD). The quantification of MR Imaging renal biomarkers from multiparametric MRI is a process that requires a physiological model to be fitted on the data. This process can provide accurate estimates only under the assumption that there is pixel-to-pixel correspondence between images acquired over different time points. However, this is rarely the case due to motion artifacts (breathing, involuntary muscle relaxation) introduced during the acquisition. Hence, it is of vital importance for a biomarkers quantification pipeline to include a motion correction step in order to properly align the images and enable a more accurate parameter estimation. This study aims in testing whether a Model Driven Registration (MDR), which integrates physiological models in the registration process itself, can serve as a universal solution for the registration of multiparametric renal MRI. MDR is compared with a state-of-the-art model-free motion correction approach for multiparametric MRI, that minimizes a Principal Components Analysis based metric, performing a group-wise registration. The results of the two methods are compared on T1, DTI and DCE-MRI data for a small cohort of 10 DKD patients, obtained from BEAt-DKD project's digital database. The majority of the evaluation metrics used to compare the two methods indicated that MDR achieved better registration results, while requiring significantly lower computational times. In conclusion, MDR could be considered as the method of choice for motion correction of multiparametric quantitative renal MRI.

Table of Contents

Abbreviations

2CFM	Two-Compartment Filtration Model
2D	Two-Dimensional
3D	Three-Dimensional
ADC	Apparent Diffusion Coefficient
ADPKD	Autosomal Dominant Polycystic Kidney Disease
AIF	Arterial Input Function
AIR	Automated image registration (toolbox)
ANTS	Advanced Normalization Tools (toolbox)
ASGD	Adaptive Stochastic Gradient Descent
ASL	Arterial Spin Labelling
BEAt-DKD	Biomarker Enterprise to Attack Diabetic Kidney Disease
BOLD	Blood Oxygenation Level Dependent
CKD	Chronic Kidney Disease
CMD	Cortico-Medullary Differentiation
CNN	Convolutional Neural Network
CPU	Central processing Unit
CS	Chi-squared error
CT	Computed Tomography
CV	Coefficient of Variation
DCE	Dynamic Contrast Enhanced
DKD	Diabetic Kidney Disease
DMD	Dynamic Mode Decomposition
DOF	Degrees of Freedom
DTI	Diffusion Tensor Imaging
DWI	Diffusion Weighted Imaging
ECG	Electrocardiography
eGFR	Estimated Glomerular Filtration Rate
EPI	Echo Planar Imaging
ESRD	End Stage Renal Disease
FA	Fractional Anisotropy
FCN	Fully Convolutional Neural Network
FFD	Free Form Deformation
FID	Free Induction Decay
FLASH	Fast Low Angle Snapshot, Siemens rapid gradient echo sequence using a small flip angle and short TR.
Gd	Gadolinium

GD	Gradient Descent
GFR	Glomerular Filtration Rate
GRASP	Golden-Angle Radial Sparse Parallel
IQR	Interquartile Range
IQR	Interquartile Range
IR	Inversion Recovery
ITK	Insight Segmentation and Registration Toolkit (toolbox)
LL	Look-Locker
MDR	Model-Driven Registration
MEM	Maximum Enhancement Map
MFR	Model-Free Registration
MI	Mutual Information
MOLLI	Modified Look-Locker pulse sequence
MR	Magnetic Resonance
MRF	Markov Random Field
MRI	Magnetic Resonance Imaging
MT	Magnetization Transfer
NMI	Normalized Mutual Information
NMR	Nuclear Magnetic Resonance
PCA	Principal Components Analysis
PET	Posiron Emission Tomography
RBF	Renal Blood Flow
RF	Radio Frequency
ROI	Region of Interest
SGD	Stochastic Gradient Descent
SIFT	Scale-Invariant Feature Transform
SNR	Signal-to-Noise Ratio
SPM	Statistical Parametric Mapping (toolbox)
STD	Standard Deviation
SURF	Speeded Up Robust Features
TE	Echo Time
TR	Repetition Time
Turbo FLASH	FLASH sequence with magnetization preparation.
VIBE	Volume Interpolated Body Examination, fast breath-hold sequence used in the abdomen.
VOI	Volume of Interest

List of Figures

List of Tables

Chapter 1

Introduction

1.1 Context and problem statement

Valuable information regarding hemodynamics, morphology, microstructure and metabolic changes in the kidneys can be described non-invasively via the quantification of MR imaging biomarkers. For this reason MRI biomarkers are speculated to be able to assist in earlier prognosis, more accurate diagnosis or personalized therapy decisions, for a variety of renal diseases like Chronic Kidney Disease (CKD) and Diabetic Kidney Disease (DKD)[1]. The biomarkers quantification usually requires a physiological model-fitting process on the acquired data. The estimated values are measured in physical units and can be used to perform comparisons, among subjects or between different tissue regions, that may reveal even subtle changes caused by the progression of a disease.

The model-fitting process required to extract MR imaging biomarkers assumes that there is pixel-to-pixel correspondence between images that are acquired over different time points. However, this assumption rarely applies for renal MRI due to organs' motion caused by a number of factors including respiration, digestion or involuntary muscle relaxation, which introduce errors in the parameters' estimation process. Therefore, motion correction techniques need to be applied before the model fitting process in order to properly align the images and enable a precise and robust quantification of MR imaging biomarkers.

This thesis will examine registration methods that could be applied on multiparametric quantitative renal MRI to support the BEAt-DKD project[2], which is a large EU-wide collaboration with academic and industry partners aiming to develop better diagnostics for DKD. More specifically, iBEAT study[3] will process the motion corrected data in order to extract more accurate MR imaging biomarkers and test whether they can detect changes in kidney's anatomy and function early enough to improve the prediction of disease progression. The study began in 2018 and will ultimately collect data from 500 early DKD patients, with type-2 diabetes.

1.2 Thesis aim

The aim of this thesis is to compare model-driven registration (MDR) against a state-of-the art model-free registration method in the context of multiparametric quantitative renal MRI. The two registration methods will be compared on: breath-hold T1-mapping and free-breathing Diffusion Tensor Imaging (DTI) and Dynamic Contrast Enhanced (DCE) renal MRI data, from DKD patients with type 2 diabetes collected by the iBEAt-study. Additionally, this study aims to provide support to the hypothesis that MDR is a suitable candidate for universal motion correction of quantitative MRI.

1.3 Overview

This paragraph provides a brief summary of the chapters of this thesis.

Chapter 2: Provides some background information regarding the Diabetic Kidney Disease (DKD), since the image registration methods considered in this study will be applied on renal MRI data acquired from DKD patients. The chapter also covers the basics of MRI (MR physics, pulse sequences) and the acquisition protocols used to acquire the data.

Chapter 3: Consists of a background section with the basic components for medical image registration, a brief description of the elastix[4] medical image registration toolbox (used to conduct all the registration experiments presented in this thesis) and finally a literature review on registration methods for MRI.

Chapter 4: Presents a short pilot study in which an initial implementation of MDR (with the use of elastix[4] and Python) was applied on renal DCE-MRI data of healthy volunteers. This initial study revealed soft spots of the method and helped determine all the necessary requirements for a more robust version of MDR presented in the next chapter.

Chapter 5: In this chapter a comparison between an enhanced version of MDR and a model-free registration takes place to test which method performs better as a universal solution for the registration of quantitative renal MRI. The experiments conducted have registered the middle slice for T1, Diffusion Tensor Imaging (DTI) and DCE MRI acquisitions from 10 DKD patients (diabetes type-2). Statistical analysis was performed on a set of registration evaluation metrics in order to conclude which method performs better.

Chapter 6: The thesis is concluded with a brief summary and a few suggestions for future research.

Chapter 2

Background on renal MRI

2.1 Renal anatomy and Diabetic Kidney Disease (DKD)

The kidneys are paired retroperitoneal organs constituting the basic urine excretory system of the human body[5]. More specifically, kidneys assist in the excretion of nitrogenous waste from the blood, keeping the water and electrolyte balance of the body. Filtration and reabsorption of blood are the two main functions of the kidneys. Healthy kidneys filter about a half cup of blood every minute. Blood enters the kidney from the abdominal aorta that branches into left and right renal arteries, afterwards it is directed towards the glomerulus of the kidneys where the process of filtration takes place. During the filtration process the kidneys are capable of keeping nutrients (salts, glucose) while expelling excess nutrients, water and wastes (urea, ammonia) out of the organism.

Human kidneys are located in the posterior region of the abdominal cavity on the right and left side of the spinal cord. The right kidney is usually a bit more caudal than the left one. The shape of the kidneys follows a bean-structure having a convex border on the outside and a concave border at the renal hilum. The median volumes for the left and right kidneys are 146 cm^3 and 134 cm^3. The range of kidneys' thickness spans from 2.5 to 3.0 cm, the width from 5.0 to 7.0 cm and the length from 11 to 12 cm[6]. Each kidney consists of a peripheral cortex and the renal medulla, which is constituted by multiple cone-shaped tissues called pyramids (Fig.1). The tip of each pyramid converges near the center of the kidney into the area known as calyx, while the areas between the renal pyramids are called renal columns and they are projections of the cortex. The structural and functional unit of the kidneys is the nephron, each human adult kidney contains around one million nephrons. Nephrons span the cortex and medulla and are responsible for the production of urine. The urine is collected in the renal pelvis and then flows through the ureter into the bladder.

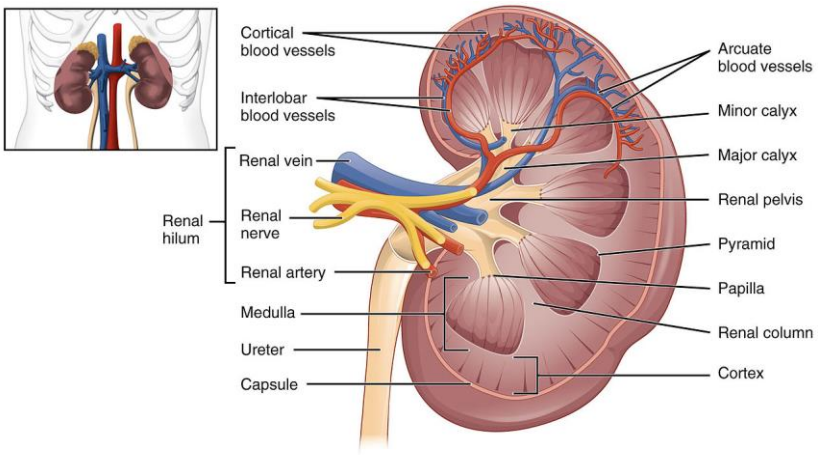

Figure 1: Normal kidney anatomy. Cross section of a kidney (Image Courtesy of: cnx.org/content/col11496/1.6/)

Diabetes is currently the most common cause of both chronic kidney disease (CKD) and end-stage renal disease (ESRD) for the majority of countries around the world[7]. Both types of diabetes (1 and 2), can lead to CKD and ESRD. Diabetic kidney disease (DKD) is currently the most common form of CKD, affecting more than 10% of global population. DKD is a degenerative disease, patients suffering from DKD face high mortality rates which surpass most types of cancer. The microvascular complication that leads to DKD develops in 30% of type 1 diabetics and approximately 40% of type 2 diabetics[8]. For both types of diabetes one of the primary causes of DKD is the chronic hyperglycemia, in type 1 hyperglycemia starts in the first decades of life while in type 2 it starts after forties, when kidneys have already been affected by ageing and other promoters of chronic renal injury (i.e. arterial hypertension, obesity, smoking). The possible combinations of the aforementioned factors indicate that especially for type 2 diabetics, DKD is a disease sustained by different mechanisms[9]. Pure glomerulopathy is more frequent for patients with earlier onset of diabetes, while vascular and tubular changes are more common among older patients with macroalbuminuria, renal insufficiency and hypertension. Due to this heterogeneity of patterns for renal diseases, type 1 and type 2 diabetics are usually studied separately. For the context of this study the focus will be on type 2 diabetics, which is also the particular type that has increased more over the last years.

Currently, there are no effective means to prevent or cure DKD[2]. The screening process for DKD is based on micro-/macroalbuminuria measurements in addition to the decline in glomerular filtration rate (GFR or eGFR), which are often inaccurate and fail to be detected in early stage patients. Patients are clinically diagnosed with DKD when they have high urinary albumin to creatinine ratio ≥30 mg/g and/or sustained a reduction in eGFR bellow 60 ml/min per 1.73 m^2. The development of DKD alternates the structures of kidney compartments, with the earliest consistent change to be the thickening of the glomerular basement membrane.

The development of novel treatment options requires better understanding of the pathways which lead to DKD and better biomarkers which will be able to reveal significant details assisting in monitoring disease progression. MRI is hypothesized to extract imaging biomarkers that improve the prognosis[1] of both CKD and DKD, in particular the prediction of functional decline and the differentiation of fast from slow progressors. Hence, it is important to establish efficient and robust image processing pipelines that will discover well-hidden relationships inside complex image data and correlate them towards a standardized quantification of MR imaging biomarkers for prognosis, diagnosis and personalized monitoring of DKD.

2.2 The iBEAt study: prognostic MRI biomarkers for DKD

Preliminary studies indicate that MR imaging biomarkers can identify underlying problems in DKD (i.e. blood supply, oxygen supply, kidney scarring and kidney function) possibly more accurately than the alternatives currently available. In this context, iBEAT study[3] aims to provide insights as regards to the progression and heterogeneity of DKD developing a more personalized approach possibly based on such MR imaging biomarkers for the management of DKD patients with type 2 diabetes. Hence, the multi-parametric iBEAt MRI protocol was developed, aiming towards the identification of imaging biomarkers for improved prognosis and prediction. The iBEAt MRI protocol is summarized in Table.1 and below follow a few indicative examples of the MRI sequences acquired and their respective biomarkers:

Recent literature claims close correlation of abdominal fat with DKD[10]. In iBEAt protocol visceral fat volume was measured with T_1-weighted DIXON as a biomarker related to the body composition.

Kidney hypertrophy following primary or secondary hyperfiltration is associated with poorer outcomes for diabetic patients[11-13]. Thus, T_1-weighted sequences with high in-plane and slice resolution were acquired in order to quantify the kidney volume, cortical volume and cortical thickness.

Recently magnetic resonance relaxometry and more specifically the measurement of the independent quantitative magnetic resonance relaxation times T_1 and T_2 have been shown to provide non-invasive information regarding renal structure and function not only in healthy but also Acute Kidney Injury CKD, renal transplant and Autosomal Dominant Polycystic Kidney Disease (ADPKD) patients[14]. T_1 shows a cortico-medullary differentiation (CMD), which is correlated to the renal function. T_2 measurements have shown increased values for early-stage ADPKD patients compared to healthy subjects while it could also be used to assess AKI in the context of ischemia perfusion injury. The iBEAt MRI protocol acquires an inversion recovery based Look Locker T_1 mapping sequence and a Spin Echo prepared Gradient Echo T_2 mapping sequence for measuring the cortical and medullary T_1 and T_2 values, respectively.

BOLD MRI provides useful information regarding the delivery of oxygenated blood to the renal parenchyma, based on the magnetic field variations between blood vessels and the tissue surrounding them[15]. BOLD is quantified depending on the transverse relaxivity rate ($R_2^*=1/T_2^*$). The extracted biomarker is the renal tissue oxygenation which may reveal aspects of renal dysfunction non-invasively[16, 17].

Diffusion weighted imaging (DWI) can detect and quantify water molecules' movement in kidney tissues, while DTI is a more comprehensive technique that also evaluates the fractional anisotropy (FA, directionality of water mobility) and ADC (its magnitude)[15, 18, 19]. Hence these sequences could serve to provide information regarding the kidney tissue (i.e. renal microstructure, fibrosis, inflammation). It has been shown[20] that the reduction of ADC and FA values correlates with decreased renal function in several renal diseases (i.e. CKD). Moreover, a number of studies[21-24] indicate that the ADC values are correlated with the histological measurements of kidney fibrosis, for CKD patients.

Phase contrast MRI[25] is based on the properties of moving versus static protons in a magnetic field and it can quantify the blood flow in renal arteries. Hence, biomarkers corresponding to the systemic hemodynamics of the kidney renal arteries (i.e. renal artery blood flow (flux), renal artery velocity) can be extracted.

Magnetization Transfer (MT) MRI provides information regarding the presence of macromolecules, offering a non-invasive tool to probe renal fibrosis[26]. A recent study examined a group of renal impaired patient and showcased that the mean MT ratio of the renal cortex is significantly higher in patients with decreased eGFR than in patients with normal renal function[27].

Arterial Spin Labeling MRI utilizes endogenous water as a tracer, however it has a limited signal-to-noise-ratio, hence it requires multiple measurements to allow data averaging. ASL has been demonstrated to provide information regarding the renal perfusion non-invasively, without the use of injected contrast, not only for healthy subjects but also for CKD patients[28].

Finally, DCE MRI provides information regarding the renal perfusion and renal vasculature[18]. Performing kinetic analysis allows the quantification of: renal blood flow, plasma and tubular mean transit times, GFR and renal blood volume. Hence, DCE can provide information describing the filtration of the kidneys. The aforementioned measurements have already been used as biomarkers assisting the diagnosis of several renal diseases including renovascular hypertension and renal transplants[15].

Category	MRI Sequence	Biomarker	Unit
Body composition	T1w-DIXON	Visceral Fat Volume	mL
Body composition	Multi-Echo 2D T_2*	Pancreatic Fat Fraction	%
Body composition	Multi-Echo 2D T_2*	Liver Fat Fraction	%
Body composition	Multi-Echo 2D T_2*	Liver Iron Content	mg/mL
Kidney Morphology	T1w-DIXON	Renal Sinus Fat Volume	mL
Kidney Morphology	T1w-DIXON	Parenchymal Volume	mL
Kidney Morphology	T1w- Spoiled Gradient Echo	Cortical Volume	mL
Kidney Morphology	T1w- Spoiled Gradient Echo	Cortical Thickness	mm
Kidney Morphology	Post-Contrast T1w-DIXON	Pelvis Volume	mL
Tissue (fibrosis)	IR-Prepared Look Locker	Longitudinal Relaxation Time (T_1)	ms
Tissue (fibrosis)	Spoiled Gradient Echo MT	Magnetisation Transfer Ratio (MTR)	%
Tissue (inflammation)	Spin-echo Prepared Gradient Echo	Transverse Relaxation Time (T_2)	ms
Tissue (oxygenation)	Multi-Echo 2D T_2*	Effective Transverse Relaxation Time (T_2*)	ms
Tissue (microstructure)	Spin Echo EPI DWI	Apparent Diffusion Coefficient (ADC)	mm^2/s
Tissue (microstructure)	Spin Echo EPI DTI	Fractional Anisotropy (FA)	%
Hemodynamics	Phase Contrast Imaging	Renal Artery Blood Velocity - Mean	cm/s
Hemodynamics	Phase Contrast Imaging	Renal Artery Blood Velocity - Diastolic	cm/s
Hemodynamics	Phase Contrast Imaging	Renal Artery Blood Velocity - Systolic	cm/s
Hemodynamics	Phase Contrast Imaging	Renal Artery Blood Flow	mL/min
Hemodynamics	Arterial Spin Labelling	Cortical Perfusion (RBF)	mL/min/100g
Hemodynamics	DCE MRI	Blood Volume Fraction	%
Filtration	DCE MRI	Single-Kidney GFR	mL/min/m2
Filtration	DCE MRI	Filtration Fraction	%
Filtration	DCE MRI	GFR Density	mL/min/100g
Filtration	DCE MRI	Tubular Volume Fraction	%
Filtration	DCE MRI	Tubular Transit Time	min

Table 1: iBEAt study MR imaging biomarkers. Prognostic imaging biomarkers of body composition, renal morphology and tissue structure, hemodynamics and filtration extracted from each MRI sequence within the study.

2.3 Background on MRI

2.3.1 MRI Basics

MRI is a non-invasive highly informative medical imaging technique, that is based on the principle of nuclear magnetic resonance (NMR). NMR is a physical phenomenon that takes place when certain nuclei interact with an external magnetic field and it could be described as the analogous of the precessional motion of a tilted spinning top around the gravitational field. The most widely used nucleus in MRI is hydrogen (^{1}H), which consists of a single proton. The hydrogen nuclei exist in abundance in biological organisms (water and fat) and they possess an intrinsic property nuclear angular momentum (spin). Spin resembles the classical angular momentum, but it can obtain only discrete quantized values. When no external magnetic field is applied the orientation of the spins is random, resulting in a net magnetic moment equal to zero. While in the presence of a static magnetic field $\boldsymbol{B_0}$ (i.e. MRI scanner) the NMR precession phenomenon takes place. More specifically, the interactions of $\boldsymbol{B_0}$ with the spins produces a torque (perpendicular to the magnetic field), which leads to the precession of the spins around the direction of the field. The precession frequency is described by the Larmor equation: $\omega_0 = \gamma\, B_0$, where γ is a constant called the gyromagnetic ratio.

Excitation:

In the presence of an external magnetic field $\boldsymbol{B_0}$ (typically applied at the z/ longitudinal direction, Fig.2), the spins exhibit a slight preference towards precessing in a direction parallel to $\boldsymbol{B_0}$ rather than antiparallel. The reason is that parallel alignment leads to lower energy states than the antiparallel. This

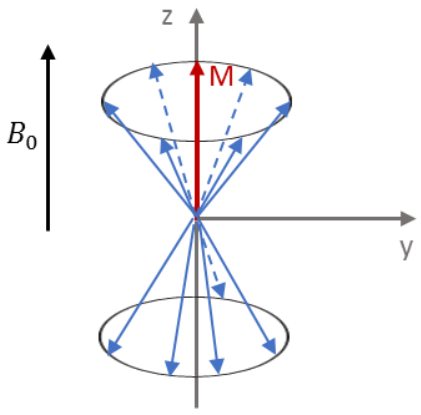

Figure 2: Spins under the influence of the external magnetic field $\mathbf{B_0}$ precessing with random phases. Due to the lack of phase coherence there is no measurable transverse magnetization. There is a slight preference for the spins to align in parallel to $\mathbf{B_0}$ since this is the lowest energy state.

slight difference creates the net magnetization $\boldsymbol{M}$ parallel to the direction of the field, which is still not directly measurable. This is because spins precess with random phases, failing to create a measurable transverse (xy-plane) magnetization (Fig.2).

A measurable NMR signal is generated when the net magnetization (or at least a fraction of it) gets tipped from the z axis into the transverse (xy) plane. This is achieved by an RF (radiofrequency) pulse, which is the application of an oscillating (at the Larmor frequency) magnetic field $\boldsymbol{B_1}$ perpendicular to $\boldsymbol{B_0}$. When $\boldsymbol{B_1}$ is applied the net magnetization $\boldsymbol{M}$ precess about the z-axis (Fig.3), leading a component of the net magnetization previously on the z-axis $\boldsymbol{M_z}$ to tip into the transverse plane and create a measurable transversal magnetization $\boldsymbol{M_{xy}}$. A suitably chosen RF pulse can fully rotate the net magnetization from the z plane to the transversal plane, this RF pulse in known as 90^o RF pulse (the angle of rotation for the net magnetization is known as the flip angle).

Relaxation:

Once the magnetization vector $\boldsymbol{M}$ is tipped to the transversal plane, the process of relaxation begins and the transverse magnetization fades leading the MR signal to fade as well. There are two main causes that

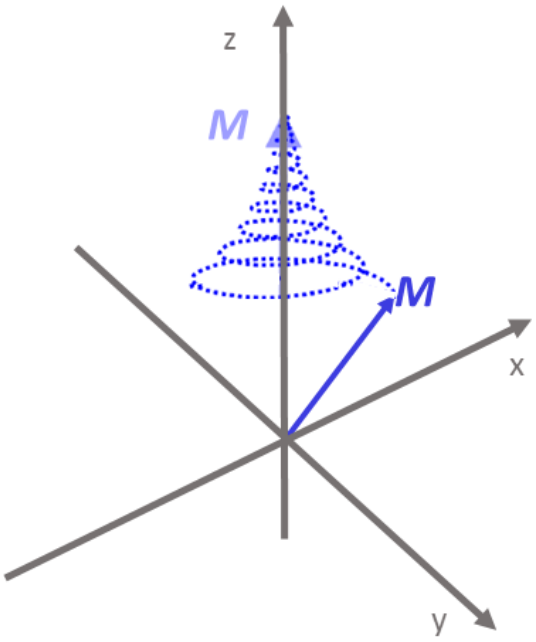

Figure 3: Precesion of the net magnetization M around the z-axis while tipping to the transversal plane.

reduce the transverse magnetization leading the system back to the stable state: the spin-lattice interactions and the spin-spin interactions.

T_1/ *Longitudinal Relaxation:*

After an excitation (application of an RF pulse) the transverse magnetization $\boldsymbol{M_{xy}}$ decays, while the magnetic moments realign gradually to the main magnetic field ($\boldsymbol{B_0}$, z-axis) restoring the longitudinal magnetization $\boldsymbol{M_z}$ (Fig.4). The rate at which the nuclei dissipate energy (in the form of heat) is characterized by the T_1 spin-lattice (or longitudinal) relaxation time. Practically, T_1 relaxation time is the time needed for $\boldsymbol{M_z}$ to reach to 63% of $\boldsymbol{M}$ following the application of a 90° RF pulse. The time constant T_1 depends (among other factors) on the strength of the external magnetic field $\boldsymbol{B_0}$ and the specific properties of the type of the tissue examined (i.e. type of nuclei etc).

T_2/ *Transverse Relaxation:*

This type of relaxation refers to the loss of phase coherence of the spins (the individual magnetization vectors start to cancel each other), which results in the decay of the transverse magnetization $\boldsymbol{M_{xy}}$. Spins exhibit differences in their resonant frequencies due to the small magnetic fields from their proximal spins which combined with the tendency of the spins to be equally distributed in space lead to spin dephasing (Fig.5).

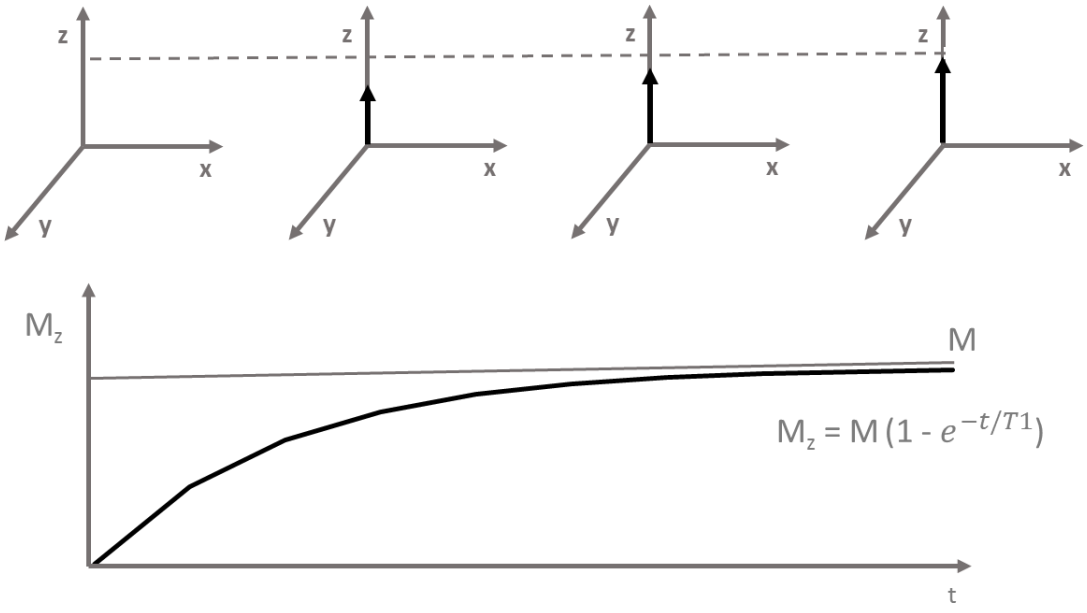

Figure 4: T1/ Longitudinal relaxation modelled as exponential growth curve of the longitudinal magnetization M_z.

The rate of the dephasing is described by the decay constant T_2 also known as spin-spin (or transverse) relaxation time. However, apart from the spin-spin interactions described by the T_2 relaxation time, in practice there are inhomogeneities of the external magnetic $\boldsymbol{B_0}$ that also affect the $\boldsymbol{M_{xy}}$ decay, these effects are described by a separate term T'_2. The combined effects of the aforementioned define the apparent transverse relaxation time T_2* (Fig.5) as follows: $\frac{1}{T_2^*} = \frac{1}{T_2} + \frac{1}{T_2'}$. The term free induction decay (FID) refers to the decay of the MR signal due to T_2* effects.

Slice Selection:

In MRI it is desirable to achieve selective slice excitation, to do that a magnetic field gradient (G_{SS}) is applied in the z-direction (Fig.6) making the magnetic field inhomogeneous in a linear fashion for z-direction. Hence, the Larmor frequencies for the spins are different along the z-axis and each slice has its own frequency. This way the application of an RF pulse that matches a slice's frequency excites protons exclusively within the chosen slice. Right after the slice selection gradient an additional gradient of opposite polarity known as rephasing gradient is used to compensate for the phase dispersion caused by the main slice selection gradient.

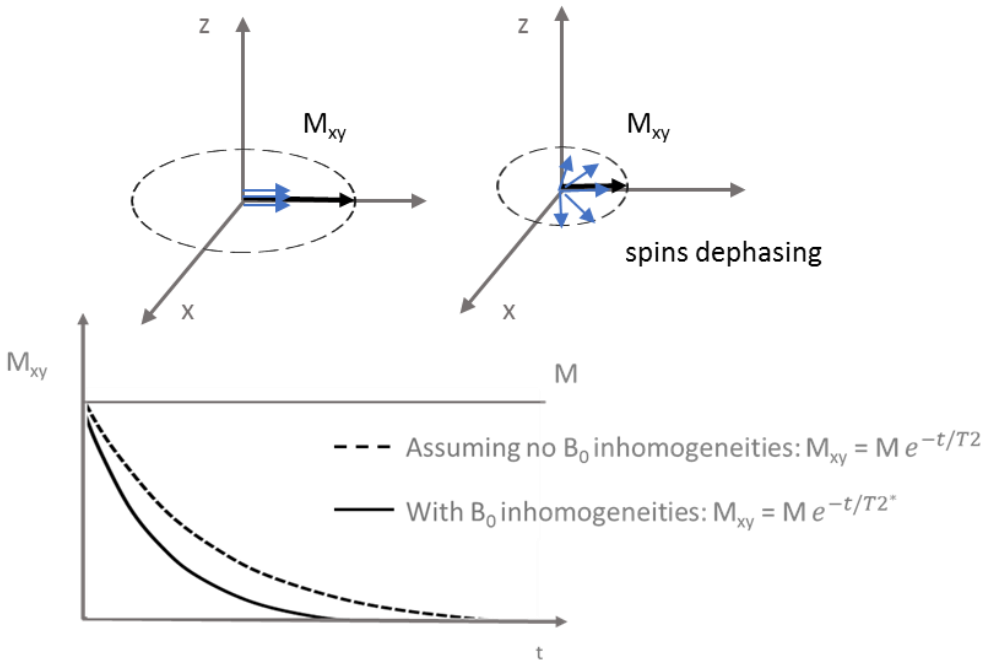

Figure 5: T2/ transverse relaxation modelled as the exponential decay of the transverse magnetization M_{xy}.

Spatial Encoding:

After the selection of a certain slice, with the application of the slice select gradient (G_{SS}) it remains to identify the exact in-plane position within the slice, which is accomplished by the process of spatial encoding which is based on phase encoding and frequency encoding.

The phase encoding step takes place first and requires the application of a phase encoding gradient (typically along the y-direction for the coordinate system of Fig.6) for a short period of time. During this time the phase encoding gradient modifies the precession speed of the proton spins leading to dephasing. Once the gradient is switched off, the spins return to their original precession frequency, but they keep their phase offset (they are either ahead or behind in phase, relative to their previous state). Hence, phase varies along y-axis in a linear fashion and each line in the xy plane can be identified by its unique phase. The aforementioned process is repeated with varying gradient strength obtaining measurements for different phase encodings to allow the derivation of the required spatial information.

The second step is the frequency encoding which requires the application of a frequency gradient (typically along the x-direction for the coordinate system of Fig.6). The application of the frequency gradient results in spins precessing at a frequency that depends on the summation of the external magnetic field $\boldsymbol{B_0}$ and the gradient magnetic field that they experience, with the later one depending on the spins location along the x-axis.

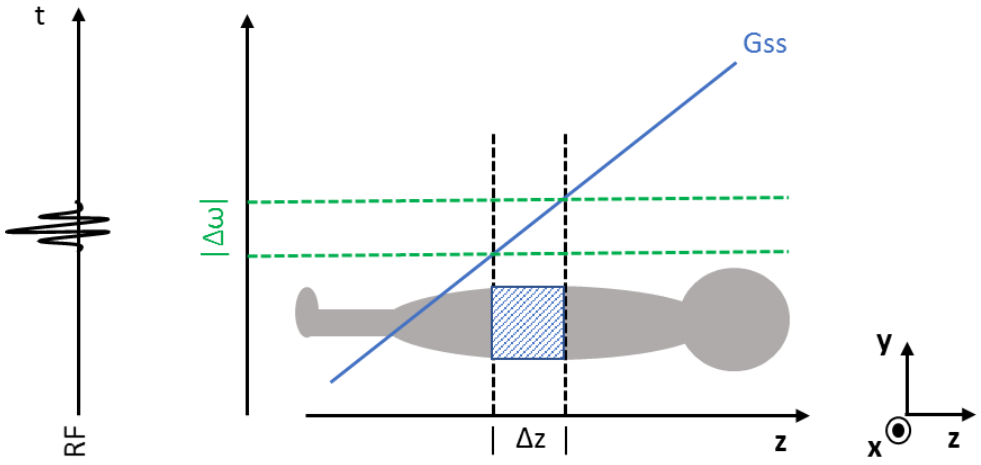

Figure 6: Slice selection with the use of an RF pulse. The frequency range Δω allows only for the spins from a certain slice with thickness Δz to get excited when the slice selection gradient G_{SS} gets activated.

2.3.2 Basic MR sequences

Bellow follows a brief summary of basic MR sequences that form the basis for the acquisition schemes utilized to acquire the T1, DTI and DCE-MRI data included in this study.

Spin Echo:

A spin echo sequence begins with a 90° RF excitation pulse[29], which tips the net magnetization in the transversal plane. Right after that the spins begin to diphase due to spin-spin interactions and inherent magnetic field inhomogeneities (T_2* decay of the FID generated signal). At half the echo time (TE/2) after the 90° pulse, an RF pulse of 180° is applied, this pulse inverts the spin dephasing and creates an echo. More specifically, the 180° RF pulse rotates the dephasing protons so that they continue precessing in the same direction and finally refocus (at TE time after the 90° RF pulse) to create an echo. Due to the fact that the 180° RF pulse compensates for the T_2* effects, a SE can provide "true" T_2 measurements. The time delay between two successive 90° RF pulses is known as the repetition time (TR).

In classic spin echo the process described above is repeated as many times as the number of the required lines of the k-space, which is very time consuming. For this reason, there are several techniques that choose to acquire multiple lines of the k-space, to achieve that they apply an 180° RF pulse at mutliples of the TE after the first 180° RF pulse to generate new echoes and allow the acquisition of more data.

Gradient echo:

Gradient echo sequences[30] does not rely on a second RF pulse to cause rephrasing of the spins, instead the polarity of the readout gradient is inversed in order to rephrase the spins. A gradient echo sequence begins with an α° pulse where α<90° (partial flip angle). A flip angle lower than 90° decreases the amount of the magnetization tipped to the transverse plane M_{xy}. Lower flip angle excitation leads to faster recovery of longitudinal magnetization M_z that allows shorter TR and TE, hence it decreases the scan time.

More specifically, in a gradient echo sequence the FID signal undergoes an accelerated dephasing as a dephasing gradient gets activated right after the a° RF pulse, this gradient causes a calibrated change in the local magnetic fields and alters the resonance frequencies slightly across the specimen. Next a rephrasing gradient is applied with the same strength but opposite polarity to the dephasing gradient, reversing the dephasing to create the echo. It is worth mentioning that since there is no 180° RF in the sequence to compensate for the T_2* effects the signal obtained is T_2*-weighted rather than T_2-weighted.

2.3.3 T1-weighted MRI

The acquisition of T_1-weigted images for this study was performed with the use of an Inversion Recovery Look-Locker (LL) pulse sequence. T1-weighted acquired images contain information regarding the time needed for the longitudinal Magnetization (M_z) to recover from its shift to the transversal plane after an RF excitation. For this study T1-maps were extracted from the T1-weighted acquisitions. T1-maps are biomarkers indicative of the cortico-medullary differentiation, which is correlated to the renal function.

Inversion recovery Look-Locker (LL):

T1-weighted images can be produced with several pulses, however regardless of the sequence specifics the basic idea is always the same: initially the spins are aligned to an external field ($\boldsymbol{B_0}$) then an RF pulse shifts them to the transverse plane creating transversal magnetization $\boldsymbol{M_{xy}}$. Following that, the transversal magnetization gradually dephases as a result of both the magnetic field inhomogeneities and the spin-spin interactions (T_2* decay) while the longitudinal magnetization $\boldsymbol{M_z}$ gets restored. Nevertheless, not all tissues return back to equilibrium simultaneously, hence the tissue's T_1 reflects the amount of time the spins need to realign with B_0. For example, fat realigns its magnetization with $\boldsymbol{B_0}$ quickly (short T_1) therefore it appears bright on T_1-weighted images, on the other hand water molecules realign much slower (long T_1) emitting weaker signals and hence appearing dark.

An inversion-recovery based pulse sequence begins with an 180˚ RF pulse in order to shift the longitudinal magnetization M_z to the transversal plain, then images are acquired at different time points (different inversion times, TI) along the T_1 recovery-curve. The inversion recovery Lock-Locker (LL) sequence is consisted of an inversion pulse followed by a series of gradient echo readouts, this technique formed the basis for inversion-recovery T_1 mapping[31]. In LL the next inversion recovery pulse is applied after 5* T_1, to reassure that the recovery of $\boldsymbol{M_z}$ has been completed.

T1 model-fitting:

Given that the acquired images are sorted according to each respective accumulative time from inversion *t* the following mono-exponential signal model gets fitted [32] pixel wise:

$$S(t) = A - B * e^{-\frac{t}{T_1^*}} \quad (2.1)$$

where *S* denotes the signal intensity, *A* represents the scaling factor of the signal intensity, *B* indicates the saturation efficiency and T_1^* is the apparent longitudinal relaxation time. Once the aforementioned mono-

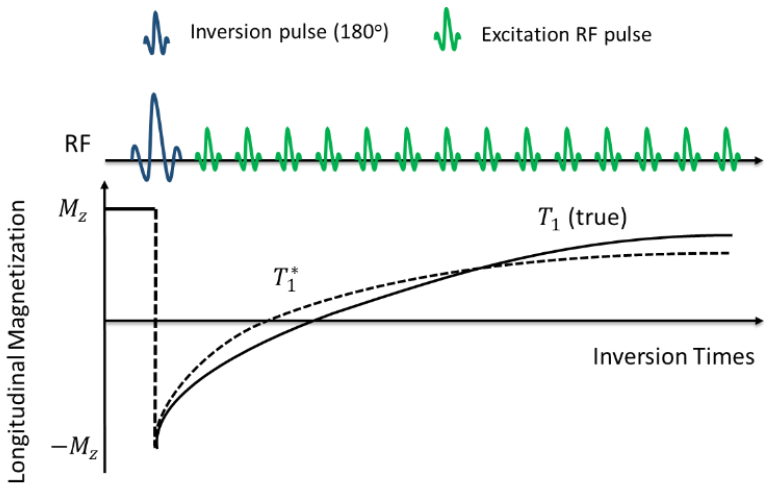

Figure 7: Comparison of the longitudinal magnetization M_z with classic single-point IR (true T1) and with Look-Locker (LL) IR (T1*).

exponential model fit is performed, the wanted is to measure the actual T_1 from the T_1^*. The LL method introduced a more time efficient way of measuring T_1 based on a continuous and periodic train of RF pulses after inversion pulse. However, for the LL method the recovery of the longitudinal magnetization $\boldsymbol{M_z}$ depends upon a number of factors including tissue characteristics, flip angle and field strength leading to a faster recovery to steady-state in comparison to the undisturbed equilibrium magnetization [33] (Fig.7).

$$T_1 = T_1^* * \left(\frac{B}{A} - 1\right) \tag{2.2}$$

The aforementioned correction is necessary to quantify the T1 map as accurately as possible. A typical fit on unregistered data is shown in Fig.8.

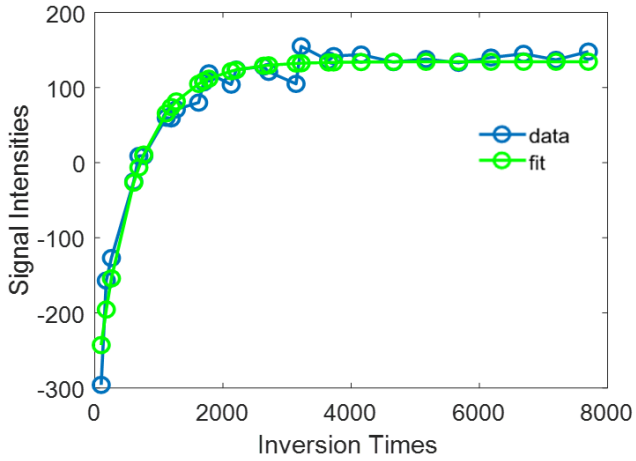

Figure 8: Indicative T1-fit for a single pixel before registration.

2.3.4 Diffusion Tensor Imaging (DTI) MRI

A Spin Echo Echo Planar Imaging (EPI) pulse sequence[34] was utilized for the acquisition of Diffusion Tensor Imaging (DTI) data for this study. DTI is a technique based on the measurement of the diffusion of water molecules which is utilized to measure diffusivity (/coefficient of diffusion). The imaging biomarker extracted from DTI acquisitions for this study is the fractional anisotropy maps (FA-maps), which provide useful information regarding the kidney tissue (i.e. renal microstructure, fibrosis). Decreasing FA values have been found to correlate with decreased renal function in several renal diseases (i.e. CKD).

Spin echo – Echo planar imaging (EPI):

The diffusion is usually measured with a Spin Echo (SE) pulse sequence. SE-EPI begins with a typical SE pulse sequence and allows the acquisition of not only a single echo after the excitation pulse (RF 180^o) but a number of additional echoes as well. In details rapidly switching gradients create multiple gradient echoes within one spin echo in order to acquire the entire k-space. The use of varying gradient strengths (blipped low amplitude phase-encoding gradient pulses) rephase the signal, preventing the transverse magnetization M_{xy} from decaying completely. Hence these gradients allow to perform successive phase encoding steps to sweep the complete k-space (each activation of a phase encoding gradient makes a small step in order to transfer to the next line of the k-space). At the same time the alternating frequency encoding gradients enable the back and forth "sweep" across the frequency encoding direction within each phase encoding step.

DTI model-fitting:

The DTI model which is used to fit the data is based on the diffusion tensor ***D***, which is a 3x3 symmetric, positive-definite matrix, hence it has three orthogonal eigenvectors and three positive eigenvalues[35].

$$\boldsymbol{D} = \begin{bmatrix} D_{xx} & D_{xy} & D_{xz} \\ D_{yx} & D_{yy} & D_{yz} \\ D_{zx} & D_{zy} & D_{zz} \end{bmatrix} \quad (2.3)$$

The three positive eigenvalues of the tensor ($\lambda_1, \lambda_2, \lambda_3$) represent the diffusivity in the direction of each eigenvector. The eigenvectors and the eigenvalues define an ellipsoid that represents an isosurface of diffusion probability: the axes of the ellipsoid are aligned with the eigenvectors and their lengths depend on the eigenvalues. The most widely used anisotropy measure is the fractional anisotropy (FA) and is defined as the normalized variance of the eigenvalues. An intuitive explanation for FA is that it shows the

difference of the tensor ellipsoid's shape from that of a perfect sphere. For the context of this study FA is the imaging biomarker of interest for DTI data since it provides information regarding tissue microstructure (may be indicative of inflammation, fibrosis) and it is calculated as shown below[36]:

$$FA = \frac{1}{\sqrt{2}} \frac{\sqrt{(\lambda_1 - \bar{\lambda})^2 + (\lambda_2 - \bar{\lambda})^2 + (\lambda_3 - \bar{\lambda})^2}}{\sqrt{\lambda_1{}^2 + \lambda_2{}^2 + \lambda_3{}^2}} \quad (2.4)$$

where $\bar{\lambda}$ is the mean diffusivity (mean of the eigenvalues).

There are two special cases of diffusion depicted in Fig.9. The first is the isotropic diffusion where the off-diagonal elements of the diffusion tensor are all zero and the main diagonal elements are all equal:

$$\boldsymbol{D} = \begin{bmatrix} D & 0 & 0 \\ 0 & D & 0 \\ 0 & 0 & D \end{bmatrix} \quad (2.5)$$

In this case the molecules have unrestricted motion and the diffusion is the same for every direction since the molecules are equally likely to move in any direction (Fig.9.a), hence the FA = 0.

The second is the case of anisotropic diffusion, where molecular displacement differs when measured in different directions. This is most of the times the case for biological tissues, since they are highly structured and exhibit different diffusion coefficients for different diffusion directions (Fig.9.b), hence FA>0. For anisotropic diffusion the diffusion tensor is consisted of the three diagonal elements D_{xx}, D_{yy} and D_{zz} which represent the diffusion coefficients measured in correspondence to the frame of reference along *x*, *y* and *z* axes. The off-diagonal terms describe the correlation between random motions corresponding to paired combinations of the principal directions.

(a) Isotropic diffusion, FA = 0 (b) Anisotropic diffusion, FA>0

Figure 9: Schematic representation of (a) isotropic and (b) anisotropic diffusion.

In order to perform a DTI acquisition, 3 gradients with orthogonal directions (x, y, z) are required, this effectively means that 6 different gradient directions will be applied by paired combinations of directions: *xx, yy, zz, xy=yx, yz=zy, xz=zx*. Despite the fact that the diffusion matrix for anisotropic diffusion has 9 elements, only 6 of them will be independent since: $D_{xy} = D_{yx},\ D_{yz} = D_{zy},\ D_{xz} = D_{zx}$.

The link between the measured signal and the diffusion tensor is established by the *b-matrix* whose values depend on the gradient's direction, strength and timing. The 3D diffusion weighting *b*-matrix consists of six terms: $b_{xx}, b_{yy}, b_{zz}, b_{xy}, b_{yx}, b_{yz}, b_{zy}, b_{xz}, b_{zx}$ where $b_{xy} = b_{yx},\ b_{yz} = b_{zy}, b_{xz} = b_{zx}$

The following equation describes the intensities per voxel for the acquired signal[37]:

$$S = S_0 * e^{-\boldsymbol{b}:\boldsymbol{D}} \tag{2.6}$$

where:

$$\boldsymbol{b}:\boldsymbol{D} = b_{xx} * D_{xx} + b_{yy} * D_{yy} + b_{zz} * D_{zz} + 2 * b_{xy} * D_{xy} + 2 * b_{xz} * D_{xz} + 2 * b_{yz} * D_{yz} \tag{2.7}$$

where *S* is the *b*-dependent signal intensity of the image and S_0 is the signal intensity in the absence of diffusion sensitization.

For the calculation of the diffusion weighting *b*-matrix for each gradient direction, the following must be taken into consideration:

1. The total gradient amplitude is the same in each individual diffusion weighted acquisition, hence the overall gradient vector can be expressed as the product of a gradient magnitude *G* and the normalized gradient direction vector $\boldsymbol{G_n}$ where:

$$\boldsymbol{G_n} = (g_x, g_y, g_z)^T \tag{2.8}$$

and

$$g_x{}^2 + g_y{}^2 + g_z{}^2 = 1 \tag{2.9}$$

2. The relative magnitudes of the *b-matrix* term are calculated from the product of the normalized gradient magnitudes as follows:

$$\boldsymbol{g} = \boldsymbol{G_n} * \boldsymbol{G_n}^{\boldsymbol{T}} = \begin{pmatrix} g_x \\ g_y \\ g_z \end{pmatrix} * \begin{pmatrix} g_x & g_y & g_z \end{pmatrix} = \begin{bmatrix} g_x{}^2 & g_x\, g_y & g_x\, g_z \\ g_y\, g_x & g_y{}^2 & g_y\, g_z \\ g_z\, g_x & g_z\, g_y & g_z{}^2 \end{bmatrix} \tag{2.10}$$

$$\boldsymbol{b} = \mathrm{b} * \boldsymbol{g} \tag{2.11}$$

and finally:

$$\boldsymbol{b}{:}\boldsymbol{D} = \mathrm{b} * \boldsymbol{g}{:}\boldsymbol{D} = \ tr\ (\mathrm{b} * \ G_n * {G_n}^T * D) \tag{2.12}$$

where b stands for the b-values and *tr* for the trace of the matrix.

During the process of the model fitting the varying parameter is considered to be the diffusion weight and the model is linearized as follows:

$$S = S_0 * \ e^{-\boldsymbol{b}:\boldsymbol{D}} \ \Rightarrow \ln(S) = \ln(S_0) - \ \boldsymbol{b}{:}\boldsymbol{D} \ \Rightarrow$$

$$\Rightarrow \ln(S) = \ln(S_0) - (b_{xx} * D_{xx} + b_{yy} * D_{yy} + b_{zz} * D_{zz} + 2 * b_{xy} * D_{xy} + 2 * b_{xz} * D_{xz} + 2 * b_{yz} * D_{yz}) \tag{2.13}$$

This is a system of linear equations which is solved to estimate the following parameters: $S_0, D_{xx}, D_{yy}, D_{zz}, D_{xy}, D_{xz}, D_{yz}$. A typical fit on unregistered DTI data is shown in Fig.10.

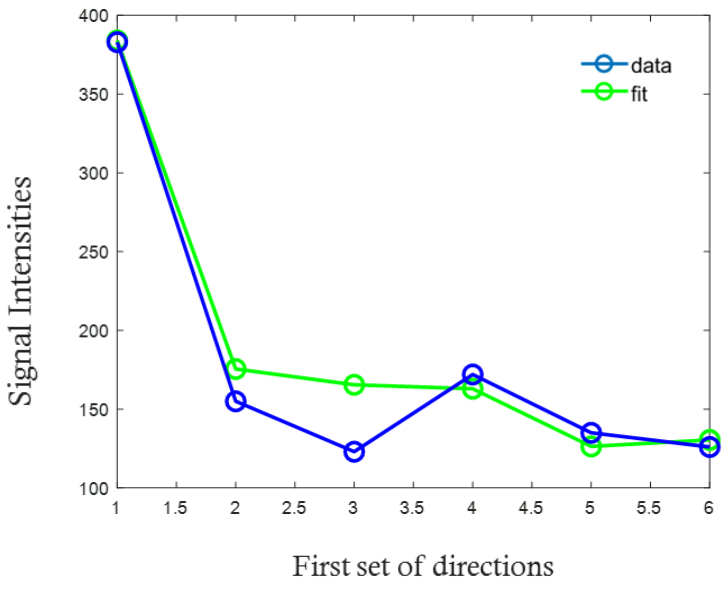

Figure 10: Indicative DTI-fit for a single pixel before registration

2.3.5 Dynamic Contrast Enhanced (DCE) MRI

An ultrafast spoiled gradient echo pulse sequence[38] was utilized for the DCE (Dynamic Contrast Enhanced) acquisitions in this study. DCE-MRI is a promising technique that allows the quantification of kidneys' physiological parameters i.e. renal blood flow, glomerular filtration rate, fractional plasma volume etc., without the use of ionizing radiation. In DCE, the subject is administrated with contrast agent, usually gadolinium (Gd) based, via an intravenous bolus. DCE exploits the T1-shortening effects of Gd, hence rapid acquisitions of T1-weigthed images take place over a period of approximately 5-10 minutes. Once Gd reaches a tissue it diffuses into the extravascular extracellular space, hence after its accumulation in the tissue the strength of the MR signal is enhanced. However, as the Gd gets washed out of the kidneys the signal intensity gradually decays. One of the most significant advantages of DCE is that it allows the assessment of perfusion and filtration parameters separately between the two kidneys, in contrast to blood tests that can provide only global measurements. The quantification of the contrast enhancement for the tissues under observation is the most important goal for DCE, since it allows the calculation of regional blood flow (RBF), a very useful imaging biomarker.

Ultrafast spoiled gradient echo:

An ultrafast gradient echo sequence utilizes a small flip angle RF pulse, optimized k-space sampling and short TR in order to reduce the acquisition time (≈ 1 sec per slice). Nevertheless, the use of a small flip angle and the short TR lead to acquisitions with lower T1-weighting. In order to counter that a 180^{o} inversion pulse is used to "prepare the magnetization" at the beginning of the sequence. The k-space lines can be acquired all together after only one inversion pulse ("single shot"), or alternatively a subset of them can be acquired after every inversion pulse ("segmented filling"). The turbo factor (TF) is the portion that describes how many lines of k-space get acquired within one R-R interval.

DCE model-fitting based on the two compartment filtration model for the kidney:

The two-compartment filtration model (2CFM) divides the kidney into two compartments, namely the vascular or plasma and the extravascular or tubular compartment[39] (Fig.11). The contrast agent first enters the vascular space where it gets distributed over the plasma volume. From there a fraction of it is excreted, while the rest is transported in the tubular compartment. The agent gets distributed over the tubular volume and then is excreted from the kidneys.

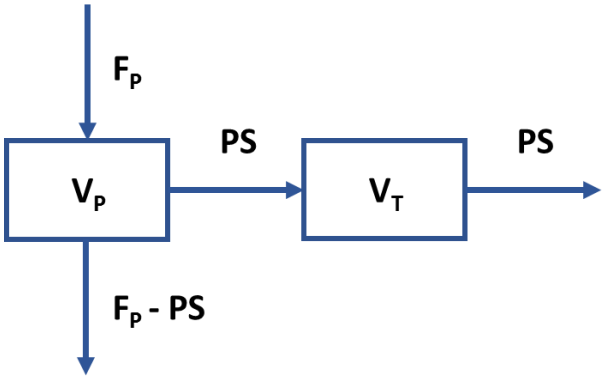

Figure 11: Tracer kinetic model: two-compartment filtration model

This model has four independent parameters: the plasma volume V_P, the tubular volume V_T, the plasma flow F_P and the permeability-surface area product PS which is indicative of how leaky the capillary is to contrast agent. Given that the mean transit time in the vascular and tubular compartments is T_P and T_T respectively, then T_P and T_T measure how long it takes for a contrast agent molecule to pass through the plasma and tubules respectively. Also, the concentration of the contrast agent in the arterial space is denoted as $C_A(t)$ and the concentrations in the vascular and tubular space are denoted as $C_P(t)$ and $C_T(t)$ respectively.

The central volume theorem provides the following fundamental relation:

$$F_P = \frac{V_P}{T_P} \tag{2.14}$$

The total tissue concentration is then given by:

$$C(t) = V_P\, C_P(t) + V_T\, C_T(t) \tag{2.15}$$

The change of tracer mass in the tubular compartment equals to the difference between the concentration flowing from the vascular to the tubular compartment and the concentration that is filtered out. Hence, the mass balance equation for the tubular space is:

$$V_T \frac{d_{C_T}(t)}{dt} = PS\, C_P(t) - PS\, C_T(t) \tag{2.16}$$

Given that:

$$PS = \frac{V_T}{T_T} \tag{2.17}$$

Likewise for the conservation of the tracer mass in the plasma compartment:

$$V_P \frac{d_{C_P}(t)}{dt} = F_P\, C_A(t) - F_P\, C_P(t) \tag{2.18}$$

For the two-compartment filtration model fitting on the DCE data, an arterial input function was selected manually inside the abdominal aorta on the transverse slice. The equations that follow combined with those mentioned above allow to solve the problem by performing a linear least squares fitting as performed in study[40].

By differentiating Eq.2.15 and substituting with the Eq.2.16, Eq.2.18 C_T' and C_P' can be eliminated leading to:

$$C' = F_P(C_A - C_P) + PS(C_P - C_T) \tag{2.19}$$

By differentiating Eq.2.19 and substituting with the Eq.2.16, Eq.2.18 C_T' and C_P' can be eliminated once again leading to:

$$C'' = F_P C_A' - (F_P - PS)\frac{F_P}{V_P}(C_A - C_P) - PS\frac{PS}{V_T}(C_P - C_T) \tag{2.20}$$

Hence there is a system of 3 equations Eq.2.15, Eq.2.19, Eq.2.20 with two unknowns: C_P, C_T. Eq.2.15, Eq.2.19 are used to solve for the unknowns and the result is substituted to the third one, hence:

$$C_P = \frac{PS\, C - (F_P\, C_A - C')\, V_T}{PS\, V_P + (PS - F_P)\, V_T} \tag{2.21}$$

$$C_T = \frac{F_P\, V_P\, C_A + (PS - F_P)\, C - V_P\, C'}{PS\, V_P + (PS - F_P)\, V_T} \tag{2.22}$$

Substituting Eq.2.21 and Eq.2.22 in Eq.2.20 leads to a second order equation that depends on: the data C, C_A, and the unknown parameters. Hence:

$$C'' = -aC - \beta C' + \gamma C_A + F_P\, C_A' \tag{2.23}$$

where:

$$a = \frac{1}{T_T\, T_P}, \beta = \frac{T_T + T_P}{T_T\, T_P}, \gamma = \frac{F_P\, T}{T_T\, T_P} \tag{2.24}$$

Using the following notation:

$$\bar{f}(t) = \int_0^t f(\tau)\, d\tau \tag{2.25}$$

Leads to:

$$C(t) = -a\,\bar{\bar{C}}(t) - \beta\bar{C}(t) + \gamma\bar{\bar{C}}_A(t) + F_P\,\bar{C}_A(t) \tag{2.26}$$

The data *C(t)* and $C_A(t)$ are measured over N time points hence the Eq.2.26 will lead to system of N linear equations, which can be summarized in a matrix of the following form $\boldsymbol{C} = \boldsymbol{A}\,\boldsymbol{X}$ where $\boldsymbol{C} = [C(t_0), \dots, C(t_{N-1})]$ is a vector of the measured concentrations and $\boldsymbol{X} = [\alpha, \beta, \gamma, F_P]$ contains the unknowns. Hence, the matrix $\boldsymbol{A}$ has 4* N elements (where N is the number of time points for the current DCE acquisition) and can be described as follows:

$$A = \begin{pmatrix} -\bar{\bar{C}}(t_0) & -\bar{C}(t_0) & \bar{\bar{C}}_A(t_0) & \bar{C}_A(t_0) \\ -\bar{\bar{C}}(t_1) & -\bar{C}(t_1) & \bar{\bar{C}}_A(t_1) & \bar{C}_A(t_1) \\ \vdots & \vdots & \vdots & \vdots \\ -\bar{\bar{C}}(t_{N-1}) & -\bar{C}(t_{N-1}) & \bar{\bar{C}}_A(t_{N-1}) & \bar{C}_A(t_{N-1}) \end{pmatrix} \tag{2.27}$$

The matrix elements are calculated from Eq.2.25 by numerical integration of the data: $C(t_N)$ and $C_A(t_N)$. The matrix equation can be solved by Linear Least Squares:

$$\mathbf{X} = (\boldsymbol{A}^T\,\boldsymbol{A})^{-1}\,\boldsymbol{A}^T\,\boldsymbol{C} \tag{2.28}$$

It is important to note that typically the number of time points for DCE-MRI data are several hundreds while there are only four unknowns, hence the system is overdetermined.

The physiological parameters T, T_T, T_P can be derived from the calculated $\alpha, \beta, \gamma, F_P$ based on Eq.2.24:

$$T = \frac{\gamma}{a\,F_P}, T_P = \frac{\beta - \sqrt{\beta^2 - 4a}}{2a}, T_T = \frac{\beta + \sqrt{\beta^2 - 4a}}{2a} \tag{2.29}$$

For the case where $\beta^2 < 4a$ the solution is:

$$T_P = T_T = \frac{\beta}{2a} \tag{2.30}$$

The mean transit time of the whole system can be described by:

$$T = \frac{V_P + V_T}{F_P} \tag{2.31}$$

The parameters V_P, V_T and F_T can be derived from F_P, T, T_T, T_P based on Eq2.17, Eq.2.31:

$$V_P = F_P\,T_P\,, \qquad V_T = F_P\,(T - T_P), \qquad PS = \frac{V_T}{T_T} \tag{2.32}$$

Once the aforementioned parameters are estimated, the blood flow (BF) which is the imaging biomarker of interest for DCE data, can be calculated as:

$$BF = \frac{F_P}{1 - Hct} \tag{2.33}$$

where Hct is the hematocrit value which is considered to be equal to 0.45[41] for all subjects (typical value), this typical value could be replaced by the actual measurement per patient if it is available.

A typical fit on unregistered DCE data is shown in Fig.12.

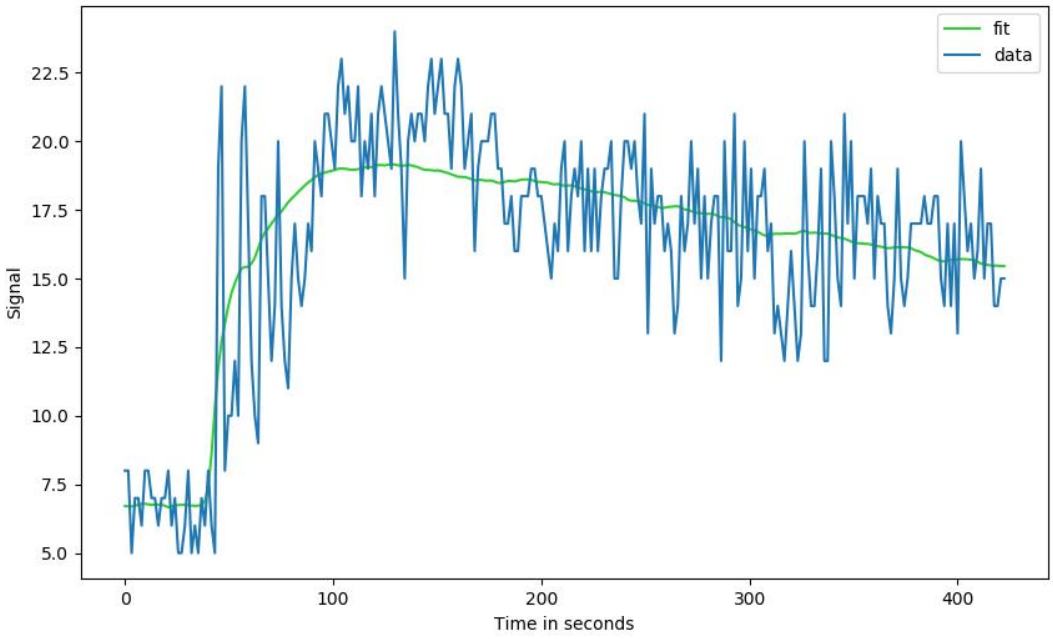

Figure 12: Indicative DCE-fit for a single pixel before registration

Chapter 3

Background on registration methods for MRI

3.1 Basics of medical image registration

In medical imaging applications, one of the most common issues is the correction of motion-induced artifacts, a characteristic example is the case of abdominal MR imaging where breathing causes distortions and displacements of the depicted organs. The image processing technique used to correct for the motion that has corrupted the acquired images is called image registration and can be formulated mathematically as follows:

Given two images: $F(x, y)$ (fixed image) and $M(x, y)$ (moving image), defined in grid Ω, the goal of image registration is to find the geometric transformation T such that $M(T(x, y))$ is optimally aligned to $F(x, y)$. Hence the process of registration can be formulated as the following maximization problem[42, 43]:

$$\hat{T} = \underset{T \in \Omega_T}{\operatorname{argmax}} S\big(F, M(T)\big) \tag{3.1}$$

where T represents the transformation, S is the selected similarity metric and $\Omega_{T\ T}$ is the space of all possible transformations. The same problem could be formulated as a minimization problem if a dissimilarity measure was used instead. As shown in Eq.3.1 there are three main components necessary to perform a successful registration: a geometric transformation (T), a measure of similarity (S) and an optimization algorithm ($\underset{T \in \Omega_T}{\operatorname{argmax}}$), these three components are discussed in more details below.

3.1.1 Geometric transformations

In medical image registration the choice of a suitable geometric transform is of crucial importance and is based on a priori knowledge of certain characteristics of the expected image deformations (i.e. rigid or non-rigid body deformations, locality of the deformation field etc.). The estimation of the specific parameters for the geometric transformation is the aim of the optimization process. One of the most important traits for every geometric transform is the flexibility to handle possible image degradations, in principle a transform is more flexible as its complexity increases. The complexity of geometric transformations is indicated by the degrees of freedom (DOF). Bellow follows a short summarization of the most common transformations for each of the two main geometric transformation categories: linear and non-linear transformations.

1. Linear Transformations: such transformations are global and often require the calculation of translational and rotational vectors. These transforms are applied when the structures of the

images are not expected to be highly distorted or deformed. From a mathematical perspective linear geometric transformation can be modeled as:

$$\boldsymbol{x}' = \boldsymbol{L}\,\boldsymbol{x} \tag{3.2}$$

where $\boldsymbol{L}$ is the transformation matrix, $\boldsymbol{x}$ is a vector of image coordinates $\boldsymbol{x} = (x, y)$ and $\boldsymbol{x}'$ is the new set of coordinates. The main types of linear transformations are summarized in Table.2[44] and an example for each type of linear transformations is visualized in Fig.13.

2. Non-linear Transformations: This case encompasses a wide range of transformations spanning from almost linear to the most complex ones that have a separate displacement vector for each pixel. For the scope of this thesis the focus will be on the free-form (non-linear) transformation, a more detailed review of non-linear transformations can be found in Wang et al[45]. A free-form deformation (FFD) transform provides a way to model arbitrary deformations that will be applied on an image. The main idea is to deform an image by manipulating a grid of control points

Type	**Geometric transformations allowed**	**Invariant Properties**	**Formula** (***Notation***: (x, y) are the coordinates of a single pixel before the transformation and (x', y') are the respective coordinates after the transformation)
Euclidean (3 DOF)	rotations, translations (used when no changes in size or shape are expected)	length, area	$\begin{pmatrix} x' \\ y' \\ 1 \end{pmatrix} = \begin{bmatrix} cos\varphi & -sin\varphi & t_x \\ sin\varphi & cos\varphi & t_y \\ 0 & 0 & 1 \end{bmatrix} \begin{pmatrix} x \\ y \\ 1 \end{pmatrix}$ t_x, $t_y \in R$, and $[t_x, t_y]$ is the translation vector and φ is the rotation angle
Scaling (4 DOF)	rotations, translations and scaling (if scaling is isotropic it is called similarity transformation)	ratio of lengths, angle	$\begin{pmatrix} x' \\ y' \\ 1 \end{pmatrix} = \begin{bmatrix} s * cos\varphi & -s * sin\varphi & t_x \\ s * sin\varphi & s * cos\varphi & t_y \\ 0 & 0 & 1 \end{bmatrix} \begin{pmatrix} x \\ y \\ 1 \end{pmatrix}$ t_x, $t_y \in R$, and $[t_x, t_y]$ is the translation vector, φ is the rotation angle and s: is an isotropic scaling factor
Affine (6 DOF)	translation, rotation, scaling, shearing	parallelism, ratio of lengths on parallel lines, ratio of areas	$\begin{pmatrix} x' \\ y' \\ 1 \end{pmatrix} = \begin{bmatrix} a_{11} & a_{12} & t_x \\ a_{21} & a_{22} & t_y \\ 0 & 0 & 1 \end{bmatrix} \begin{pmatrix} x \\ y \\ 1 \end{pmatrix}$ where $a_{i,j}$, t_x, $t_y \in R$, and $[t_x, t_y]$ is the translation vector
Projective (8 DOF)	generalization of affine transform in which parallelism is not preserved	concurrency[1], collinearity[2], order of contact[3], cross ratio[4]	$\begin{pmatrix} u \\ v \\ w \end{pmatrix} = \begin{bmatrix} a_{11} & a_{12} & t_x \\ a_{21} & a_{22} & t_y \\ a_{31} & a_{32} & 1 \end{bmatrix} \begin{pmatrix} x \\ y \\ 1 \end{pmatrix}$ where $a_{i,j}$, t_x, $t_y \in R$, and $[t_x, t_y]$ is the translation vector and a_{31}, a_{32} are responsible for the projection and influence the parallelism of the lines, $x' = \frac{u}{w}, y' = \frac{v}{w}$

[1] a point of concurrency is the point where 3 or more lines intersect
[2] geometrical property that refers to a set of points lying on a single point
[3] intersection = 1 point contact, tangency = 2 points contact, inflections = 3 points contact with line
[4] ratio of ratio of lengths

Table 2: Summary of the linear transformations for image registration.

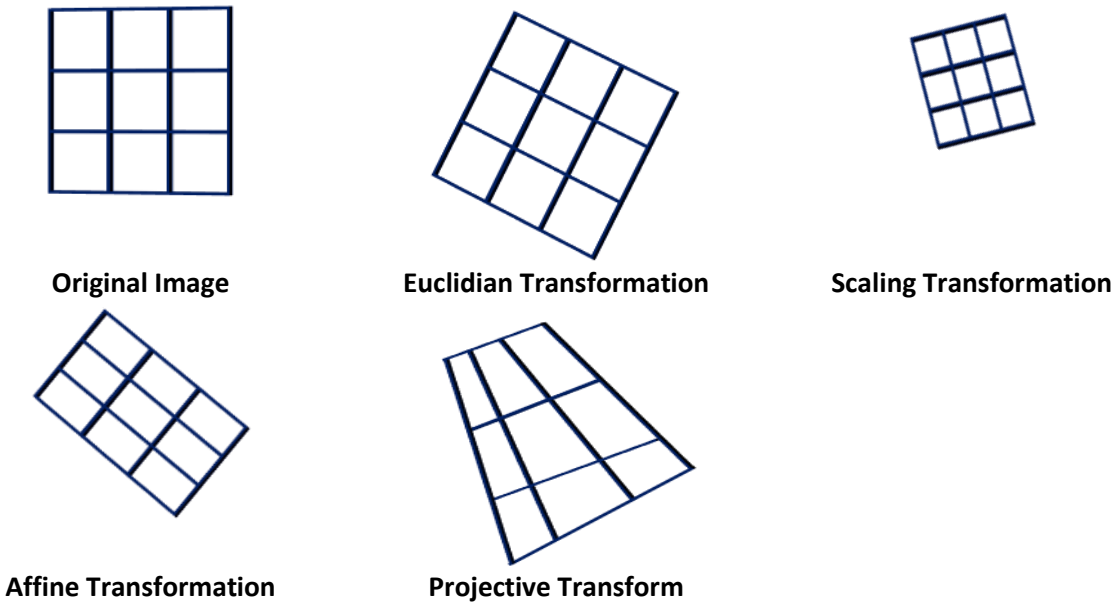

Figure 13: Examples of linear transformations.

spanning the image. These control points will be displaced based on the optimization of a cost function and the displacements will then be transferred to the underlying pixels in order to deform the actual image. The displacement vectors of the pixels lying between control points will be computed based on the values of neighboring control points that surrounds them. Methods based on FFD create continuous and smooth deformations enforced by the properties of the basis function used to model them. Some common basis functions that can be utilized to model non-linear FFD transformations are the following:

a) Radial Basis Functions (RBF) transformations: RBF is a data interpolation method which consists of a linear combination of radially symmetric basis functions, each centered around a particular control point. The RBF value at an interpolation point $\boldsymbol{x}$ is defined as follows[46]:

$$U_{RBF}(\boldsymbol{x}) = f(\boldsymbol{x}) + \sum_{i=1}^{N} \omega_i \ \phi(|\boldsymbol{x} - \boldsymbol{p}_i|) \tag{3.3}$$

where: N is the total number of control points, ω_i is a real-valued weight, ϕ is a basis function and $|\boldsymbol{x} - \boldsymbol{p}_i|$ is the distance between point $\boldsymbol{x}$ and the control point $\boldsymbol{p}_i$ (often referred to as landmark), $f(\boldsymbol{x})$ is a polynomial which is usually chosen to be 1st degree in order to perform a global affine transformation. $f(\boldsymbol{x})$ can also be omitted from the transformation, however when included it helps making the process more precise.

The basis function $\phi(r)$ (where r is the Euclidean distance $r = |\boldsymbol{x} - \boldsymbol{p}_i|$) can take different forms including:

a) Gaussian: $\phi(r) = \exp(-\beta r^2), \beta > 0$

b) Thin-plate spline: $\phi(r) = r^2 \log(r)$

c) Multi-quadratic: $\phi(r) = \sqrt{r^2 + \beta^2}, \beta > 0$

Each control point in an RBF transformation model is capable of causing a global influence on the whole image, this is obvious from the summation in Eq.3.3, which indicates that any interpolated RBF value gets affected by all the control points. Hence, the most important disadvantage of this approach is that it has limitations when complex localized deformations are required.

b) B-Splines: is a more general form of the Bezier curves and they are consisted of a series of polynomials. B-Splines are defined by their order, a set of control points and a knot vector. The number of polynomials needed depends on the number of the control points and the order of the curve. The knot vector indicates where the polynomials that constitute the B-Spline start and stop.

B-Splines can be used to perform a free form deformation registration, where a grid of evenly spaced control points is defined over the moving image and a parametrized coordinate transformation is calculated (the choice of the control point spacing is a user defined parameter). This transformation depends on a vector of transformation parameters which is estimated by the optimization process. In this study B-Splines were utilized to parametrize a coordinate transformation that minimized the mean squared error between the fixed and the deformed moving image.

A dense deformation field that distributes the displacement of the control points to all the pixels of the image can be computed using a B-Spline transformation function. This function takes as parameters a pixel $\boldsymbol{x} = (x, y)^{\tau}$ and the current control point configuration $\boldsymbol{\varphi}$ to calculate the pixel's displacement after the deformation. For the case of cubic B-Splines[47] and under the assumption of a uniform spaced grid of control points (Fig.14, s_x = s_y) the displacement of every pixel is determined by the displacement of a number of control points around it (16 control points for 2D and 64 for 3D). The displacement is calculated based on the following formula which presents a 2-D tensor product of 1D cubic B-Splines, Fig.14 provides a visualization of the process described above[48]:

$$U_{cubic}(\boldsymbol{x}, \boldsymbol{\varphi}) = \sum_{l=0}^{3} \sum_{m=0}^{3} B_3^l(u)\ B_3^m(v)\ \varphi\,(i+l, j+m) \tag{3.4}$$

where:

$$B_3^0(t) = \frac{-t^3 + 3t^2 - 3t + 1}{6}, B_3^1(t) = \frac{3t^3 - 6t^2 + 4}{6}, \\ B_3^2(t) = \frac{-3t^3 + 3t^2 + 3t + 1}{6}, B_3^3(t) = \frac{t^3}{6} \tag{3.5}$$

Let (i, j) indicate the indices of control points and $\boldsymbol{p} = (p_x, p_y)^\tau$ denote the control point that is the closest one to the pixel for which the displacement is calculated:

$$p_x = \left\lfloor \frac{x}{s_x} \right\rfloor,\ p_y = \left\lfloor \frac{y}{s_y} \right\rfloor \tag{3.6}$$

Then the index of the basis control point is $(i, j) = (p_x - 1, p_y - 1)$ and the last control point of the summation will have as index: $(i + 3, j + 3) = (p_x + 2, p_y + 2)$. The parameters (u, v) represent the relative position of the pixel within its surrounding block of control points. These parameters are the fractional remainders of pixel coordinates between control points which are formulated as follows:

$$u = \frac{x}{s_x} - \left\lfloor \frac{x}{s_x} \right\rfloor, v = \frac{y}{s_y} - \left\lfloor \frac{y}{s_y} \right\rfloor \tag{3.7}$$

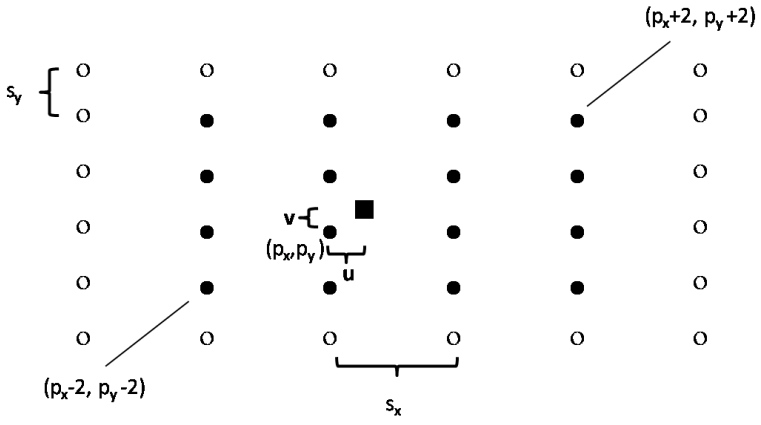

Figure 14: Control point configuration for the calculation of the displacement of a pixel (bold square) based on cubic B-Splines (2D example).

Apart from the FFD transformations examined in detail above, there are also other categories of non-linear transformation models that can be used in medical image registration. For example, the elastic body model where the moving image is modelled as an elastic membrane upon which internal forces (indicative of the membrane's elastic properties) and external forces (representing the displacement field for the registration process) act in order to register the moving image to the target. This method works well mainly for small deformations which is not always the case especially for free-breathing acquisitions in renal MRI. The viscous fluid flow model, where the image is modelled as a viscous fluid with the transformation being formulated as a simplified version of the Navier-Stokes equation. In this case instead of defining the deformation using control points like in FFD the pixels of the moving image are deformed following a velocity field. However, the human body is not totally fluid and hence this model is not ideal since it provides higher flexibility (which may end up in misregistration i.e. growth of a region instead of deforming it). The optical flow model is another non-linear transformation model, which assumes that the moving and target images are consecutive samples from a single image sequence and utilizes optical flow to return a vector field for each pixel in the moving image that shows where this pixel moved in the next frame. The basic assumption for this method is that the intensity of a certain pixel is constant for a short time interval, which means that this method may not be effective for large steep deformations. Another alternative is the demon's method which combines optical-flow based methods with those of diffusive models. This method is based on Maxwell's analogy for thermodynamics with the boundaries of the objects being considered to act as semi-separable membranes through which the moving image will diffuse in accordance to the effectors (demons) located in the membranes. This method however may not be suitable for biological tissue since it lacks a particular physical significance. Finally, the diffeomorphism model which is closely related to the demon's method is another alternative which allows the calculation of differentiable and invertible transformations. Inverse consistency is a significant trait for image registration since ideally the transformation that maps the moving on the target image and its inverse should be uniquely determined, such transformations would allow for measurements or segmentations on one image to be transferred to the other. However, it should be noted that inverse consistency by itself (as a cost function) is not sufficient for a proper image registration and it is usually used as a constraint.

Each non-linear transformation model has its own advantages and disadvantages which have been extensively examined in several review papers (i.e Wang et al , Sotiras et al.). For the context of this study FFD based on B-Splines was chosen as the registration transform, since it can provide plausible

deformations for medical image registration purposes while being computationally efficient (elastix implementation).

3.1.2 Measures of similarity

The measurement of the similarity between F and M, is required in order to calculate an optimal set of transformation parameters which will be applied on M in order to compensate for the motion that originally corrupted it. The two main categories of measures of similarity are the features-based and intensity-based methods [42, 49].

1. Features-based methods: for this case certain landmarks are extracted either manually[50] or automatically[43], aiming towards establishing correspondence between the two images. In both cases some kind of distance (i.e. Euclidean) between respective landmarks of the fixed and moving image is set as the cost function for the registration problem at hand. As regards to the automatically extracted landmarks there are three main pairs of respective features from fixed and moving images that can be utilized for the comparisons:
    a) points to points (which can be extracted with the use of well-known computer vision algorithms like SIFT[51] and SURF[52])
    b) edges to edges[53] (such edges can be isolated in both images with the use of suitably designed filters)
    c) surfaces to surfaces[54]

    The extracted features may or may not coincide with anatomical points of interest, in any case such approaches achieve the radical decrease of information for both fixed and moving images, increasing the speed of the procedure.

2. Intensity-based methods: for several applications feature selection is a highly challenging process, while in some cases the number of the extracted features may be considered insufficient. The aforementioned fact explains why the most popular choice for the measures of similarity, is to find the transformation T that will match the moving and fixed images, based on metrics defined by their respective pixel intensities[47, 55, 56]. Table.3 summarizes a few of the most commonly used intensity-based dissimilarity (denoted with D) and similarity functions (denoted with S) for the field of image registration (a more detailed list can be found in study[57]).

Cost – Similarity function	Formula	Notes
Mean Squared Error	$D = \frac{1}{N}\sum_j (M_j - F_j)^2$ where: N is the total number of the pixels (same for M and F), $M_j = M(x_j, y_j)$ and $F_j = F(x_j, y_j)$	1. Implemented in every registration software package i.e. SPM[58], AIR[59], ITK[60], elastix[4], ANTS[61]. 2. Based on the assumption that similar anatomical structures in the two images have similar intensities. 3. Intra-modal (for fixed intensity scaling)
Correlation Ratio	$S = \frac{1}{var(M)} * \sum_k \frac{n_k}{N} var(M_k)$ where: M_k is the k[th] iso-set defined as the set of intensities in M at positions where the intensity in F is in the kth intensity bin, n_k is the number of elements in the set M_k such that $N = \sum_k n_k$, where N is the total number of pixels	Inter-modal applications (it operates based on the assumption that if there are no changes in intensities of tissues in one image then the same should apply for the other image as well)
Normalized Cross-Correlation Coefficient	$S = \frac{\sum_j (M_j - \bar{M})(F_j - \bar{F})}{\sqrt{\sum_j (M_j - \bar{M})^2}\sqrt{\sum_j (F_j - \bar{F})^2}}$ where: $M_j = M(x_j, y_j)$ and $F_j = F(x_j, y_j)$	Intra-modal applications (when acquisition parameters are slightly different)
Mutual Information (MI)	$S = H(M) + H(F) - H(M,F)$ where entropy is defined as: $H(M) = -\sum_c p_M(c)\log(p_M(c))$ and $p_M(c)$ is the probability that a pixel in M has intensity c, $H(F)$ is defined respectively The joint entropy is defined as: $H(M,F) = -\sum_c \sum_d p_{M,F}(c,d)\log(p_{M,F}(c,d))$ where $p_{M,F}(c,d)$ shows the probability that a pixel with intensity c in M corresponds to a pixel with intensity d in F	1. Detects the degree of mutual information between 2 images, (entropy based). 2. Does not insist on strict relationships between intensities. 3. Inter-modal (or intra-modal when high differences in intensities are expected).
Normalized Mutual Information (NMI)	$S = \frac{H(M) + H(F)}{H(M,F)}$ following the same notation as above	Same as MI, but it is used for the cases where the two images would overlap only for small areas.

Table 3: Summary of the most common cost and similarity function used for MRI registration.

3.1.3 Optimization algorithms

Most optimization algorithms are iterative processes that utilize the results of the similarity measurements in order to define the optimal Geometric Transformation T. These methods estimate the optimal set of parameters via an iterative updating process[62] which can be formulated as in study[63]:

$$\boldsymbol{p}_{k+1} = \boldsymbol{p}_k + \alpha_k * \boldsymbol{d}_k \quad (3.8)$$

where $\boldsymbol{p}$ is the vector of parameters for transformation T, α_k is the step size (or gain factor) along the search direction of iteration k and $\boldsymbol{d}$ is the search direction. In addition, for future usage $g(\boldsymbol{p}_k)$ is defined as the derivative of the cost function for the vector of parameters at the k^{th} iteration with the respective vector of parameters $\boldsymbol{p}_k$.

Equation 3.8 is the basis for the majority of the most common optimization methods including: Gradient Descent method and its alternations[63] (i.e. Conjugate Gradient Descent, Stochastic Gradient Descent, Adaptive Stochastic Gradient Descent etc), Quasi-Newton[46]and Levenberg-Marquardt[46].

1. Gradient Descent (GD) optimizes an objective function by following the direction of its negative gradient,d searching for a minimum point. This method suffers from being highly dependent on the choice of initial conditions (i.e. step size). GD can be described by Eq.3.8 if the direction of search is set to be $\boldsymbol{d}_k = -g(\boldsymbol{p}_k)$ and the gain factor (α_k) is decaying function of k. Over the years a number of alternations of GD have been proposed in order to achieve better convergence, indicative examples include:

   a) Conjugate Gradient Descent (CGD) which utilizes knowledge from previous steps in order to avoid step repetition by taking steps in conjugate (/orthogonal) directions. CGD can be described by Eq.3.8 if $\boldsymbol{d}_k = -g(\boldsymbol{p}_k) + \beta_k * \boldsymbol{d}_{k-1}$ which means that the search direction is a linear combination of $g(\boldsymbol{p}_k)$ and the previous search direction $\boldsymbol{d}_{k-1}$, with β_k being a weighting factor.

   b) Stochastic Gradient Descent (SGD) which replaces the direction of search by a non-deterministic estimate of it, calculated from a subset of the data. Eq.3.8 can describe SGD given that $\boldsymbol{d}_k = -\widehat{g(\boldsymbol{p}_k)}$. The convergence of the optimization process is guaranteed if the

bias of the approximation error tends to zero: $E\big(\widehat{g(\boldsymbol{p}_k)}\big) - g(\boldsymbol{p}_k) \to 0 \;\; as \;\; k \to \infty$ where E denotes expectation. SGD usually manages to converge faster than plain GD.

c) Adaptive Stochastic Gradient Descent (ASGD[64]) this specific variant of SGD implements an adaptive step size mechanism, which is based on the inner product of the gradients of two consecutive steps. Hence, if the gradients of two consecutive steps point in the same direction the step size is increased, while if they point in opposite directions it gets decreased. The step size is defined by a monotonic decreasing function γ and it depends on "time" t_k instead of the iteration k, hence Eq.3.8 is substituted by: $\boldsymbol{p}_{k+1} = \boldsymbol{p}_k - \gamma(t_k) * \widehat{g(\boldsymbol{p}_k)}$. Where $\widehat{g(\boldsymbol{p}_k)}$ is an approximation of the true derivative and γ denotes a monotone decreasing function dependent on t_k. "Time" t_k has its value adapted dependent on the inner product of $\widehat{g(\boldsymbol{p}_k)}$ and $\widehat{g(\boldsymbol{p}_{k-1})}$ and is defined as: $t_{k+1} = \max(\, t_k + f\big(-\widehat{g(\boldsymbol{p}_k)}^{\mathrm{T}}\, \widehat{g(\boldsymbol{p}_k)}\big), 0)$ where f is a sigmoid function. This optimization method was introduced[64] by the developers of the image registration toolbox: elastix and it is one of the most commonly used methods for registration schemes implemented with the aforementioned toolbox. The same study[64] concluded that the adaptive step size mechanism of ASGD improved the robustness for a wider range of algorithm's user-defined parameters.

2. Quasi-Newton (QN) is a method that attempts to accumulate information from previous iterations and utilizes it in order to speed up its convergence. QN uses second-order information and more specifically an approximation of the inverse Hessian matrix $\widehat{H}^{-1}(\boldsymbol{p}_k)$ in order to define the direction of search for Eq.3.8 as follows: $\boldsymbol{d}_k = -\widehat{H}^{-1}(\boldsymbol{p}_k)\, g(\boldsymbol{p}_k)$. The exact computation of the inverse of the Hessian matrix is avoided since it would be computationally very expensive, especially for high-dimensional optimization problems. QN usually has a convergence rate higher than that of GD.

3. Levenberg-Marquardt (LM) is a method closely related to the families of Newton and Gradient based optimization methods and defines the search direction for Eq.3.8 as follows: $\boldsymbol{d}_k = -(\widehat{H}^{-1}(\boldsymbol{p}_k) + \zeta \boldsymbol{I}) g(\boldsymbol{p}_k)$, where $\boldsymbol{I}$ is the identity matrix and ζ is a weighting factor that acts as a regularizer taking into consideration the speed and stability of the algorithm.

A more thorough review of optimization methods for medical image registration can be found in the study from Song et al[49].

3.2 elastix: medical image registration toolbox

elastix[4] is one of the most widely-adopted software packages for medical image registration among others (SPM[58], AIR[59], ITK[60], SimpleITK[65], SimpleElastix[66] and ANTS[61]) and it was utilized to carry out all the registration experiments conducted for this study. Apart from the basic registration modules: transformation models, cost functions and optimization methods (whose role in an image registration problem has been covered extensively in the previous paragraph), elastix also provides two more modules: interpolators and multiresolution schemes. A schematic overview of the elastix registration components and their relations as introduced in study[62] are shown in Fig.15, a short summary for each component[62] follows:

Cost function:

elastix solves a minimization problem (as formulated in Eq.3.1) for a user defined cost function: C via an iterative optimization method. Hence the goal is to minimize the distance between the target image: $I_F(x)$ and the warped version of the moving image: $I_M(T_{\mu k}(x))$ where $T_{\mu k}(x)$ is the transform calculated by the k^{th} iteration and μ is the vector of the transform parameters. elastix provides a significant number of cost functions including mean squared differences, normalized cross-correlation, mutual information and normalized mutual information.

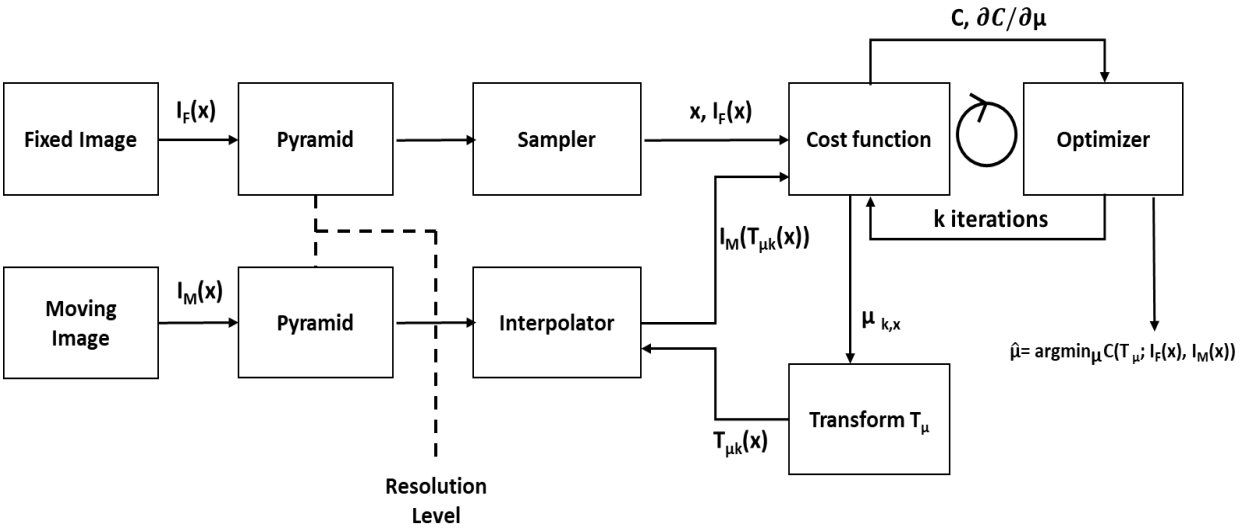

Figure 15: Scheme of the basic registration components for elastix. $T_{\mu k}(x)$ is the transform calculated by the kth iteration, μ is the vector of the transform parameters and C is the cost function that measures the dissimilarity between the fixed $I_F(x)$ and the deformed moving image: $I_M(T_{\mu k}(x))$.

Transformation:

The parametrization of the coordinate transformation T_μ determines the degrees of freedom of the deformation. elastix supports all kinds of linear transformations mentioned in paragraph 3.1 and for the non-linear transformations it provides an implementation of B-Splines. The B-Splines implementation models the transformation as a weighted sum of B-Spline basis functions placed on a uniform grid of control points explained in paragraph 3.1.1. The control point spacing for the grid is a user defined parameter which dictates the transformation's flexibility.

Optimization methods:

In order to find the optimal vector of parameters μ for the transformation T, an iterative optimization procedure is performed by elastix. In every iteration k, the current vector of transformation parameters μ_k gets updated by taking a step in the search of direction. elastix includes a large number of optimization methods including gradient descent, quasi-Newton, conjugate gradient descent and several alternations of stochastic gradient descent. To reduce the computation time elastix also provides the option to only use a subset of the image's voxels to compute the cost function derivative, the module responsible for this process is the sampler.

Interpolators:

The computation of the cost function requires the evaluation of $I_M(T_{\mu k}(x))$ at non-voxel positions, hence an interpolation process is needed, the module responsible for this is the interpolator. The interpolators provided by elastix are: nearest neighbour, linear and N^{th} order B-Spline interpolation (with $1 \leq N \leq 3$).

Hierarchical strategies:

elastix offers several approaches for hierarchical (multiresolution) image registration. In Fig.15 the multiresolution approach is represented by the module named "Pyramid". The main hierarchical strategies provided by the toolbox are combinations of Gaussian pyramids with and without downsampling. In order to form a typical Gaussian pyramid, Gaussian smoothing with increasing scale and downsampling of the previous level is performed. The most important advantage of a pyramid in a registration scheme is that it decreases the processing time, as less calculations are needed for the initial stages (where the images are smaller), making it an appealing option for slower algorithms. Nevertheless, part of the same process is the upsampling that needs to take place between levels, forcing an

interpolation of the transformation. More specifically, the interpolated transformation from the previous level is utilized as the initial transform for the current level, however since interpolation is a non-optimized process it may introduce artefacts in the deformation field.

An additional multiresolution strategy (not depicted in Fig.15) is offered by elastix only for the non-rigid registrations (B-Splines). It allows the increase of the transformation model complexity by enabling the iterative process of registration to work with uniform grids of variable control points spacing. This way starting from lower resolutions a coarse grid is utilized to compensate for gross motion artefacts while as resolutions get higher the grid gets refined enabling finer deformations.

3.3 Registration methods for multiparametric MRI

Over the last few years a plethora of registration methods have been proposed for medical imaging. However, the motion correction of multiparametric MRI remains one of the most challenging applications due to the combination of breathing induced artifacts and the massive image intensity differences between MR sequences caused by changing MR contrast mechanisms used to capture specific tissue properties. Some MRI registration methods utilize information from physiological models within the registration pipeline itself (model-driven registration or MDR) while others do not rely on this information (model-free methods).

3.3.1 Model-free motion correction approaches

Below follows a brief review of model-free motion correction techniques that includes the following categories:

Methods that implement intensity-based co-registration using as targets a certain subset of the MR acquired data. Characteristic examples include motion correction techniques for DCE-MRI data that considered using as targets either a specific image from the acquired sequence to perform registration for 2D[67] or a chosen volume for 3D[68, 69] respectively. A similar approach was also described in[70] for motion correction of MOLLI CMR image series, where the last time frame of the sequence (the one with the longest inversion time), was used as a reference image. These methods are limited to MRI sequences with minor changes in contrast, since they proceed straight to an intensity-based registration.

In order to avoid choosing specific registration targets there are some methods that proceeded to group-wise registration of the acquired set of images, registering all the images simultaneously to a common "mean space". An example of such method is study[71] on T1 MRI brain scans, which used an entropy based cost function combined with a constraint reassuring that the average deformation is the identity transform to successfully register brain MRI scans. A relevant study on renal RADIAL VIBE DCE[72] proposed an alternation of the GRASP reconstruction method, that removed the spokes corrupted by motion. This novel reconstruction method was utilized as an additional step before proceeding to the group-wise registration of the reconstructed images. However, the applications of this method are limited to RADIAL VIBE acquisitions.

Another category of model-free methods includes approaches that apply data decomposition methods on the acquired images to disentangle the intensity changes due to motion from those due to changing MR contrast mechanisms (i.e. contrast administration) and then proceed to the registration process. One of the most well-known methods for this category is the method presented in the study[73] where Principal Components Analysis (PCA) was used to analyze the acquired images to their principal components and then reconstruct synthetic motion-free images utilizing only the first principal components. The acquired images were then pair-wise registered on their respective synthetic counterparts. After this first registration, a new set of synthetic target images was created using the newly registered data and the process was iterated until convergence. The authors of the study found that the method's effectiveness may be affected by the presence of periodic motion, which could appear in the first principal components. Similarly, methods[74, 75] utilized Robust-PCA to split the data to their low-rank (representing smoothly varying global changes) and sparse components (representing rapid local changes), with the former being assumed to capture the motion effect. The low-rank components of the data were then utilized in group-wise registration schemes to avoid being affected from changes in images' contrast. The authors of study[70] noted that the assumption that motion should appear in the low rank components may be limiting for local rapid motion elements that occur over a short period of time. Another interesting method that heavily relies on data decomposition is the one introduced by Tirunagari et al[76] that used Dynamic Mode Decomposition (DMD) to decompose image sequences into sets of dynamic modes. The most significant modes captured slow-varying changes for example changes in contrast and the least significant modes captured fast-varying changes like motion effects. Initially, DMD was applied on overlapping windows of sets of 3 successively acquired images. The most significant modes produced by this application of DMD were concatenated together and DMD was applied again on them. The three most significant modes produced by the later application of DMD were used to reconstruct a set of motion corrected images. However, a critical parameter for this process is the size of the windows for which authors proposed a constant value, the lack of a dynamic criterion capable to tune this parameter on the patient's breathing cycle indicates that the method may lack robustness and generalization capability.

Finally, there is a method introduced by Huizinga et al[77] that lies in the intersection of the last two categories. This study performed group-wise registration of the originally acquired images by minimizing a novel cost function that was based on a data decomposition technique (PCA). This state-of-the-art approach has achieved excellent results for quantitative MRI[77] (T1, T2, ADC, DTI and DCE) and it will be

compared against model-driven registration in chapter 5 as a potential candidate for universal motion correction in renal quantitative MRI. A more detailed review of the method follows below:

PCA-based group-wise registration:

Study[77] introduced a registration method based on the fact that intensity changes take place according to low-dimensional physical models, while once motion has corrupted the data their complexity gets increased and the same models can no longer describe them sufficiently. Hence, a novel dissimilarity metric based on PCA was introduced to quantify the amount of misalignment in the set of images by focusing the attention on the first few principle components, which were expected to represent the low-dimensional physical model free from the "noise" introduced due to motion.

This technique treats all the images equally, hence the order in which the images are fed to the algorithm has no effect on the value of the dissimilarity measure or the registration results in general. Given a set of $n = \{1, 2, \dots, N\}$ acquired images, denoted with M (for moving images) in PCA-based group-wise registration the images M_n (for all n) are registered simultaneously to a common "mean space". From this process a transformation $T(\boldsymbol{\mu}_n)$ for each image of the set is calculated, where $\boldsymbol{\mu}_n$ is the image specific vector of transformations parameters. Hence, this problem can be formulated as the minimization of a dissimilarity metric D_{PCA} with respect to $\boldsymbol{\mu}$ as follows:

$$\hat{\boldsymbol{\mu}} = \underset{\mu}{\operatorname{argmin}}\, D_{PCA}(\boldsymbol{\mu}) \tag{3.9}$$

where $\boldsymbol{\mu}$ is a vector of transformations parameters constituted of all the respective $\boldsymbol{\mu}_n$. In this case the dissimilarity measure calculates the dissimilarity of all transformed images $M_n(T(\boldsymbol{\mu}_n))$ with respect to each other and the parameters $\boldsymbol{\mu}_n$ are optimized simultaneously for all n.

The novelty of this approach lies mostly on the use of D_{PCA} as the dissimilarity metric, a short description of this metric is given below:

Given a set of acquired images M_n, they can be represented as columns in a $P \times N$ matrix denoted with $\boldsymbol{M}$, where P is the number of pixels of a single M_n image.

Then the covariance matrix of $\boldsymbol{M}$ is defined as:

$$\boldsymbol{C} = \frac{1}{P-1} * \boldsymbol{M}^T * \boldsymbol{M} \tag{3.10}$$

The above can be formulated further in order to make the observations zero-mean:

$$\boldsymbol{C} = \frac{1}{P-1} * \ (\boldsymbol{M} - \bar{\boldsymbol{M}})^T * (\boldsymbol{M} - \bar{\boldsymbol{M}}) \tag{3.11}$$

where $\bar{\boldsymbol{M}}$ stands for a matrix same size as $\boldsymbol{M}$, which has in each column all elements equal to the average value of the respective $\boldsymbol{M}$ column.

Then the correlation matrix is defined as:

$$\boldsymbol{K} = \frac{1}{P-1} * \ \boldsymbol{\Sigma}^{-1} * \ (\boldsymbol{M} - \bar{\boldsymbol{M}})^T * (\boldsymbol{M} - \bar{\boldsymbol{M}}) * \ \boldsymbol{\Sigma}^{-1} \tag{3.12}$$

where $\boldsymbol{\Sigma}^{-1}$ denotes the inverse of the diagonal matrix of the standard deviations for each column of $\boldsymbol{M}$.

The proposed dissimilarity metric is based on the fact that when motion has corrupted the quantitative MRI data, they can no more be described properly just by their respective physical models, a fact that has an effect on the spectrum of eigenvalues of $\boldsymbol{K}$. More specifically, the following behavior was observed: calculating the eigenvalues of $\boldsymbol{K}$ for properly aligned images leads to larger scalars only for the first few eigenvalues with those that follow being much smaller. On the contrary the respective calculation for misaligned images showed that the following eigenvalues got relatively higher values. Based on these observations the dissimilarity metric aims to transform the images in a way that will make the spectrum of $\boldsymbol{K}$ to approach that of an aligned image set as described by the formula below:

$$D_{PCA}(\boldsymbol{\mu}) = \sum_{j=1}^{N} j * \ \lambda_j(\boldsymbol{\mu}) \tag{3.13}$$

This way the first eigen values which have lower indices have also lower weights assigned to them, while those that follow have higher weights (their values are more important for the dissimilarity metric). Given that $\sum_{j=1}^{N} \lambda_j = N$ (where N is the trace of the correlation matrix) this metric aims to end up having as much variance as possible explained by a few large eigenvectors. The dependence of the metric on $\boldsymbol{\mu}$ is used to clarify that the eigenvalues λ_j of $\boldsymbol{K}$ are calculated on the deformed version of the images. Finally, the PCA is performed on the correlation matrix $\boldsymbol{K}$ instead of the covariance matrix $\boldsymbol{C}$ to avoid sensitivity on intensity scaling between images (correlation is a standardized function of covariance).

3.3.2 Model-driven motion correction approaches

Model-driven motion correction techniques integrate physical models that properly describe the function of the organ of interest in the registration process itself. More specifically, most model-driven methods utilize a physiological model fit to create motion-free target images and subsequently perform a pair-wise

co-registration. Following that a model-fitting on the newly registered data initiates a new iteration of the process which is repeated until convergence. The above described process will be referred to as the typical model-driven registration (MDR) scheme for the rest of the text. Model-driven registration techniques have been applied in a range of MRI data for a variety of organs:

The first study that introduced an MDR scheme is form Hayton et al[78] for 2D registration of breast DCE-MRI. This study proposed the use of a pharmaco-kinetic model for contrast uptake, combined with a free-form deformation algorithm. A dedicated breast coil was used during the acquisition of the data for this study, limiting the motion induced artifacts.

A large number of model-driven motion correction methods initiate their pipeline with an initial registration step before proceeding to the typical MDR iterative scheme described above. This strategy is quite common among model-driven registration methods for cardiac MRI[79], [80], [81], [82]. Study[79] focused on Dynamic Cardiac Perfusion MRI (ECG-triggered acquisition with breath-holding) and proposed the utilization of a two-compartment model to create artificial target images. Initially, all images were registered to a single reference frame, which was chosen to have sufficient contrast uptake and good contrast between the myocardium and the ventricle blood pools. Following that, a typical MDR scheme with pairwise translational (rigid-body) transforms was performed. A similar approach was introduced for MOLLI T1 cardiac MRI[80] (for breath-holding and free-breathing acquisitions), the method begins by considering all pair-wise affine registrations between the acquired images to find an optimal reference frame and then registers (with affine transforms) every other image to that. After this initial registration a typical MDR was performed to achieve a non-rigid refinement. Another study in MOLLI T1 cardiac MRI[81] (ECG-triggered acquisition with breath-holding) used a MOLLI inversion recovery model to initiate an iterative process of co-registration on synthetic target images. The process began by registering together the images with the shortest and longest T1 in order to obtain a crude initial T1 estimate and calculate the first set of synthetic images for the model-driven registration. The optimization process minimized an energy function dependent on: the distance between the synthetic images and the originally acquired images, the model fit error and a regularization term. In the same category belongs study[82] which began the pipeline with a preliminary rigid registration, where each image was registered on its own target image. The individual target images were calculated as the average of the image before and right after the current image. Following the initial rigid transform a typical non-rigid MDR scheme was performed, however this approach was found to produce poorer results in cases that were corrupted by larger amounts of motion.

Deviating from the pattern of model-driven methods for cardiac MRI described above, study[83] on Look-Locker T1 cardiac MRI did not perform any initial registration steps and proceeded straight to a typical MDR scheme utilizing the model fitting error to spatially align the acquired images. This study resembles more registration approaches utilized for abdominal MRI, which often choose to proceed straight to the typical MDR scheme based on non-rigid transforms, skipping the additional preliminary registrations based on rigid transforms. These methods skip the preliminary rigid registration step, since non-rigid transforms have the required complexity to compensate for both rigid and non-rigid motion. Characteristic examples of this category of methods are the two studies from Buonaccorsi et al.[84, 85] focused on registering tumorous DCE-MRI liver data. Both studies described a similar pipeline that performed a two-compartment filtration model fitting on the data to create 3D synthetic (motion-free) image volumes initiating a typical MDR scheme. The registrations performed were rigid boy (translations) and were calculated based only on the similarity measurements within a tumor VOI (that was defined manually). An important note is that the rigid body registration performed was found to be occasionally insufficient to fully recover tumor motion, which often included warpings and other non-rigid body deformations. Similarly, a recent method[86] also followed a typical MDR scheme to perform (non-rigid) free form deformation transforms (modeled with B-Splines) to compensate for motion artifacts on placental DWI MRI. This study stands out for two reasons: first it is the only work found (to the best of our knowledge) to compare the registration results of a model-driven technique with those of a model-free[73], concluding that the model-driven registration performs better. Second, it is one of the few model-driven methods that has successfully registered free-breathing acquired data and has utilized a single model that combined T2 relaxometry and DW imaging which constitutes an indicator that MDR can be applied successfully on more than one MR modalities. However, it should be noted that DWI MRI exhibit limited changes in contrast making it a more manageable case than other MR modalities like DCE-MRI. The same claim applies for study[87] that focused on registration of free-breathing DWI MRI of the abdomen performing a simultaneous joint optimization for: the registration process (typical non-rigid transform MDR scheme) and the model-parameters estimation.

Some other registration methods chose to resort to a probabilistic formulation of the registration problem incorporating information form the respective physiological models. Study[88] presented a motion correction technique with joint estimation of motion parameters and T1 maps for Inversion-Recovery (IR) brain T1 MRI data. More specifically, this approach solved a maximization problem of the maximum likelihood criterion, where the IR model parameters and the transformation parameters were calculated

so that the observed data were most probable. This process combined models of T1 relaxation, motion and noise into a single statistical model for the T1-weighted maps. The transformations calculated were translational (rigid-body), while the noise corrupted acquired data were modelled by the Rice distribution. Similarly, study[89] on colorectal cancer DCE-MRI images proposed a registration scheme that performed a simultaneous motion correction and model-parameter estimation. This approach performed an optimization based on the maximization of the joint posterior probability of: the parameters of the model that best fitted the data and all the transformations needed to deform the image sequence in order to achieve spatial correspondence.

Finally, a study from Enescu et al[90] formulated and solved a discrete optimization problem that incorporated model information in order to register DCE-MRI data from patients with rectal tumors. To address such a problem the first step was to define an undirected graph, in this case the nodes represented voxels (or group of voxels) and edges connected voxels with similar anatomical features and spatial proximity. For this approach each node had a set of labels representing the possible discrete displacements of the voxels constituting the source image with respect to the respective target image volumes. In order to calculate the optimal displacement for each node (group of voxels) an energy function consisted of two terms was minimized. The first term was a regularization cost that penalized non-smooth displacements of directly connected nodes and the second was a distance metric between the intensities of the volume to be registered and the respective model-predicted intensities.

The majority of the model-driven methods described above have processed data acquired using gating, breath-holding, dedicated coils, MRI data with limited contrast changes or other techniques that laid the ground for a more easily addressable registration problem. Furthermore, each model-driven method analyzed above was applied on a single MRI modality. Hence, to the best of our knowledge it has not yet been tested whether a single set of registration parameters could be combined with different physiological models to form a universal MDR approach for multimodal renal MRI (including free-breathing acquisitions). An attempt to develop such a universal MDR approach and also compare it against a state-of-the-art model-free group-wise registration method[77] on T1, DTI and DCE renal MRI data will be presented in chapter 5.

3.3.3 Deep Learning based motion correction approaches

Apart from the traditional approaches examined in sections 3.3.1, 3.3.2 there is also another category of solutions that utilizes artificial intelligence and more specifically deep learning to address the problem of motion correction for the field of medical imaging. In a broader sense the vast majority of deep learning based approaches falls under the category of model-free registration since they do not utilize any pathophysiological model related information. However, deep learning approaches are examined in a separate paragraph since they solve the problem using an optimization process that aims to properly train a (deep) neural network to address the registration problem. A short review of architectures that have been specifically developed for the motion-correction of medical images follows:

Sloan et al[91] in a relevant study performed rigid image registration for mono and mutli-modality cases for T1 and T2-weigthed MRI brain scans. Two separate architectures were developed and tested for both modalities: a convolutional neural network (CNN) with fully connected layers at the end of the model and a fully convolutional neural network[92] (FCN) (both networks included skip connections to assist the extraction of richer set of features from the images). The conducted experiments showed that the proposed architectures produced results comparable to a multi-scale, iterative registration scheme implemented in SimpleITK[65].

Another architecture designed specifically for medical image registration is DirNet[93] (FCN type), which was trained in an end-to-end unsupervised way, by optimizing an image metric between the fixed and transformed moving images. This way a 2D grid of control points of cubic B-Splines representing the spatial transformation gets estimated and then applied on the moving image to properly deform it. DirNet consists of the following modules:

- a CNN which takes as input a fixed and a moving image and estimates the spatial transformations in x and y axis, generating a deformation field
- a spatial transformer module based on spatial transformer network[94], which takes as input the deformation field and with the use of a cubic B-Spline resampler module produces the warped moving image.

DirNet was applied on cardiac cine MRI scans and it was found to perform equally well with a conventional deformable image registration method (implemented in SimpleElastix[66]), with a substantially shorter execution time.

Shan et al[95], presented a FCN with an encoder-decoder architecture based on FlowNet[96], which was able to perform 2D-registration in an unsupervised way. The FCN takes as input a fixed and a moving image and calculates a deformation field. The deformation field is utilized by a "sampling grid generator" module in order to deform a regular spatial grid, which was then used to warp the moving image. The difference between the warped moving image and the fixed image was then back-propagated to train the network. This approach was tested on T1-weighted brain MRI and liver CT data producing state of the art results for the first case (MRI) and results comparable to traditional approaches for the later one (CT).

An unsupervised model for deformable image registration was introduced by Balakrishnan et al[97], which succeeded in registering 3D-MRI brain scans. The network was based on the UNet[98] architecture. Hence, it follows an encoder-decoder architecture with skip connections that generates a 3D-registration field (ϕ). ϕ is then fed into a spatial transform module (which is based again on spatial transformer networks[94] and performs a trilinear interpolation (3D linear interpolation) in order to estimate the warped moving 3D-image. Afterwards the loss function is calculated and back-propagated in order to train the network. This architecture achieved comparable results to a traditional registration scheme implemented in ANTS.

Another study introduced[99] a self-supervised FCN network in order to register T1-weighted MRI brain images. The proposed approach directly trained the network to estimate voxel-to-voxel spatial transformation for registration purposes (3D-registration) by maximizing a similarity metric. This network included a spatial type of convolutional layers called "regression layers", whose output has the same size as their input (in the spatial domain) and multiple channels that encode the displacements for each spatial dimension of each image. This architecture performed better than a conventional registration scheme implemented in ANTS.

Moreover, in another study[100] a VGG-Net[101] (FCN) was used to calculate a transformation between fixed and moving 3D-images. The transform was modeled as a thin plate spline where all the needed coefficients were computed by the displacements estimated by the CNN. This network relied on learning synthetic transformations applied on a small set of representative (for the given registration task) images and it was tested on lung CT data.

A much more thorough review of Deep Learning solutions for medical image registration can be found in the recent review paper from Chen et al[102].

Chapter 4

Pilot study – initial implementation of model-driven registration

4.1 Introduction

This chapter briefly presents an initial implementation of a model-driven (MDR) registration method for renal DCE-MRI based on study[39] with the use of elastix and Python. The focus was set on DCE-MRI since it is one of the most modalities for renal MRI combining free-breathing acquisition with massive changes in image contrast due to the contrast passage. 3 videos from healthy volunteers were selected for the conducted experiments, representing a typical example of high breathing motion (free breathing acquisition), a case with medium and low breathing motion respectively (Fig.16). The main goals for this pilot study were:

1) To verify that the elastix - Python implementation of the code works properly.
2) To perform some initial registration experiments that would help identifying potential soft spots of the method in order to improve them. Hence, this initial set of experiments served as a starting point for the development of a more robust implementation of MDR (presented in chapter 5), that could be utilized as a universal motion correction approach for renal quantitative MRI.

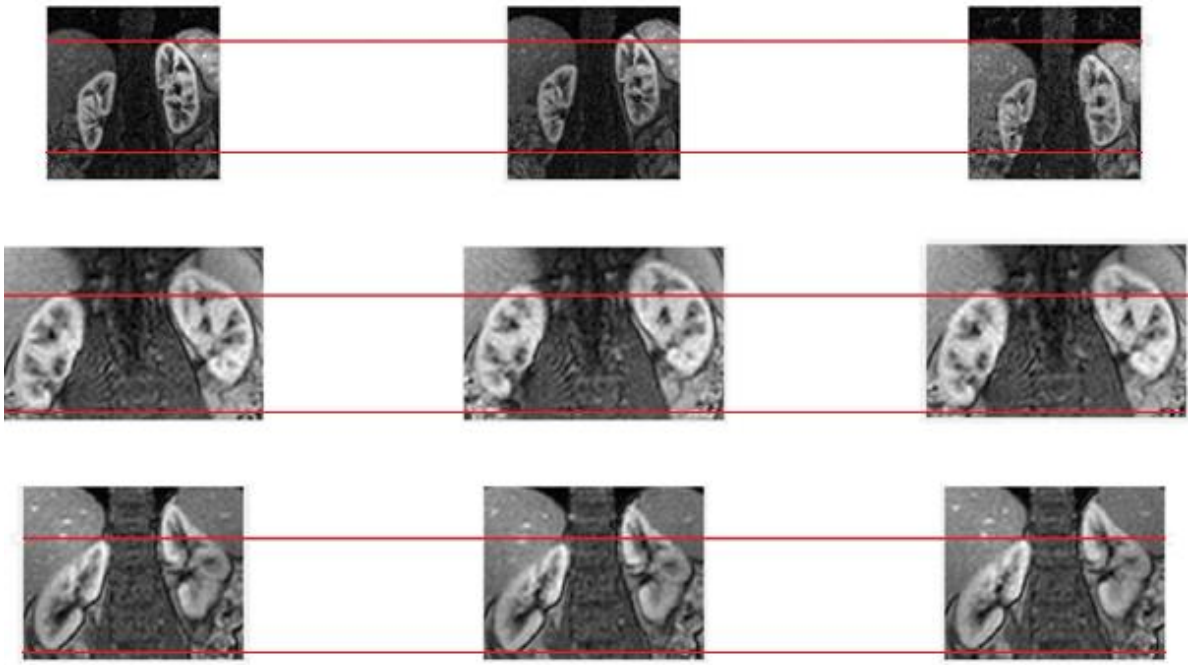

Figure 16: Illustration of the motion to be corrected for 3 different DCE-MRI datasets. ***Top row***: DCE data with high breathing motion (free breathing). ***Middle row***: DCE data with medium breathing (shallow breathing) motion. ***Bottom row***: DCE data with low breathing motion (shallow breathing).

The algorithm was developed in Python with the use of elastix[4] and is completely data-driven, the only assumption made is that the acquired data comply with a physical model (in this case the 2CFM, paragraph 2.3.5). MDR has successfully addressed the issue of using a fixed reference image (S_0) as a target for the registration of DCE-MRI data, which include massive changes in image contrast due to the bolus passage. MDR results are compared to those of a simplistic approach performing an intensity-based pairwise image registration to a single target image.

4.2 Methods

MDR's basic principle is illustrated in Fig.17. Given a set of N acquired frames, measured with N sets of imaging parameters, a new set of N registered frames is created by iterating two steps: (1) the current set of N registered frames is fitted pixel-by-pixel to the signal model, producing N fitted frames; [94] these are used as targets for a frame-by-frame registration of the N acquired frames, producing a new set of N registered frames. For the first iteration the N registered frames are initialized to the N acquired frames.

Dataset

The DCE-MRI data were drawn from renal pilot studies measured in 2 centres, on 2 different 3T scanners (Siemens, Philips). MR renography was performed in both centers with a 2D-turbo flash sequence at 3T (Slices: 4, Matrix size: 480 (squared), Slice thickness: 8mm, FOV: 441 mm, Temporal resolution: 1.1s, FA 12°, TR/TE 3.5/1.6ms). A standard dose of a macrocyclic contrast agent was injected. The DCE-MRI data used for the experiments of this chapter were kindly provided by Peter Thelwall, Jehill Parikh and Neil Sheerin (Newcastle University) and by Patrick Mark and Alexandra Radjenovic (Glasgow University).

Model-fitting

The pixel by pixel model fitting was performed using a two-compartment filtration model[40] and Levenberg-Marquardt optimization. An arterial input function was selected in the aorta on the transverse slice. The equations that describe the two-compartment filtration model used for the linear least squares fit were analytically described in paragraph 2.3.5 and in the study from Flouri et al[40].

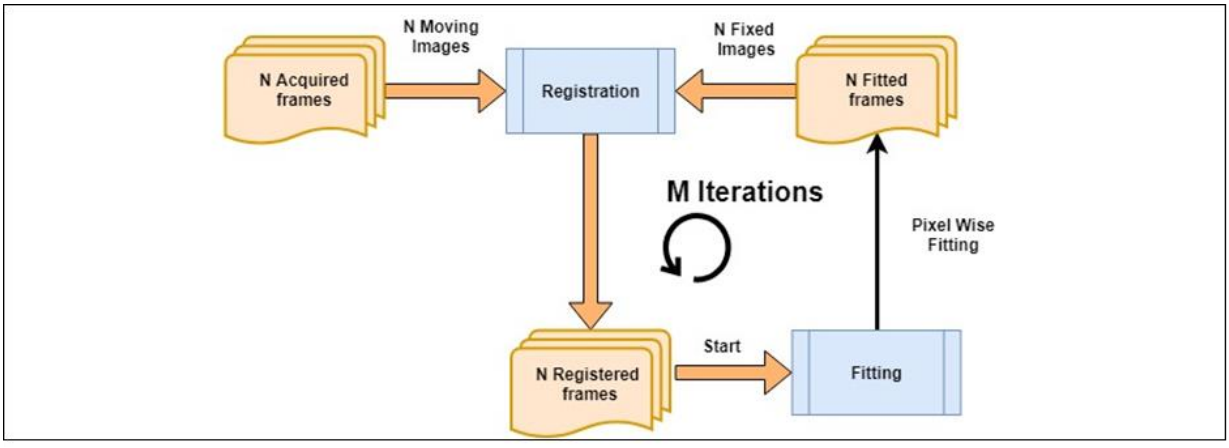

Figure 17: Model driven registration (MDR) – basic architecture. Initialization: for the first iteration the N registered frames were initialized to the N acquired frames.

	High Motion (free-breathing)	Medium Motion (shallow-breathing)	Low Motion (shallow-breathing)
ITERATIONS - RESOLUTIONS	3 iterations 4 resolutions each	2 iterations 4 resolutions each	1 iteration 4 resolutions
FINEST RESOLUTION GRID SPACING PER ITERATION	1st iter: 100mm. 2nd iter: 50mm. 3rd iter: 25mm.	1st iter: 50mm. 2nd iter: 25mm.	1st iter: 25mm.

Table 4: Breathing motion and grid spacing for each of the 3 DCE-MRI datasets processed. The grid spacing is halved after each iteration for all 3 cases.

Registration

The image registration process was implemented in elastix[4] following a multi-resolution strategy (4 resolution levels), applying a free-form deformation transform (non-rigid B-splines) and a mutual information based similarity metric with adaptive stochastic gradient descent optimization[64] scheme.

Due to lack of a more sophisticated stoppage criterion and since a different amount of motion had corrupted each set of images, a different number of MDR iterations took place for each case (a summary of these details can be found in Table.4). Apart from the internal mutli-resolution scheme of elastix, the finest resolution grid spacing was halved after each iteration of MDR to perform gradually finer registrations.

As a baseline method and comparator for MDR, a more simplistic conventional approach was also applied to the data, this approach used a single fixed reference image as a target to register all time frames. The mean of the time-frames before contrast arrival was chosen as the fixed reference image and all registration parameters were kept the same as in MDR to enable a fair comparison.

4.3 Results

The two registration approaches were compared on the same 3 volunteer datasets that were described previously. Figs.18, 19 show semiquantitative (Maximum Enhancement Maps) and quantitative (Renal Blood Flow, RBF) parameter maps for all 3 motion cases: no registration, reference image registration and model driven registration (MDR), respectively. Both figures show that MDR drastically reduces motion artifacts in the case of high motion, but the registration effect is less pronounced in low and medium motion cases. The RBF maps were calculated by performing a final extra fitting step on the motion corrected data.

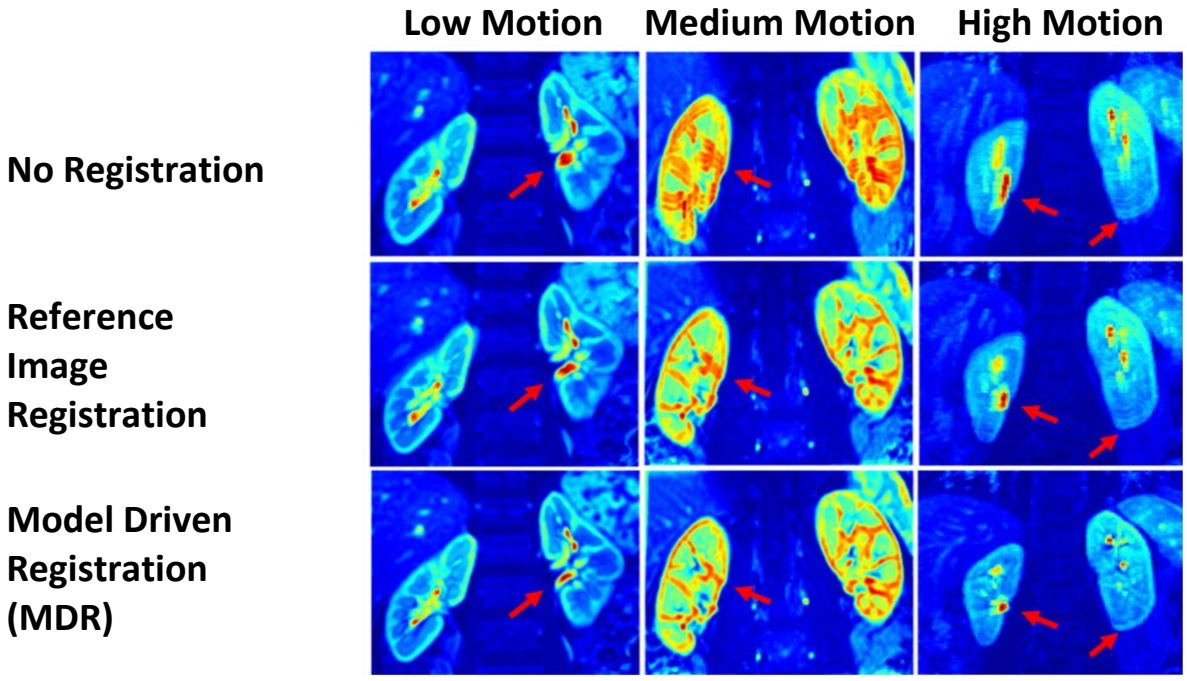

Figure 18: Maximum Enhancement Maps (MEMs) for the compared approaches. Top row: Maximum enhancement maps (MEM) for low (left panels), medium (mid-panels), and high (right panels) breathing motion (before registration). **Middle row:** MEMs with image registration using reference approach. **Bottom row:** MEMs with image registration using proposed model driven registration approach. The red arrows red arrows indicate areas of the images where the motion correction effects are more pronounced.

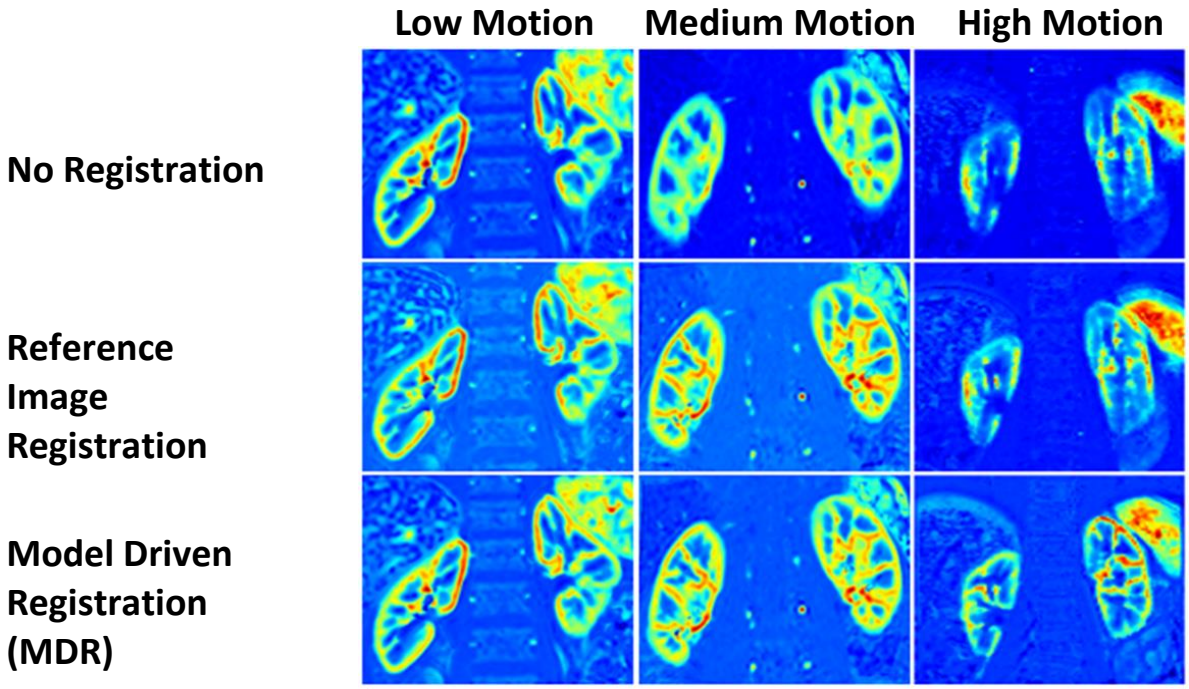

Figure 19: Renal blood flow maps extracted from the registered data with the compared approaches. Top row: Renal Blood flow (RBF) maps for low (left panels), medium (mid-panels), and high (right panels) breathing motion (before registration). **Middle row**: RBFs with image registration using reference approach. **Bottom row**: RBFs with image registration using proposed model driven registration approach.

4.4 Conclusion

The results demonstrate that MDR even in this early form can achieve a noteworthy reduction in motion artifacts for cases of high breathing motion, while the benefit is minimal when breathing motion is shallow, in which case a faster reference-image approach may be sufficient.

The first observations made during the experimental process concerned the computational time needed. More specifically, the use of a model target came at the cost of significant computation time due to the model-fitting process integrated in the MDR scheme. Additionally, this initial implementation of MDR is relied on a fixed number of iterations per case regardless of the improvements achieved at the intermediate steps. This practically means that there is always the possibility for the algorithm to perform excessive computations prolonging the computational times further.

The visual inspection of the intermediate results produced at the end of each MDR iteration revealed that the choice of 100mm. as the finest resolution grid spacing for the 1st iteration of the high motion case did not improve the results significantly. While, the 25 mm. grid spacing for the finest resolution of the last iteration, could be lowered even further for all 3 cases to allow more detailed local deformations. The room for improvement is evident on the lower pole of the left kidney for the low motion RBF map and the lower pole of the right kidney for the high motion RBF map where the edges of the kidney cortex remain a bit blurred (Fig.19). An intuitive conclusion based on the above observations is that the decrease of the finest resolution grid spacing after every iteration of MDR could be avoided, if a fixed but smaller finest resolution grid spacing was set for the internal elastix multiresolution scheme.

Hence to address all the aforementioned issues the following improvements should be implemented:

1) There should be examined whether there are technical ways that would allow the reduction of the computational time needed for the model-fitting process of MDR. The parallelization of the aforementioned process can be considered as a potential improvement to reduce the computational time needed (chapter 5).
2) The set of MDR's registration parameters should be refined with a special focus on the tuning of the elastix internal multiresolution scheme. A suitable modification of the number of resolutions used and the finest grid resolution could make the externally imposed decrease of the finest resolution grid spacing after each MDR iteration unnecessary, leading to a reduction of the overall algorithm complexity.

3) A dynamic automated stoppage criterion should be developed in order to identify when MDR has converged. This would increase the robustness and the effectiveness of the algorithm while eliminating the need for the user to choose the number of algorithmic iterations on a patient basis. Ideally such a criterion should be in position to halt the process when the displacement vectors produce are small enough (i.e. less or equal to single pixel distance).

The aforementioned requirements were addressed in order to develop a more robust, efficient and faster implementation of MDR that could serve as a universal registration approach for multi-parametric renal MRI, the improved version of MDR is presented in chapter 5.

Chapter 5

Comparison of model-free and model-driven registration for multiparametric renal MRI

5.1 Abstract

Dedicated registration methods for motion correction of quantitative MRI can be classed as either model-driven registration (MDR) or model-free registration (MFR). The aim of this study was to verify the hypothesis that MDR is more suitable for quantitative MRI by comparison against state-of-the-art group-wise MFR (GMFR). The comparison was performed in the challenging setting of renal MRI. Motion-correction was applied to breath hold T_1-mapping, free-breathing diffusion tensor imaging (DTI) and free-breathing dynamic contrast-enhanced (DCE) MRI data from 10 consecutive patient cases. Co-registration in MDR and GMFR was performed in elastix using free-form deformation and the same registration parameters. The quality of registration was measured with 8 scores calculated on each of the 3 types of data: chi-square difference with the model fit (CS), coefficient of variation (CV), standard deviation (STD) of the 2nd derivative, and the interquartile range (IQR). Statistical significance of differences between MDR and GMFR was assessed with Wilcoxon signed rank test (significance at $p<0.05$ with Bonferroni correction). Computational times were measured on a standard laptop PC. MDR and GMFR were significantly different in 10 of the 24 scores, and MDR scored better in 9 of those including all DTI and DCE metrics. Differences between MDR and GMFR were generally modest (<20%), but significantly larger for the more challenging free-breathing DCE data with large contrast changes. GMFR is on average 1.5 min per subject faster than MDR for T1-mapping, but 230 min slower for DTI and 955 min slower for DCE. Model-driven registration was found to perform better for the majority of the evaluation metrics than a state-of-the-art model-free method for motion correction of quantitative MRI in the kidney, with modest improvements in registration accuracy and major reductions in computation time. The benefits of MDR are anticipated to translate to other applications, but this remains to be demonstrated.

5.2 Introduction

Quantitative MRI allows non-invasive measurement of imaging biomarkers for assessing tissue structure and function in vivo[103]. Examples of MRI biomarkers include electromagnetic tissue properties such as the longitudinal relaxation time (T1) measured by MRI relaxometry, microstructure parameters such as the Fractional Anisotropy (FA) measured with Diffusion Tensor Imaging (DTI), and hemodynamic parameters such as tissue blood flow measured with Dynamic Contrast Enhanced (DCE)-MRI.

Quantitative MRI requires multiple acquisitions with differing sequence parameters and interpretation by fitting an appropriate physiological model. A key problem in clinical practice is the effect of voluntary or involuntary patient motion (respiration, peristalsis, etc.) between acquisitions, causing a blurring of the anatomy on model-based parametric maps[87, 104, 105]. Techniques like triggering, gating and breath-holding can be applied to mitigate motion artifacts but this can extend the acquisition time and/or require valuable data to be removed. Moreover, they can cause physical discomfort to the patient and are likely to leave some residual motion. Hence, these methods can be either replaced[86, 87] or combined[79, 81, 82] with image registration techniques. Image registration for multiparametric quantitative MRI is a particularly challenging task since during acquisition the motion effects are combined with substantial changes in both image contrast and signal intensity.

Two types of dedicated image registration approaches have been proposed for quantitative MRI[23, 74] [84, 85]: model-driven registration (MDR) methods that utilize physiological models within the image registration pipeline, and model-free registration (MFR) methods that do not rely on this information. MDR was first proposed in 1997[78] and has since been applied in quantitative MRI of the breast[78], brain[106, 107], heart[79-82], liver cancer[84, 85], abdomen[87, 108], lower abdomen[89, 90], placenta[86], free-breathing DCE-MRI of the kidney[39] and non-MRI application in whole brain PET data[109]. Examples of MFR methods include the use of principal component analysis (PCA)[73], Robust-PCA[23, 74] and Dynamic Mode Decomposition[76]. While other proposals[71, 77] include group-wise MFR (GMFR) where deformation fields at all time points are optimized simultaneously. GMFR has proven to perform well in various applications including T1/ T2 (heart), ADC (abdomen), DTI (brain), DCE (abdomen)[77] and multi-parametric renal MRI[110].

At first glance, MFR methods appear more appealing than MDR because the same algorithm can be applied to multiple MRI modalities and the results are not affected by model bias. However, in the context

of quantitative MRI, motion correction is part of an image processing pipeline that will ultimately always require a physiological model to estimate the imaging biomarkers. From this perspective MFR methods may in fact introduce additional and unnecessary biases, for instance when periodic breathing motion appears in the principal components[73] or when rapid motion elements occur locally over a short period of time[74]. A recent study[86] compared MDR against an MFR method in diffusion-weighted imaging (DWI) of the placenta and demonstrated an improved alignment with MDR. However, it remains to be shown whether these results translate to more challenging multi-parametric settings.

The particular focus of this study is multi-parametric quantitative MRI of the kidney[88], a challenging application area for motion correction due to the large deformable motion amplitudes and strong reversals of contrast. MFR[92] and MDR[39] methods have both been applied successfully to DCE-MRI of the kidney and MFR has been used in the multiparametric setting[110]. However, it is not known how MDR compares to MFR in this application area. The aim of this study was therefore to compare MDR against a state-of-the-art GMFR method in breath hold T1 mapping and free-breathing DTI and DCE-MRI (approximate duration for DCE-MRI acquisition: 7 minutes) of the kidney. If MDR demonstrates a benefit in this area, this would add significant strength to the broader hypothesis that MDR could be considered as the method of choice for motion correction in quantitative MRI.

5.3 Methods

Data acquisition and processing

Multiparametric renal MRI data were obtained from the first 10 patients recruited in the iBEAt study[3]. The subjects were scanned in the morning (8-10 am) after an overnight fast and a standardized meal, on MAGNETOM Prisma 3 T MRI (Siemens Healthcare GmbH, Erlangen, Germany), following the iBEAt protocol[3]. MRI data were exported anonymously and uploaded on a central database in XNAT.

T1-mapping, DTI and DCE-MRI data (Table.5) were used to compare motion correction methods as these provide a broad range of challenges for image co-registration: (1) T1 and DCE show large changes in contrast and intensity whereas DTI shows mainly large changes in intensity; [94] DTI and DCE were acquired in free breathing while T1 was acquired in breath hold; (3) T1 represents a mild computational challenge with only 28 frames per slice, but DTI and DCE are significantly more challenging with 146 and 265 frames per slice, respectively.

	IR-prepared Modified look Locker (T1)	**Spin-Echo EPI (DTI)**	**2d-turbo flash sequence (DCE)**
Acquisition mode	multiple breath-hold	free breathing	free breathing
Number of slices	5	30	9
Slice thickness (mm)	5	2.3	7.5
Field of view (mm)	400	400	400
Flip angle (degrees)	12	90/ 180	10
TR (ms)	506.63	5100	179
TE (ms)	2.32	70	0.97
Number of frames per slice	28	146	265
Acquisition Matrices	192 192	172 172	192 144
Reconstructed Matrices	384 384	172 172	384 384
Additional parameters	Inversion times: [100 – 7700]	b-values: 100, 600 s/mm^2 total number of directions: 146 EPI factor: 172 diffusion scheme: monopolar	quarter of a dose contrast agent: Dotarem/Gadovist

Table 5: Acquisition parameters for IR-prepared Modified look Locker (T1), Spin-Echo EPI (DTI) and 2d-turbo flash sequence (DCE).

The data were downloaded in DICOM format from the central XNAT database. Only the middle slice from each acquired sequence was motion corrected. The experiments were conducted using a laptop PC with intel core i7-6600U CPU @ 2.60GHz, 8 GBs of RAM and Python version 3.6.0. The DCE-MRI images were subsampled to half the original matrix size, as preliminary experiments demonstrated that the computational times for the GMFR method were impractical with the original reconstructed matrix size. For DCE, an arterial input function was extracted manually from the aorta on the axial slice. A processing pipeline was developed in Python that automatically performed motion correction for all 10 cases using GMFR and MDR methods.

Motion correction

MDR iterates two steps until convergence (Table.6): pixel-by-pixel fitting of the MR signal model, and frame-by-frame image co-registration. The iteration halts if the correction to the deformation field $\mathbf{d}_i(\mathbf{r}, t)$ after iteration i at location $\boldsymbol{r}$ and time t, is small:

$$\text{median}_{\mathbf{r}} \max_t \|\mathbf{d}_i(\mathbf{r}, t) - \mathbf{d}_{i-1}(\mathbf{r}, t)\|_2 < 1 \text{ pixel size} \tag{5.1}$$

Pixel-by-pixel model fitting was performed with a mono-exponential recovery for T1[32], a diffusion tensor model for DTI[37] and a linear 2-compartment filtration model fit for DCE-MRI[40]. The calculations for individual pixels are independent and were distributed among the available CPU-cores to reduce computational times.

Frame-by-frame co-registration was implemented in elastix[4] using the same parameters for all individual datasets and all three contrast mechanisms: a 2D free-form deformation (FFD) model with 3rd order B-splines, 4 resolution levels, linear interpolation for the calculation of the displacement vectors between pixel positions and a uniform grid of control points with spacing set to 16 mm for the finest resolution. The similarity metric was the sum of squared differences and adaptive stochastic gradient descent[64] was used for the optimization process. Mean squared error is a suitable metric here because the target images follow the contrast and intensity of the acquired images. Moreover, since the model fitting step also uses a least squares metric, this guarantees convergence of the algorithm.

GMFR was implemented with an existing elastix implementation[111]. In order to ensure a fair comparison, the registration parameters were the same as those of MDR except for the use of a stack FFD transform modeled by 3rd order B-splines and the use of the D_{PCA} similarity metric[77].

Input:	Acquired (x,t): measured signals at pixel locations x and time frames t.
Output:	Registered(x,t): motion corrected signals
Algorithm:	Registered = Acquired until convergence do for all x: Fitted(x,:) = model-fit (Registered(x,:)) for all t: *Registered(:,t) = co-register(Acquired(:,t), Fitted(:,t))*

Table 6: Pseudocode describing MDR algorithm

Evaluation of registration quality

Four different scores were derived to measure the quality of the motion correction (Eqs.5.2 - 5.4). All scores were first calculated for each pixel x inside an ROI, then the mean and the median over the ROI were reported. The ROI was a rectangular region of fixed size and position for all patients, capturing both kidneys as well as part of the surrounding abdominal area (i.e. liver, spleen).

$$CS(x) = \frac{\sum_t [Registered(x,t) - Fitted(x,t)]^2}{\sum_t Fitted(x,t)^2} \tag{5.2}$$

$$CV(x) = \frac{\text{standard\_deviation}(Registered(x,:))}{\text{average}(Registered(x,:))} \tag{5.3}$$

$$IQR(x) = 75\text{th\_percentile}\big(Registered(x,:)\big) - 25\text{th\_percentile}(Registered(x,:)) \tag{5.4}$$

$$STD(x) = \text{standard\_deviation}(\text{second\_difference}(Registered(x,:)) \tag{5.5}$$

All scores are defined such that smaller values indicate better motion correction. The chi-square error (CS, Eq.5.2[112]) measures whether a set of observed values is significantly different from the values expected based on the signal model. Since the signal models do not allow for motion, the assumption is that removing motion will improve the model fit. The coefficient of variation of the signal over time (CV, Eq.5.3[113]), the interquartile range (IQR, Eq.5.4[114]) and the standard deviation of the second derivative (STD, Eq.5.5[115]) are all measures of smoothness that increase when noise or other types of oscillations are added to the signal. The assumption here is that proper motion correction removes motion-induced oscillations and therefore reduces the aforementioned scores.

Statistical analysis:

A non-parametric Wilcoxon signed rank test was used to compare whether a given score was on average significantly different between group-wise and MDR results. Statistical significance was defined as $p<0.05$ and a Bonferroni correction was applied to account for the use of multiple scores. Since 8 different scores are used (median and mean for each of 4 scores) this leads to a cut-off value of $p<0.05/8 = 0.00625$ for each individual comparison.

In order to determine whether the effect of registration method depends on the choice of modality, the relative difference between GMFR and MDR was calculated for each of the 8 scores and in each individual dataset:

$$Diff\ (score) = \frac{score(MDR) - score(groupwise)}{(score(MDR) + score(groupwise))/2} \tag{5.6}$$

With this definition, a negative difference means that MDR performs better motion correction. A pairwise non-parametric Wilcoxon test was then used to compare these differences between T1, DTI and DCE, using the same significance level ($p<0.05$) and Bonferroni correction to test for the differences in each pair.

All evaluation scores were also calculated for the uncorrected, acquired MRI data to confirm that both methods provide effective motion correction.

5.4 Results

Table.7 compares the average values of all 8 scores between both methods, showing a significant difference in 10 out of 24 cases. MDR scored better in 9 of these 10 cases including 1 T1 score, 3 DTI scores, and 5 DCE scores. GMFR performed better in 1 of the T1 scores. Comparing the averages over the population, the differences in scores between MDR and GMFR are relatively small for T1 (ranging from -9.5% to 1.6% with mean -1.8%) and DTI (from -0.74% to 0.64% with mean -1.57%) but higher for DCE (ranging from -18%, -3.0% with mean -9.87%).

Figure 20 shows the distribution of the relative differences for each score and every modality (T1, DTI, DCE) and the results of the pairwise comparisons between modalities. The figure confirms on an individual level that MDR generally offers an improved motion correction in single subjects (differences < 0). The largest difference observed on a single-subject level is close to 40% (for DCE in mean CS). The figure confirms that the improvement of MDR over GMFR is most substantial in DCE showing significant differences with DTI and T1 in 3 scores each. The difference between DTI and T1 was significant in 3 of the scores as well, but smaller in magnitude compared to the differences in DCE.

		T1		DTI		DCE	
		group-wise	*MDR*	*group-wise*	*MDR*	*group-wise*	*MDR*
mean	**CS (%)**	2.5 (0.8)	2.4 (0.8)	13.4 (1.3)	13.0 (1.0)	3.1 (0.6)	2.7 (0.7)
	CV (%)	28.8 (1.0)	29.1 (1.1)	38.5 (1.3)	38.2 (1.2)	17.7 (1.5)	17.2 (1.7)
	STD	25.9 (2.7)	26.2 (2.8)	75.7 (9.3)	**72.1 (8.5)***	2.67 (0.2)	**2.37 (0.1)***
	IQR	23.1 (2.3)	22.7 (2.1)	33.9 (3.4)	**32.8 (3.1)***	1.8 (0.2)	**1.67 (0.1)***
median	**CS (%)**	1.1 (0.3)	1.0 (0.3)	12.7 (0.3)	12.8 (0.2)	1.7 (0.3)	**1.4 (0.3)***
	CV (%)	26.9 (1.3)	26.9 (1.3)	35.7 (0.4)	35.9 (0.4)	15.0 (1.3)	14.5 (1.9)
	STD	**24.7 (2.4)***	25.1 (2.5)	53.6 (4.3)	53.2 (4.2)	2.46 (0.17)	**2.2 (0.13)***
	IQR	20.6 (2.0)	**20.0 (1.8)***	28.6 (2.2)	**28.1 (2.1)***	1.55 (0.13)	**1.4 (0.10)***

Table 7: Comparison of evaluation metrics between group-wise and MDR registration. For each metric, method and contrast mechanism the table shows the mean (95% confidence interval in the mean) over all 10 volunteers. In cases where the difference is significant, **bold** font is used to identify the best of the two. (* means p<0.00625).

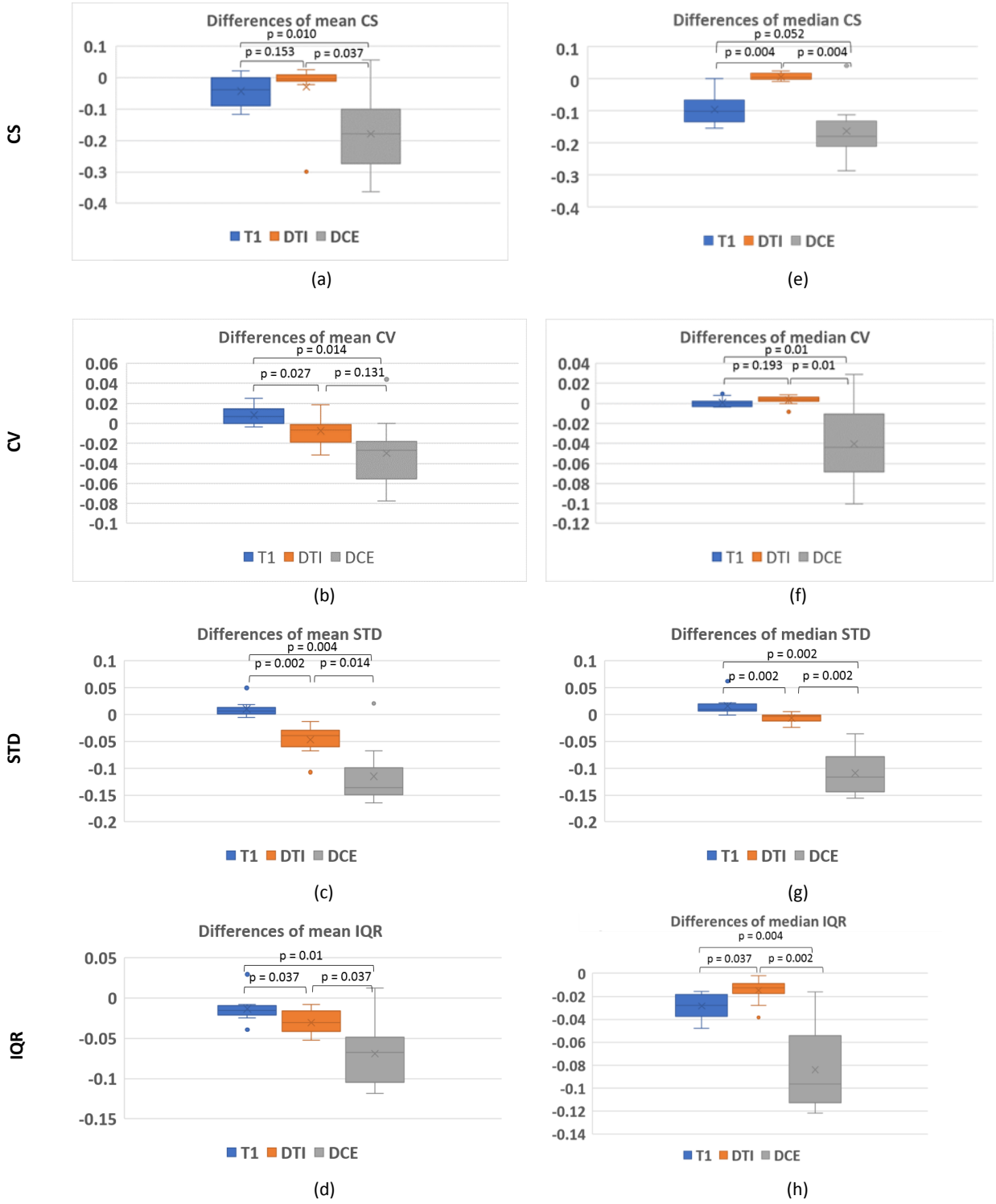

Figure 20: Differences per MRI modality (T1, DTI, DCE) for each evaluation metric

Figure 21 shows the distribution of the pixel-level scores for each individual patient and for T1, DTI and DCE cases. Scores calculated on acquired, uncorrected images are also shown for reference. The figure confirms that both GMFR and MDR methods achieved substantial improvements in all scores compared to unregistered data. The difference between both registration methods is relatively minor compared to the difference with the uncorrected data, but the differences are systematic between patients. The figures also confirm clearly that the choice of registration method is more important for DCE than for DTI and T1. The standard deviations of the metrics are also similar between both methods, with a tendency for slightly narrower distributions for MDR on some metrics. As for the means, both registration methods provide substantially reduced standard deviations compared to unregistered images.

Figure 22 shows the effect of motion correction using semi-quantitative parameter maps for three typical cases. These maps show the effect of motion clearly in unregistered data with free-breathing scans, evident as a blurring in the direction of motion and a duplication of organ boundaries corresponding to in-haled and exhaled states. The effect is less significant in breath hold data, as expected. The figures also indicate effective motion correction with both methods, showing sharper organ boundaries. Visually from this perspective the difference in registration quality between MDR and GMFR is difficult to identify, though there are obvious differences particularly in the thickness of the right kidney parenchyma on the DTI scans.

Figure 23 shows the effect of motion correction on quantitative maps for the same DTI and DCE cases as figure 22 with the addition of a T1 case. Motion effects do not impact quantitative maps as much as semi-quantitative maps. Nevertheless, the effect of motion correction does remain visually apparent in free-breathing data (DTI and DCE) through an improved delineation of motion-sensitive anatomic structures such as the renal cortex in the upper and lower poles of the kidney. For T1 maps acquired in breath holding, the motion artifacts and therefore the impact of co-registration are minor. Comparing MDR and GMFR, a significant difference is apparent in the FA maps in this particular case – mainly in the size and thickness of the renal parenchyma which appears larger after GMFR motion correction.

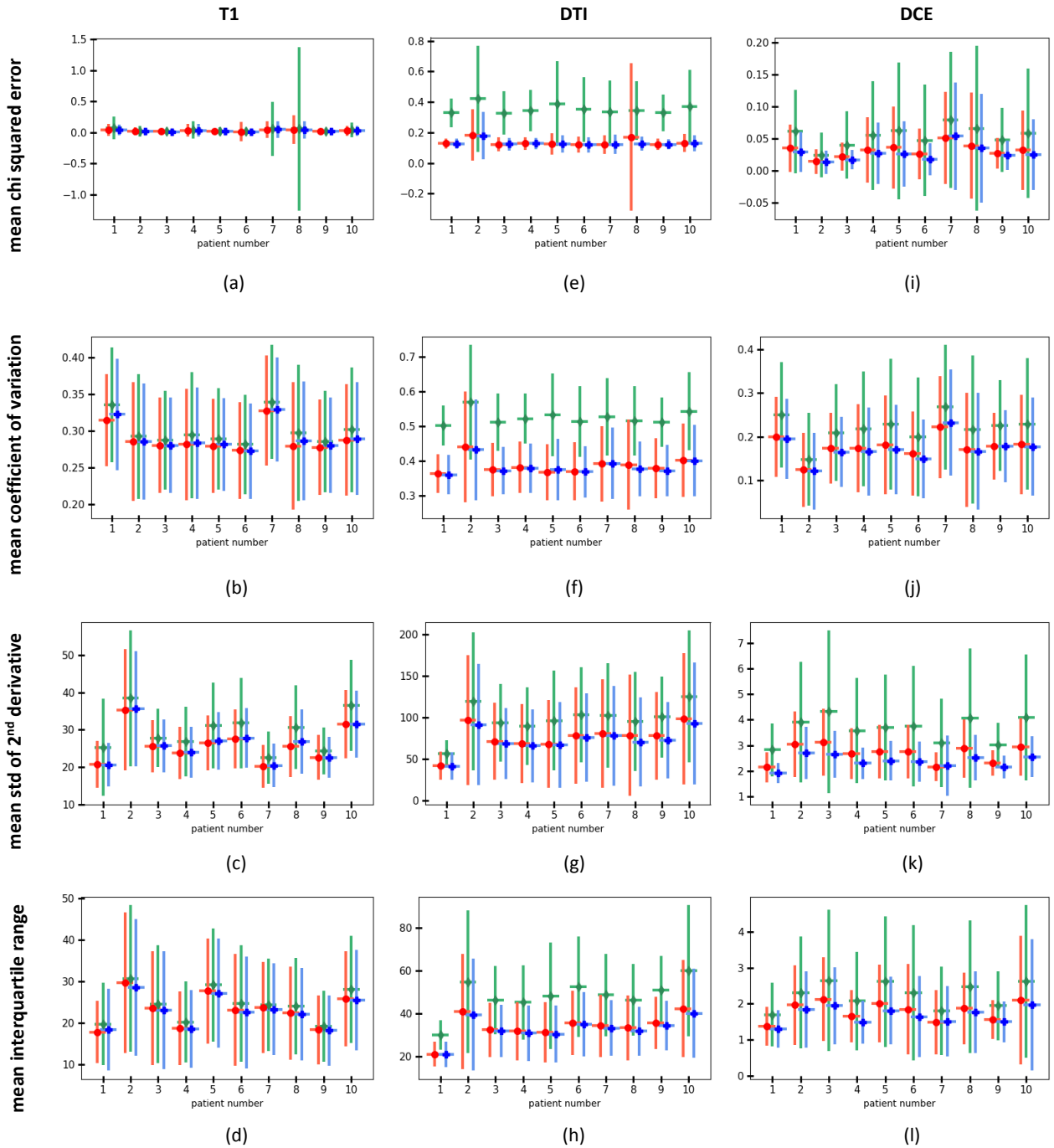

Figure 21: Plots of the mean values of the evaluation metrics per patient and registration method. The figure is consisted of 3 columns (T1, DTI, DCE) and 4 rows presenting the **mean values of each evaluation metric per patient**. The calculated metrics before registration are denoted with **green colour**, after group-wise registration with **red colour** and after MDR registration with **blue colour**. For each measurement the vertical lines indicate the standard deviation, while the horizontal lines are of fixed size and they are included to facilitate the visual comparison between methods.

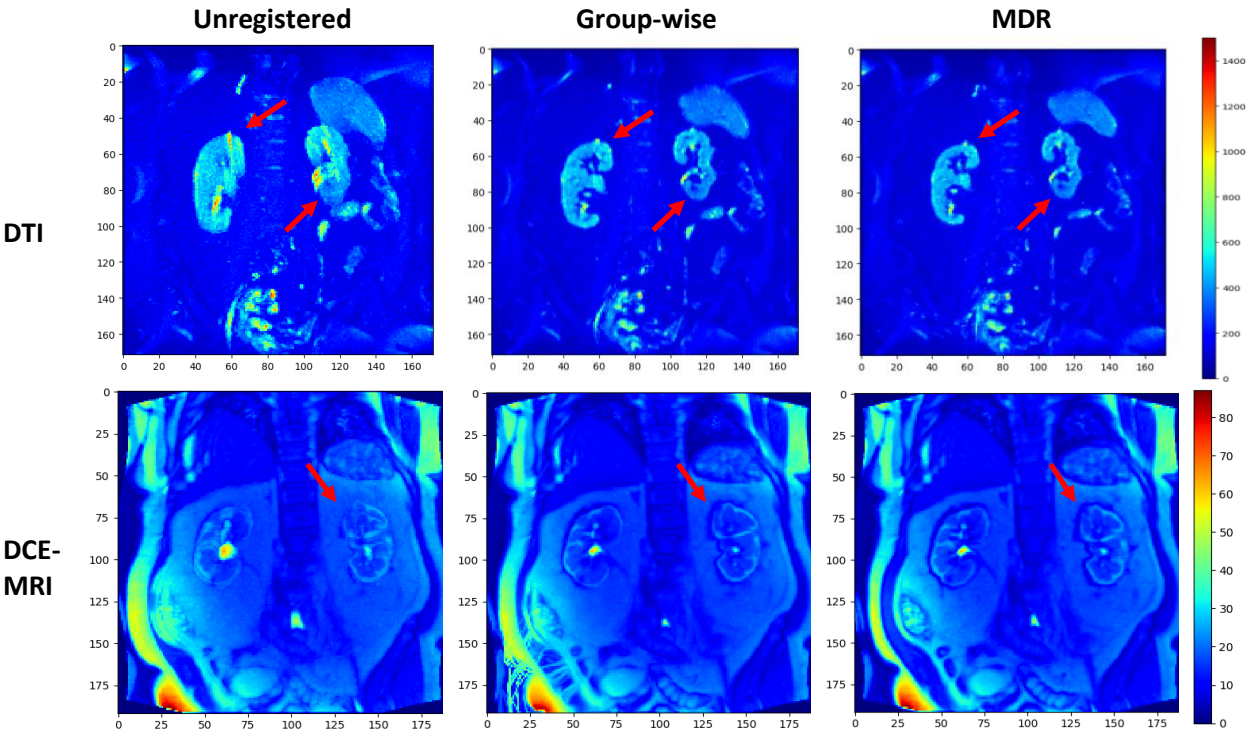

Figure 22: Comparison of maximum intensity maps (semi-quantitative parametric maps) for DTI and DCE. The figure illustrates the maximum intensity maps from a single patient DTI (**first row**) and DCE-MRI data (**second row**). Each column displays the maps before registration (unregistered) after group-wise and after MDR motion correction respectively.

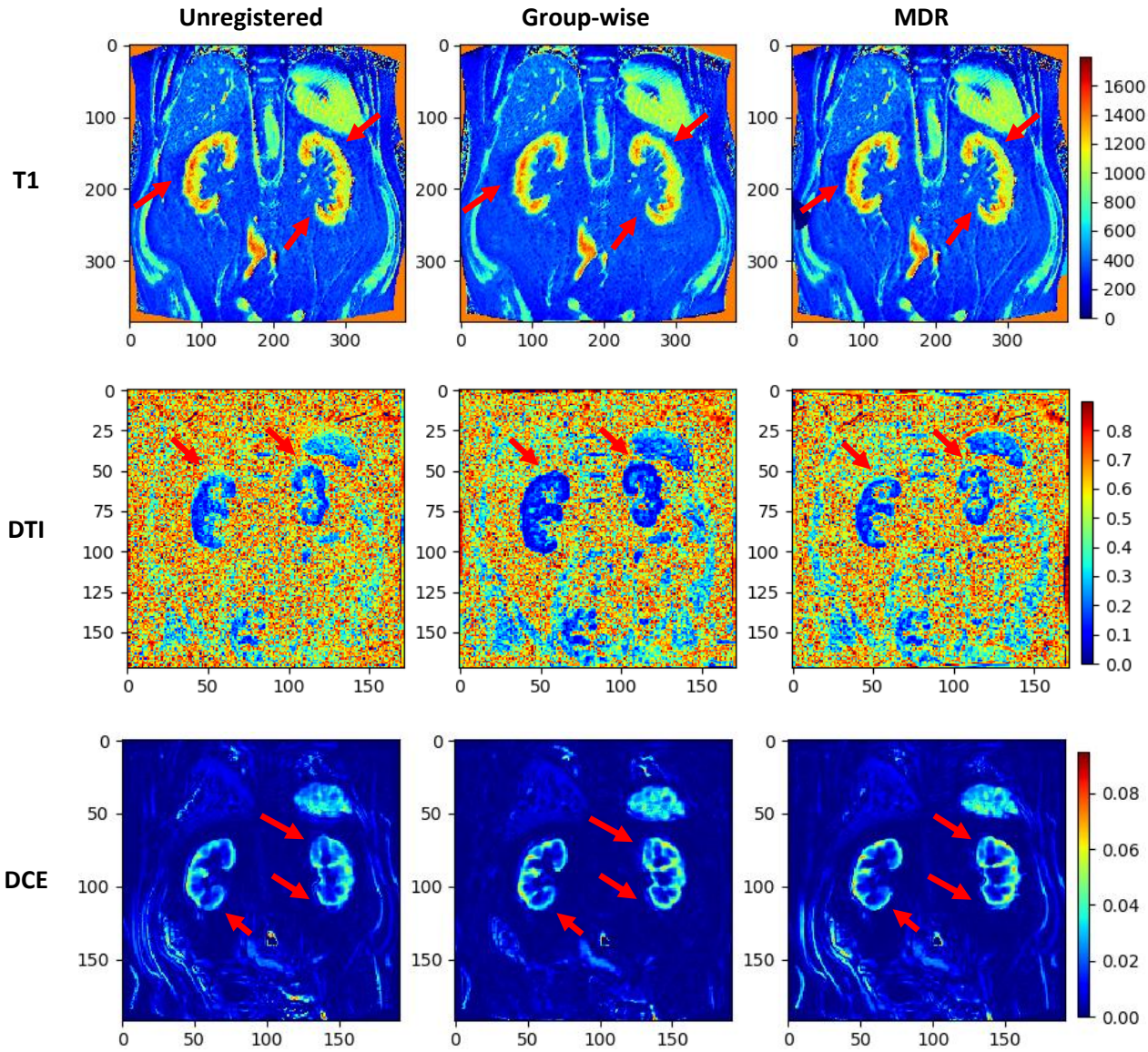

Figure 23: Comparison of parametric: T1, FA and RBF maps extracted from T1, DTI and DCE-MRI respectively for Unregistered, Group-wise and MDR methods. The **first row** contains the T1 maps, the **second row** the FA and the **third row** the RBF maps. Each row is divided in **three columns** displaying the maps before registration (**unregistered**) after **group-wise** and after **MDR** motion correction respectively.

Figure 24 compares the execution times of the GMFR and MDR methods for every patient across the examined modalities. MDR is, on the whole, faster with massive improvements in calculation times in the computationally heavy MRI application areas. For T1-mapping, MDR is on average 1.5 min slower per patient than GMFR, since a non-linear model-fitting which is quite computationally expensive is performed. This affects more MDR than GMFR time-wise, since the former performs the model-fitting process multiple times to achieve registration. For DTI and DCE, MDR is on average 5 and 10 times faster and saves 230 min and 956 min per patient, respectively. These measurements are in accordance with the fact that since GMFR involves a matrix inversion process which depends on the dataset's size it requires more time as the number of timepoints grows from 28 for T1, to 146 for DTI and finally 265 for DCE. The differences are consistent between subjects.

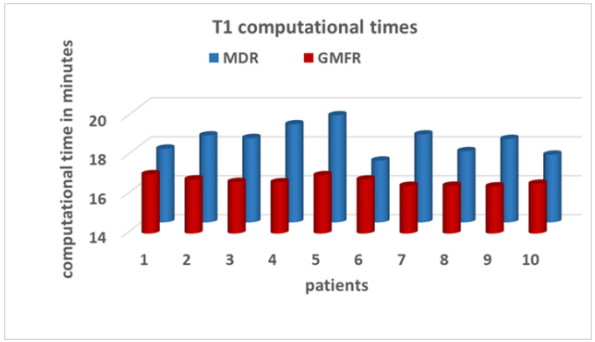

	mean +/- std	Wilcoxon p-value
MDR	18.2 +/- 0.7	0.002**
GMFR	16.7 +/- 0.2	

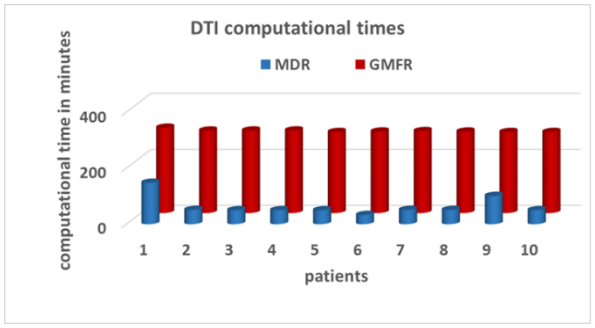

	mean +/- std	Wilcoxon p-value
MDR	63.5 +/- 32.6	0.002**
GMFR	292.9 +/- 4.4	

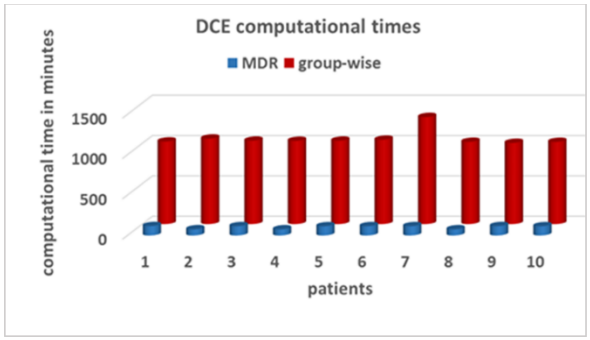

	mean +/- std	Wilcoxon p-value
MDR	103 +/- 17.8	0.002**
GMFR	1058.8 +/- 89.9	

Figure 24: Comparison of computational times in minutes per patient (1-10) for group-wise (red-colour) and MDR (blue-colour) methods on T1, DTI and DCE data. The two columns in every matrix present the mean +/- standard deviation (std) per method and the p-value of the Wilcoxon signed ranked test (a=0.05), the ****** denote statistical significance.

5.5 Discussion

The aim of this study was to compare MDR against a state-of-the-art group-wise model-free method in a challenging application of multi-parametric renal MRI. The results confirm the hypothesis that MDR is a more beneficial approach in the context of quantitative imaging: MDR scores better on the majority of the evaluation metrics and offers a substantial gain in computational times. The improvement of MDR is more substantial in the challenging application areas – in this case DTI and DCE, which were performed in free breathing and included a larger number of acquired frames per slice.

These results are in line with previous observations in Flouri et al[86], which showed that MDR improved motion correction compared to a PCA-based MFR method in diffusion-weighted imaging of the placenta. The current study substantially strengthens the evidence for the better performance of MDR. First, a more recent model-free method that followed a group-wise approach (GMFR) was selected as comparator, since it has been shown to perform well in a wide range of application areas including multi-parametric MRI[77, 110]. Second, the comparison was performed in a range of contrast mechanisms (T1, DTI, DCE) including methods such as T1 and DCE that exhibit much stronger reversals compared to DWI/DTI. Third, renal MRI in free-breathing is associated with larger motion amplitudes, typically over 20 mm in the y-direction – significantly larger than the thickness of the anatomical structures of interest (renal cortex) and approximately 8 times larger than the maximum amplitude of 2.5 mm considered in the placenta[86]. Fourth, in this study the registration quality was assessed with 4 different scores, including CS but also model-free smoothness scores CV, STD and IQR. While each score has its own limitations, the combined results of all 4 scores pointing in the same direction substantially strengthens the evidence. In particular, the use of CS as the sole evaluation metric could create an unfair bias towards MDR because the CS metric is used within MDR as part of the model fitting step and, in this study, in the image registration as well.

A well-known possible limitation of MDR is the risk that a model-bias will negatively affect the motion correction. The effect has been observed, for instance in renal DCE, where motion correction typically fails in a small number of frames around the bolus arrival when a model is used that does not properly account for bolus delay[39]. However, in quantitative MRI this problem is not resolved by the use of MFR because model errors will impact the final parameters even if the model is not used for the specific purpose of motion correction. Nevertheless, we chose in this study to use a number of model-free evaluation scores (CV, STD and IQR) which aim to reveal possible model bias in MDR. All four scores essentially led to the

same conclusion and showed the same systematic behavior. One exception may be the DCE data for participant 7, where the average scores for MDR are slightly higher than for GMFR – in contrast to what is observed in all other participants. Visual inspection of the images showed an artifact peripheral to the field of view which resulted in large distortions with MDR in a subset of frames and therefore slightly higher scores for some of the metrics for MDR. The artefact visually affected the MDR motion corrected dynamics to a larger extent than GMFR, but the difference was not apparent in the parametric maps.

On the other hand, model bias may well remain an issue for MDR in other applications where the model provides a poor fit to the data in other organs inside the field of view. An example where this may occur is in cardiac DCE-MRI where the kinetic models tend to offer a close fit to the myocardial data, but generally perform poorly in many of the surrounding areas including the right ventricle, pulmonary arteries, lungs and aorta. Unless the model can be generalized to apply everywhere in the field of view, such applications may benefit from a model-free motion-correction followed by model fitting on a myocardial ROI only. Conversely, the assumptions that are made in MFR, though fairly generic in nature, are not automatically fulfilled in all conditions and may adversely impact on the results. Typical examples include the assumption that motion does not affect the principal components of an acquired MRI signal and the assumption that robust-PCA can isolate rapid local intensity changes in the low rank component of the acquired signal. However, while the first assumption may be true for more erratic motion (such as that encountered between breath hold positions) it may not be true in the case of free breathing data where motion can induce smooth periodic signal oscillations[73], likewise the second assumption does not hold for cases where rapid motion elements occur locally over a short period of time[74]. This study includes two free-breathing MR modalities (DTI and DCE) and shows that the GMFR method generally provides good motion correction in free breathing as well. Nevertheless, the observation that the difference between MDR and GMFR is significant only in the free-breathing acquisitions is consistent with the expected impact of this effect.

A striking observation in this study is the major reduction in calculation times with the use of MDR as compared to GMFR - reducing calculation times on a standard laptop PC with up to 16 hours per slice for DCE. Moreover, DCE data were down sampled by a factor of 2 for this study after initial experiments demonstrated that GMFR for DCE at full resolution was not practically feasible with this setup. GMFR carries a significant penalty due to the group-wise approach to image registration that generates a large search space for the inverse problem. While, MDR is implemented in this study with a standard sequential

pairwise image registration, which splits up the large computational problem into a series of independent smaller problems that can be addressed more efficiently. In principle, MDR can be implemented in a group-wise fashion as well and in certain problems this may carry a trade-off in terms of co-registration accuracy or robustness. This was not done in the current study because MDR performed well in the current pairwise implementation. Nevertheless, we chose to prioritize registration accuracy over computational time in the selection of a comparator because calculation times can be reduced with other means (further parallelization, CPU implementations, or more powerful hardware) if there is a proven benefit in terms of accuracy and robustness. As the results show, the massive computational costs that comes with group-wise registration do not seem to necessarily translate into an improved motion correction, which reduces the interest in a separate comparison between pairwise MDR and pairwise MFR.

There are further possible improvements in MDR that were not explored fully in this study. Group-wise MDR or a fully joint optimization of MRI model parameters and deformation fields[89] was not evaluated in this study. More conventional optimization through fine tuning of elastix parameters and parallelization of the pairwise registrations have not been explored in depth but could lead to significant further gain in computational times. Clearly, over the last few years the use of deep learning methods has appeared as perhaps the most promising approach to achieve a step change in image co-registration speed[93, 97, 100, 116]. Previous studies have shown that this can achieve comparable results as traditional registration methods but at a fraction of the time. The most straightforward approach to bring deep learning into MDR would be to replace the pairwise co-registrations with a neural network approach. However, more integrated approaches could also be considered, aiming for a joint recovery of deformation fields and MRI parameters. Furthermore, an interesting objective could be to incorporate the model-driven philosophy in the training process itself to improve model's interpretability (which remains a soft-spot for deep learning applications in the medical field).

As regards to the general question of MDR versus MFR for quantitative MRI, the current study is obviously limited as it provides evidence in renal application areas only. However, motion correction of the chosen methods (T1, DTI, DCE) in the kidney is among the most challenging problems in quantitative MRI, for various reasons: (i) the field of view is large and includes multiple other organs which can create issues when working with kidney-specific models; (ii) due to the major differences between cortex and medullary structure, methods such as DCE and T1 are associated with major reversals in image contrast; (iii) motion

has large amplitudes compared to the size of the organ and is essentially non-rigid. This does offer some confidence that the results will translate to other application areas of quantitative MRI. One of the most important open research topics in the field of medical image registration is the search for proper metrics to evaluate the registration results. Given the lack of a golden standard there is still room for improvement regarding the registration evaluation process, for example the metrics used in this study are symmetric and could potentially be affected by systematic biases in the model fitting process on a pixel-basis. In the current implementation such cases could be partially assessed by examining the standard deviations of the respective metrics reported on a patient basis in Fig21. As part of future work additional registration evaluation metrics could be considered to improve the assessment of possible biases in the model-fitting process on a pixel-basis (i.e.mean bias error). Another limitation of the study is the absence of a ground truth. Though partially compensated by the use of multiple metrics, there is a clear benefit in a more in-depth simulation study in anthropomorphic phantoms with realistic motion and contrast changes.

Finally, the ultimate criteria for judging the impact of a motion correction method or any other methodological improvement lies in the effect on clinical endpoints. The presented study compared a model-driven registration method against a state-of-the-art model-free method as part of a renal MR imaging biomarkers quantification pipeline and assessed the results based on metrics that quantified the model-fitting error and the smoothness of the pixel intensity curves after registration. However, the most important test would be to compare the two registration methods in clinical endpoints where both registration methods could be applied on the same data. In clinical trials the small differences in the MR imaging biomarkers obtained after each registration method could be assessed by medical doctors (i.e. nephrologists, diabetologists) after being applied on a few hundred cases, an example of such a study is iBEAt. At this point it is expected that the most effective motion correction method will produce more accurate measurements of the MR imaging biomarkers which in turn will allow earlier prognosis (i.e. will facilitate a more accurate classification of the examined subjects as either healthy or early diabetics) or more accurate diagnosis disease staging etc. In other words, the motion correction method that will facilitate more the clinical examination and intervention can be the method of choice. It may well be that the differences between methods as observed in the current study are too small to be of any significance when put in the context of disease progression or therapy response. However, even in that case the combined effect of improvements in accuracy and computational times remain a strong argument to support the conclusion that MDR is a preferred approach for motion correction in quantitative MRI.

5.6 Conclusion

Based on the calculated evaluation metrics for the examined cohort the use of a pair-wise model-driven registration (MDR) is more beneficial than a state-of-the-art group-wise model-free registration (GMFR) method[77] for motion correction of quantitative MRI in the kidney. Improvements in registration accuracy are moderate but consistent across subjects and improvements in calculation time are major in the more challenging methods of DCE and DTI.

Chapter 6

Summary and outlook

6.1 Overall conclusions and future work

Renal blood flow (RBF), fractional anisotropy (FA) and MR relaxometry are only a few indicative cases of a larger set of renal MR imaging biomarkers that will be examined in the BEAt-DKD[2] project, to test whether they can be used to improve prognosis, diagnosis and monitoring for DKD patients. A common requirement for a precise measurement of all the aforementioned biomarkers is to perform a pixel-wise model-fitting on the acquired MRI data, assuming that the data exhibit spatial correspondence[77]. However, due to patient breathing, unwilling motion and organs distortions motion artifacts corrupt the data, increasing the model-fitting error. Hence, in order to extract MR imaging biomarkers more accurately, image registration techniques are needed to properly align the acquired data before proceeding to the model-fitting process.

Two major categories of medical image registration techniques were examined in this study: the model-driven that incorporates information from physiological models (describing the data) in the registration process and the model-free that rely on a variety of data-driven assumptions (not related to physiological models). In the context of quantitative MRI, image registration is a processing step in an imaging biomarkers quantification pipeline, which will ultimately always require a physiological model to be fitted on the data in order to estimate the wanted parameters. This raises the question of whether model-free registration methods could introduce additional biases on top of the inevitable model-bias, making it the less effective choice. To address this question a representative method was chosen from both categories and the two methods were compared on renal T1, DTI and DCE-MRI data from 10 DKD patients, registering only the middle slice for each acquisition. A state-of-the-art model-free registration method for quantitative MRI[77] was already available, while the model-driven registration methods found were limited to individual modalities. Hence, for this thesis a robust and versatile model-driven registration (MDR) solution was implemented in Python with the use of elastix[4]. This implementation utilized a single set of registration parameters to compensate for motion artifacts regardless of the MR modality at hand. For the examined dataset the two methods had statistically significant differences for 10 out of 24 cases and MDR scored better in 9 of them (1 score for T1, 3 scores for DTI and 5 scores for DCE). Hence, the conducted experiments indicated that use of MDR is more beneficial according to the majority of the registration evaluation measures, while requiring for the whole cohort ~14% of the respective model-free method's computational time. The aforementioned findings are in accordance to those of another study that compared a model-driven versus a model-free motion correction method exclusively on DWI-MRI[86]. The satisfying results of MDR on a range of different MR modalities for the motion correction of renal

MRI, which is known to be a very challenging application, indicate that it is possible for the method to generalize well to the registration of MR images from other parts of the body as well.

The main contribution of the work presented is that it systematically assessed the registration results of an MDR against a state of the art MFR method in the context of quantitative renal MRI, with the registration evaluation metrics indicating that MDR performed better. Furthermore, this study showed that a single set of registration parameters can be utilized across different MRI modalities, combined with the respective pathophysiological models making MDR a suitable solution for universal motion correction of renal MRI data. Finally, the conducted experiments showed that MDR is much faster than the respective MFR alternative, especially for MR acquisitions with large number of timepoints (i.e. DTI, DCE).

A well-known limitation for MDR is the model-bias that may have a negative effect in the registration process. However, the conducted experiments indicated that in the context of quantitative MRI this is not a major concern since the model is always integrated in the quantification process itself, introducing model errors even for the cases where the model is not included in the registration process. A soft-spot revealed for MDR during the experimental process is that it can be relatively more sensitive to the presence of non-motion related artifacts, if the corrupted frames are not removed by the quality assurance control. It is speculated that the model-free group-wise registration method may perform better on data with such acquisition artifacts because it combines information from all available timepoints, possibly forming a more “favorable” optimization landscape. Accordingly, a future version of MDR could perform simultaneous joint optimization of the registration and the model-fitting process, ending up solving a highly overdetermined problem with an optimization landscape that could further improve MDR’s robustness. Another interesting direction for future work could be to integrate the model-fitting process in a deep learning scheme for motion correction. By incorporating the physiological model in the training process of the network it is possible to achieve better results, while increasing the model’s interpretably, one of the weakest aspects of modern deep learning solutions in the medical imaging field.

References

[1] SELBY, N. M., BLANKESTIJN, P. J., BOOR, P., COMBE, C., ECKARDT, K.-U., EIKEFJORD, E., GARCIA-FERNANDEZ, N., GOLAY, X., GORDON, I., GRENIER, N., HOCKINGS, P. D., JENSEN, J. D., JOLES, J. A., KALRA, P. A., KRÄMER, B. K., MARK, P. B., MENDICHOVSZKY, I. A., NIKOLIC, O., ODUDU, A., ONG, A. C. M., ORTIZ, A., PRUIJM, M., REMUZZI, G., RØRVIK, J., DE SEIGNEUX, S., SIMMS, R. J., SLATINSKA, J., SUMMERS, P., TAAL, M. W., THOENY, H. C., VALLÉE, J.-P., WOLF, M., CAROLI, A. & SOURBRON, S. 2018. Magnetic resonance imaging biomarkers for chronic kidney disease: a position paper from the European Cooperation in Science and Technology Action PARENCHIMA. *Nephrology, dialysis, transplantation : official publication of the European Dialysis and Transplant Association - European Renal Association,* 33**,** ii4-ii14.

[2] 2018. *BEAt DKD* [Online]. Available: https://www.beat-dkd.eu/ [Accessed 20/11/2018 2018].

[3] GOODING, K. M., LIENCZEWSKI, C., PAPALE, M., KOIVUVIITA, N., MAZIARZ, M., ANDERSSON, A.-M. D., SHARMA, K., PONTRELLI, P., HERNANDEZ, A. G. & BAILEY, J. J. M. 2020. Prognostic Imaging Biomarkers for Diabetic Kidney Disease (iBEAt): Study protocol.

[4] KLEIN, S., STARING, M., MURPHY, K., VIERGEVER, M. A. & PLUIM, J. P. 2010. Elastix: a toolbox for intensity-based medical image registration. *IEEE transactions on medical imaging,* 29**,** 196-205.

[5] PALLABI, P. 2018. Some Information about the Morphology and Anatomy of the Human

Kidney. *Journal of Morphology and Anatomy,* 2.

[6] EMAMIAN, S., NIELSEN, M., PEDERSEN, J. & YTTE, L. 1993. Sonographic evaluation of renal appearance in 665 adult volunteers: correlation with age and obesity. *Acta Radiologica,* 34**,** 482-485.

[7] SHAHBAZIAN, H. & REZAII, I. 2013. Diabetic kidney disease; review of the current knowledge. *J Renal Inj Prev,* 2**,** 73-80.

[8] ALICIC, R. Z., ROONEY, M. T. & TUTTLE, K. R. 2017. Diabetic Kidney Disease: Challenges, Progress, and Possibilities. *Clin J Am Soc Nephrol,* 12**,** 2032-2045.

[9] RUGGENENTI, P. & REMUZZI, G. J. N. D. T. 2000. Nephropathy of type 1 and type 2 diabetes: diverse pathophysiology, same treatment? 15**,** 1900-1902.

[10] HU, J., YANG, S., ZHANG, A., YANG, P., CAO, X., LI, X., GOSWAMI, R., WANG, Y., LUO, T., LIAO, K., CHENG, Q., XIAO, X. & LI, Q. 2016. Abdominal Obesity Is More Closely Associated With Diabetic Kidney Disease Than General Obesity. *Diabetes Care,* 39**,** e179-80.

[11] MANCINI, M., MASULLI, M., LIUZZI, R., MAINENTI, P. P., RAGUCCI, M., MAUREA, S., RICCARDI, G. & VACCARO, O. 2013. Renal duplex sonographic evaluation of type 2 diabetic patients. *J Ultrasound Med,* 32**,** 1033-40.

[12] ZERBINI, G., BONFANTI, R., MESCHI, F., BOGNETTI, E., PAESANO, P. L., GIANOLLI, L., QUERQUES, M., MAESTRONI, A., CALORI, G., DEL MASCHIO, A., FAZIO, F., LUZI, L. & CHIUMELLO, G. 2006. Persistent renal hypertrophy and faster decline of glomerular filtration rate precede the development of microalbuminuria in type 1 diabetes. *Diabetes,* 55**,** 2620-5.

[13] RIGALLEAU, V., GARCIA, M., LASSEUR, C., LAURENT, F., MONTAUDON, M., RAFFAITIN, C., BARTHE, N., BEAUVIEUX, M.-C., VENDRELY, B., CHAUVEAU, P., COMBE, C. & GIN, H. 2010. Large kidneys predict poor renal outcome in subjects with diabetes and chronic kidney disease. *BMC Nephrology,* 11**,** 3.

[14] WOLF, M., DE BOER, A., SHARMA, K., BOOR, P., LEINER, T., SUNDER-PLASSMANN, G., MOSER, E., CAROLI, A. & JEROME, N. P. 2018. Magnetic resonance imaging T1- and T2-mapping to assess renal structure and function: a systematic review and statement paper. *Nephrol Dial Transplant,* 33**,** ii41-ii50.

[15] TAKAHASHI, T., WANG, F. & QUARLES, C. C. 2015. Current MRI techniques for the assessment of renal disease. *Curr Opin Nephrol Hypertens,* 24**,** 217-23.

[16] PRUIJM, M., MENDICHOVSZKY, I. A., LISS, P., VAN DER NIEPEN, P., TEXTOR, S. C., LERMAN, L. O., KREDIET, C. T. P., CAROLI, A., BURNIER, M. & PRASAD, P. V. 2018. Renal blood oxygenation level-dependent magnetic resonance imaging to measure renal tissue oxygenation: a statement paper and systematic review. *Nephrol Dial Transplant,* 33**,** ii22-ii28.

[17] PRUIJM, M., MILANI, B. & BURNIER, M. 2016. Blood Oxygenation Level-Dependent MRI to Assess Renal Oxygenation in Renal Diseases: Progresses and Challenges. *Front Physiol,* 7**,** 667.

[18] NOTOHAMIPRODJO, M., REISER, M. F. & SOURBRON, S. P. 2010. Diffusion and perfusion of the kidney. *Eur J Radiol,* 76**,** 337-47.

[19] CAROLI, A., SCHNEIDER, M., FRIEDLI, I., LJIMANI, A., DE SEIGNEUX, S., BOOR, P., GULLAPUDI, L., KAZMI, I., MENDICHOVSZKY, I. A., NOTOHAMIPRODJO, M., SELBY, N. M., THOENY, H. C., GRENIER, N. & VALLEE, J. P. 2018. Diffusion-weighted magnetic resonance imaging to assess diffuse renal pathology: a systematic review and statement paper. *Nephrol Dial Transplant,* 33**,** ii29-ii40.

[20] LU, L., SEDOR, J. R., GULANI, V., SCHELLING, J. R., O'BRIEN, A., FLASK, C. A. & MACRAE DELL, K. 2011. Use of diffusion tensor MRI to identify early changes in diabetic nephropathy. *Am J Nephrol,* 34**,** 476-82.

[21] INOUE, T., KOZAWA, E., OKADA, H., INUKAI, K., WATANABE, S., KIKUTA, T., WATANABE, Y., TAKENAKA, T., KATAYAMA, S., TANAKA, J. & SUZUKI, H. 2011. Noninvasive evaluation of kidney hypoxia and fibrosis using magnetic resonance imaging. *J Am Soc Nephrol,* 22**,** 1429-34.

[22] ZHAO, J., WANG, Z. J., LIU, M., ZHU, J., ZHANG, X., ZHANG, T., LI, S. & LI, Y. 2014. Assessment of renal fibrosis in chronic kidney disease using diffusion-weighted MRI. *Clin Radiol,* 69**,** 1117-22.

[23] FENG, Q., MA, Z., WU, J. & FANG, W. 2015. DTI for the assessment of disease stage in patients with glomerulonephritis--correlation with renal histology. *Eur Radiol,* 25**,** 92-8.

[24] TOGAO, O., DOI, S., KURO-O, M., MASAKI, T., YORIOKA, N. & TAKAHASHI, M. 2010. Assessment of renal fibrosis with diffusion-weighted MR imaging: study with murine model of unilateral ureteral obstruction. *Radiology,* 255**,** 772-780.

[25] DAMBREVILLE, S., CHAPMAN, A. B., TORRES, V. E., KING, B. F., WALLIN, A. K., FRAKES, D. H., YOGANATHAN, A. P., WIJAYAWARDANA, S. R., EASLEY, K., BAE, K. T., BRUMMER, M. E. & CONSORTIUM FOR RADIOLOGIC IMAGING STUDIES OF POLYCYSTIC KIDNEY, D. 2010. Renal arterial blood flow measurement by breath-held MRI: Accuracy in phantom scans and reproducibility in healthy subjects. *Magn Reson Med,* 63**,** 940-50.

[26] JIANG, K., FERGUSON, C. M., WOOLLARD, J. R., ZHU, X. & LERMAN, L. O. 2017. Magnetization Transfer Magnetic Resonance Imaging Noninvasively Detects Renal Fibrosis in Swine Atherosclerotic Renal Artery Stenosis at 3.0 T. *Invest Radiol,* 52**,** 686-692.

[27] ITO, K., HAYASHIDA, M., IZUMITANI, S., FUJIMINE, T., ONISHI, T. & GENBA, K. 2013. Magnetisation transfer MR imaging of the kidney: evaluation at 3.0 T in association with renal function. *Eur Radiol,* 23**,** 2315-9.

[28] LI, L. P., TAN, H., THACKER, J. M., LI, W., ZHOU, Y., KOHN, O., SPRAGUE, S. M. & PRASAD, P. V. 2017. Evaluation of Renal Blood Flow in Chronic Kidney Disease Using Arterial Spin Labeling Perfusion Magnetic Resonance Imaging. *Kidney Int Rep,* 2**,** 36-43.

[29] JUNG, B. A. & WEIGEL, M. 2013. Spin echo magnetic resonance imaging. *J Magn Reson Imaging,* 37**,** 805-17.

[30] MARKL, M. & LEUPOLD, J. 2012. Gradient echo imaging. *J Magn Reson Imaging,* 35**,** 1274-89.

[31] LOOK, D. C. & LOCKER, D. R. 1970. Time Saving in Measurement of NMR and EPR Relaxation Times. *Review of Scientific Instruments,* 41**,** 250-251.

[32] MESSROGHLI, D. R., RADJENOVIC, A., KOZERKE, S., HIGGINS, D. M., SIVANANTHAN, M. U. & RIDGWAY, J. P. 2004. Modified Look-Locker inversion recovery (MOLLI) for high-resolution T1 mapping of the heart. *Magn Reson Med,* 52**,** 141-6.

[33] KIM, P. K., HONG, Y. J., IM, D. J., SUH, Y. J., PARK, C. H., KIM, J. Y., CHANG, S., LEE, H.-J., HUR, J. & KIM, Y. J. J. K. J. O. R. 2017. Myocardial T1 and T2 mapping: techniques and clinical applications. 18**,** 113-131.

[34] DE FIGUEIREDO, E. H., BORGONOVI, A. F. & DORING, T. M. 2011. Basic concepts of MR imaging, diffusion MR imaging, and diffusion tensor imaging. *Magn Reson Imaging Clin N Am,* 19**,** 1-22.

[35] RAJAGOPALAN, V., JIANG, Z., YUE, G. H., RADIC, J. S., PIORO, E. P., WYLIE, G. R. & DAS, A. 2017. A Basic Introduction to Diffusion Tensor Imaging Mathematics and Image Processing Steps. *Brain Disorders & Therapy,* 06.

[36] O'DONNELL, L. J. & WESTIN, C.-F. J. N. C. 2011. An introduction to diffusion tensor image analysis. 22**,** 185-196.

[37] KINGSLEY, P. B. 2006. Introduction to diffusion tensor imaging mathematics: Part II. Anisotropy, diffusion-weighting factors, and gradient encoding schemes. *Concepts in Magnetic Resonance Part A,* 28**,** 123-154.

[38] TSAO, J. 2010. Ultrafast imaging: principles, pitfalls, solutions, and applications. *J Magn Reson Imaging,* 32**,** 252-66.

[39] FLOURI, D. 2016. Tracer-Kinetic Model-Driven Motion Correction with Application to Renal DCE-MRI. *University of Leeds Department of Applied Mathematics & Division of Biomedical Imaging*.

[40] FLOURI, D., LESNIC, D. & SOURBRON, S. P. 2016. Fitting the two-compartment model in DCE-MRI by linear inversion. *Magnetic resonance in medicine,* 76**,** 998-1006.

[41] PURVES, W. K., SADAVA, D., ORIANS, G. H. & HELLER, H. C. 2003. *Life: the science of biology: volume III: plants and animals*, Macmillan.

[42] QIU, P. & NGUYEN, T. On image registration in magnetic resonance imaging. BioMedical Engineering and Informatics, 2008. BMEI 2008. International Conference on, 2008. IEEE, 753-757.

[43] WU, G., QI, F. & SHEN, D. 2006. Learning-based deformable registration of MR brain images. *IEEE transactions on medical imaging,* 25**,** 1145-1157.

[44] HARTLEY, R. & ZISSERMAN, A. 2003. *Multiple View Geometry in Computer Vision*, Cambridge University Press.

[45] WANG, M., LI, P. J. J. O. M. & ENGINEERING, B. 2019. A review of deformation models in medical image registration. 39**,** 1-17.

[46] SOTIRAS, A., DAVATZIKOS, C. & PARAGIOS, N. J. I. T. O. M. I. 2013. Deformable medical image registration: A survey. 32**,** 1153-1190.

[47] RUECKERT, D., SONODA, L. I., HAYES, C., HILL, D. L., LEACH, M. O. & HAWKES, D. J. 1999. Nonrigid registration using free-form deformations: application to breast MR images. *IEEE transactions on medical imaging,* 18**,** 712-721.

[48] SCHWARZ, L. A. 2007. Non-rigid Registration

Using Free-form Deformations. *Diploma Thesis, Technical University of Munich*.

[49] SONG, G., HAN, J., ZHAO, Y., WANG, Z. & DU, H. 2017. A Review on Medical Image Registration as an Optimization Problem. *Current medical imaging reviews,* 13**,** 274-283.

[50] STRAND, R., MALMBERG, F., JOHANSSON, L., LIND, L., SUNDBOM, M., AHLSTRÖM, H. & KULLBERG, J. 2017. A concept for holistic whole body MRI data analysis, Imiomics. *PloS one,* 12**,** e0169966.

[51] ADALINE, M. J., KALAISELVI, S., GOMATHI, V. & SRINIVASAGAN, K. A Registration Technique for Medical Images using Fuzzy-SIFT Matching.

[52] GU, Z., CAI, L., YIN, Y., DING, Y. & KAN, H. 2014. Registration of Brain Medical Images Based on SURF Algorithm and R-RANSAC Algorithm. *Indonesian Journal of Electrical Engineering and Computer Science,* 12**,** 2290-2297.

[53] AL-AZZAWI, N. & ABDULLAH, W. A. K. W. 2012. MRI monomodal feature-based registration based on the efficiency of multiresolution representation and mutual information. *American Journal of Biomedical Engineering,* 2**,** 98-104.

[54] POSTELNICU, G., ZOLLEI, L. & FISCHL, B. 2009. Combined volumetric and surface registration. *IEEE transactions on medical imaging,* 28**,** 508-522.

[55] ROHLFING, T., MAURER, C. R., BLUEMKE, D. A. & JACOBS, M. A. 2003. Volume-preserving nonrigid registration of MR breast images using free-form deformation with an incompressibility constraint. *IEEE transactions on medical imaging,* 22**,** 730-741.

[56] SHANMUGAPRIYA, S. & POONGUZHALI, S. 2014. AN INTENSITY-BASED MEDICAL IMAGE REGISTRATION USING GENETIC ALGORITHM. *Signal & Image Processing,* 5**,** 53.

[57] KESZEI, A. P., BERKELS, B. & DESERNO, T. M. 2017. Survey of non-rigid registration tools in medicine. *Journal of digital imaging,* 30**,** 102-116.

[58] PENNY, W. D., FRISTON, K. J., ASHBURNER, J. T., KIEBEL, S. J. & NICHOLS, T. E. 2011. *Statistical parametric mapping: the analysis of functional brain images*, Elsevier.

[59] WOODS, R. P., GRAFTON, S. T., HOLMES, C. J., CHERRY, S. R. & MAZZIOTTA, J. C. 1998. Automated image registration: I. General methods and intrasubject, intramodality validation. *Journal of computer assisted tomography,* 22**,** 139-152.

[60] YOO, T. S., ACKERMAN, M. J., LORENSEN, W. E., SCHROEDER, W., CHALANA, V., AYLWARD, S., METAXAS, D. & WHITAKER, R. 2002. Engineering and algorithm design for an image processing API: a technical report on ITK-the insight toolkit. *Studies in health technology and informatics***,** 586-592.

[61] AVANTS, B. B., TUSTISON, N. & SONG, G. 2009. Advanced normalization tools (ANTS). *Insight j,* 2**,** 1-35.

[62] KLEIN, S. 2008. *Optimisation methods for medical image registration*, Utrecht University.

[63] KLEIN, S., STARING, M. & PLUIM, J. P. 2007. Evaluation of optimization methods for nonrigid medical image registration using mutual information and B-splines. *IEEE Trans Image Process,* 16**,** 2879-90.

[64] KLEIN, S., PLUIM, J. P., STARING, M. & VIERGEVER, M. A. 2009. Adaptive stochastic gradient descent optimisation for image registration. *International journal of computer vision,* 81**,** 227.

[65] BEARE, R., LOWEKAMP, B. & YANIV, Z. J. J. O. S. S. 2018. Image segmentation, registration and characterization in R with SimpleITK. 86.

[66] MARSTAL, K., BERENDSEN, F., STARING, M. & KLEIN, S. SimpleElastix: A user-friendly, multi-lingual library for medical image registration. Proceedings of the IEEE conference on computer vision and pattern recognition workshops, 2016. 134-142.

[67] MELBOURNE, A., HIPWELL, J., MODAT, M., MERTZANIDOU, T., HUISMAN, H., OURSELIN, S. & HAWKES, D. 2011. The effect of motion correction on pharmacokinetic parameter estimation in dynamic-contrast-enhanced MRI. *Physics in Medicine & Biology,* 56**,** 7693.

[68] ZÖLLNER, F. G., SANCE, R., ROGELJ, P., LEDESMA-CARBAYO, M. J., RØRVIK, J., SANTOS, A. & LUNDERVOLD, A. 2009. Assessment of 3D DCE-MRI of the kidneys using non-rigid image registration and segmentation of voxel time courses. *Computerized Medical Imaging and Graphics,* 33**,** 171-181.

[69] YANG, X., GHAFOURIAN, P., SHARMA, P., SALMAN, K., MARTIN, D. & FEI, B. Nonrigid registration and classification of the kidneys in 3D dynamic contrast enhanced (DCE) MR images. Medical Imaging 2012: Image Processing, 2012. International Society for Optics and Photonics, 83140B.

[70] ZHANG, S., LE, T. T., KABUS, S., SU, B., HAUSENLOY, D. J., COOK, S. A., CHIN, C. W. L. & TAN, R. S. 2018. Cardiac magnetic resonance T1 and extracellular volume mapping with motion correction and co-registration based on fast elastic image registration. *MAGMA,* 31**,** 115-129.

[71] BALCI, S. K., GOLLAND, P., SHENTON, M. E. & WELLS, W. M. 2007. Free-form B-spline deformation model for groupwise registration.

[72] COLL-FONT, J., AFACAN, O., CHOW, J. S., LEE, R. S., STEMMER, A., WARFIELD, S. K. & KURUGOL, S. 2020. Bulk motion-compensated DCE-MRI for functional imaging of kidneys in newborns. *J Magn Reson Imaging,* 52**,** 207-216.

[73] MELBOURNE, A., ATKINSON, D., WHITE, M., COLLINS, D., LEACH, M. & HAWKES, D. 2007. Registration of dynamic contrast-enhanced MRI using a progressive principal component registration (PPCR). *Physics in Medicine & Biology,* 52**,** 5147.

[74] HAMY, V., DIKAIOS, N., PUNWANI, S., MELBOURNE, A., LATIFOLTOJAR, A., MAKANYANGA, J., CHOUHAN, M., HELBREN, E., MENYS, A. & TAYLOR, S. 2014. Respiratory motion correction in dynamic MRI using robust data decomposition registration–Application to DCE-MRI. *Medical image analysis,* 18**,** 301-313.

[75] FENG, Q., ZHOU, Y., LI, X., MEI, Y., LU, Z., ZHANG, Y., FENG, Y., LIU, Y., YANG, W. & CHEN, W. J. S. R. 2016. Liver DCE-MRI registration in manifold space based on robust principal component analysis. 6**,** 34461.

[76] TIRUNAGARI, S., POH, N., WELLS, K., BOBER, M., GORDEN, I. & WINDRIDGE, D. 2017. Movement correction in DCE-MRI through windowed and reconstruction dynamic mode decomposition. *Machine Vision and Applications,* 28**,** 393-407.

[77] HUIZINGA, W., POOT, D. H., GUYADER, J. M., KLAASSEN, R., COOLEN, B. F., VAN KRANENBURG, M., VAN GEUNS, R. J., UITTERDIJK, A., POLFLIET, M., VANDEMEULEBROUCKE, J., LEEMANS, A., NIESSEN, W. J. & KLEIN, S. 2016. PCA-based groupwise image registration for quantitative MRI. *Med Image Anal,* 29**,** 65-78.

[78] HAYTON, P., BRADY, M., TARASSENKO, L. & MOORE, N. J. M. I. A. 1997. Analysis of dynamic MR breast images using a model of contrast enhancement. 1**,** 207-224.

[79] ADLURU, G., DIBELLA, E. V. & SCHABEL, M. C. 2006. Model-based registration for dynamic cardiac perfusion MRI. *Journal of Magnetic Resonance Imaging: An Official Journal of the International Society for Magnetic Resonance in Medicine,* 24**,** 1062-1070.

[80] TILBORGHS, S., DRESSELAERS, T., CLAUS, P., CLAESSEN, G., BOGAERT, J., MAES, F. & SUETENS, P. J. M. I. A. 2019. Robust motion correction for cardiac T1 and ECV mapping using a T1 relaxation model approach. 52**,** 212-227.

[81] XUE, H., SHAH, S., GREISER, A., GUETTER, C., LITTMANN, A., JOLLY, M. P., ARAI, A. E., ZUEHLSDORFF, S., GUEHRING, J. & KELLMAN, P. 2012. Motion correction for myocardial T1 mapping using image registration with synthetic image estimation. *Magn Reson Med,* 67**,** 1644-55.

[82] LIKHITE, D., ADLURU, G. & DIBELLA, E. Deformable and rigid model-based image registration for quantitative cardiac perfusion. International Workshop on Statistical Atlases and Computational Models of the Heart, 2014. Springer, 41-50.

[83] VAN DE GIESSEN, M., TAO, Q., VAN DER GEEST, R. J. & LELIEVELDT, B. P. Model-based alignment of look-locker MRI sequences for calibrated myocardical scar tissue quantification. 2013 IEEE 10th International Symposium on Biomedical Imaging, 2013. IEEE, 1038-1041.

[84] BUONACCORSI, G. A., ROBERTS, C., CHEUNG, S., WATSON, Y., O'CONNOR, J. P., DAVIES, K., JACKSON, A., JAYSON, G. C. & PARKER, G. J. J. A. R. 2006. Comparison of the performance of tracer kinetic model-driven registration for dynamic contrast enhanced MRI using different models of contrast enhancement. 13**,** 1112-1123.

[85] BUONACCORSI, G. A., O'CONNOR, J. P., CAUNCE, A., ROBERTS, C., CHEUNG, S., WATSON, Y., DAVIES, K., HOPE, L., JACKSON, A. & JAYSON, G. C. 2007. Tracer kinetic model–driven registration for dynamic contrast-enhanced MRI time-series data. *Magnetic Resonance in Medicine: An Official Journal of the International Society for Magnetic Resonance in Medicine,* 58**,** 1010-1019.

[86] FLOURI, D., OWEN, D., AUGHWANE, R., MUFTI, N., MAKSYM, K., SOKOLSKA, M., KENDALL, G., BAINBRIDGE, A., ATKINSON, D., VERCAUTEREN, T., OURSELIN, S., DAVID, A. L. & MELBOURNE, A. 2020. Improved fetal blood oxygenation and placental estimated measurements of diffusion-weighted MRI using data-driven Bayesian modeling. *Magn Reson Med,* 83**,** 2160-2172.

[87] KURUGOL, S., FREIMAN, M., AFACAN, O., DOMACHEVSKY, L., PEREZ-ROSSELLO, J. M., CALLAHAN, M. J. & WARFIELD, S. K. 2017. Motion-robust parameter estimation in abdominal diffusion-weighted MRI by simultaneous image registration and model estimation. *Med Image Anal,* 39**,** 124-132.

[88] RAMOS-LLORDEN, G., ARNOLD, J., VAN STEENKISTE, G., JEURISSEN, B., VANHEVEL, F., VAN AUDEKERKE, J., VERHOYE, M. & SIJBERS, J. J. I. T. O. M. I. 2016. A unified maximum likelihood framework for simultaneous motion and $ T_ {1} $ estimation in quantitative MR $ T_ {1} $ mapping. 36**,** 433-446.

[89] BHUSHAN, M., SCHNABEL, J. A., RISSER, L., HEINRICH, M. P., BRADY, J. M. & JENKINSON, M. Motion correction and parameter estimation in dceMRI sequences: application to colorectal cancer. International Conference on Medical Image Computing and Computer-Assisted Intervention, 2011. Springer, 476-483.

[90] ENESCU, M., HEINRICH, M. P., HILL, E., SHARMA, R., CHAPPELL, M. A. & SCHNABEL, J. A. 2014. An MRF-based discrete optimization framework for combined DCE-MRI motion correction and pharmacokinetic parameter estimation. *Bayesian and grAphical Models for Biomedical Imaging.* Springer.

[91] SLOAN, J. M., GOATMAN, K. A. & SIEBERT, J. P. 2018. Learning rigid image registration-utilizing convolutional neural networks for medical image registration.

[92] LONG, J., SHELHAMER, E. & DARRELL, T. Fully convolutional networks for semantic segmentation. Proceedings of the IEEE conference on computer vision and pattern recognition, 2015. 3431-3440.

[93] DE VOS, B. D., BERENDSEN, F. F., VIERGEVER, M. A., STARING, M. & IŠGUM, I. 2017. End-to-end unsupervised deformable image registration with a convolutional neural network. *Deep Learning in Medical Image Analysis and Multimodal Learning for Clinical Decision Support.* Springer.

[94] JADERBERG, M., SIMONYAN, K., ZISSERMAN, A. & KAVUKCUOGLU, K. J. A. P. A. 2015. Spatial transformer networks.

[95] SHAN, S., YAN, W., GUO, X., CHANG, E. I., FAN, Y. & XU, Y. J. A. P. A. 2017. Unsupervised end-to-end learning for deformable medical image registration.

[96] DOSOVITSKIY, A., FISCHER, P., ILG, E., HAUSSER, P., HAZIRBAS, C., GOLKOV, V., VAN DER SMAGT, P., CREMERS, D. & BROX, T. Flownet: Learning optical flow with convolutional networks. Proceedings of the IEEE international conference on computer vision, 2015. 2758-2766.

[97] BALAKRISHNAN, G., ZHAO, A., SABUNCU, M. R., GUTTAG, J. & DALCA, A. V. An Unsupervised Learning Model for Deformable Medical Image Registration. Proceedings of the IEEE Conference on Computer Vision and Pattern Recognition, 2018. 9252-9260.

[98] RONNEBERGER, O., FISCHER, P. & BROX, T. U-net: Convolutional networks for biomedical image segmentation. International Conference on Medical image computing and computer-assisted intervention, 2015. Springer, 234-241.

[99] LI, H. & FAN, Y. Non-rigid image registration using self-supervised fully convolutional networks without training data. 2018 IEEE 15th International Symposium on Biomedical Imaging (ISBI 2018), 2018. IEEE, 1075-1078.

[100] EPPENHOF, K. A., LAFARGE, M. W., MOESKOPS, P., VETA, M. & PLUIM, J. P. Deformable image registration using convolutional neural networks. Medical Imaging 2018: Image Processing, 2018. International Society for Optics and Photonics, 105740S.

[101] SIMONYAN, K. & ZISSERMAN, A. J. A. P. A. 2014. Very deep convolutional networks for large-scale image recognition.

[102] CHEN, X., DIAZ-PINTO, A., RAVIKUMAR, N. & FRANGI, A. J. P. I. B. E. 2020. Deep learning in medical image registration.

[103] HOCKINGS, P., SAEED, N., SIMMS, R., SMITH, N., HALL, M. G., WATERTON, J. C. & SOURBRON, S. 2020. MRI Biomarkers. *In:* SEIBERLICH, N., GULANI, V., CALAMANTE, F., CAMPBELL-WASHBURN, A., DONEVA, M., HU, H. H. & SOURBRON, S. (eds.) *Advances in Magnetic Resonance Technology and Applications.* Academic Press.

[104] ZÖLLNER, F. G., ŠERIFOVIĆ-TRBALIĆ, A., KABELITZ, G., KOCIŃSKI, M., MATERKA, A., ROGELJ, P. J. M. R. M. I. P., BIOLOGY & MEDICINE 2020. Image registration in dynamic renal MRI—current status and prospects. 1-16.

[105] BERISHA, S., HAN, J., SHAHID, M., HAN, Y. & WITSCHEY, W. R. J. P. O. 2016. Measurement of myocardial T1ρ with a motion corrected, parametric mapping sequence in humans. 11**,** e0151144.

[106] MIRZAALIAN, H., SAAD, A. & HAMARNEH, G. Iterative segmentation and motion correction for dynamic PET images based on radioactive tracer kinetics. 2012 IEEE Workshop on Mathematical Methods in Biomedical Image Analysis, 2012. IEEE, 265-270.

[107] RAMOS-LLORDEN, G., DEN DEKKER, A. J., VAN STEENKISTE, G., JEURISSEN, B., VANHEVEL, F., VAN AUDEKERKE, J., VERHOYE, M. & SIJBERS, J. 2017. A Unified Maximum Likelihood Framework for Simultaneous Motion and T_{1} Estimation in Quantitative MR T_{1} Mapping. *IEEE Trans Med Imaging,* 36**,** 433-446.

[108] COLL-FONT, J., AFACAN, O., CHOW, J. S., LEE, R. S., WARFIELD, S. K. & KURUGOL, S. J. M. I. A. 2020. Modeling dynamic radial contrast enhanced MRI with linear time invariant systems for motion correction in quantitative assessment of kidney function. 67**,** 101880.

[109] JIAO, J., BOUSSE, A., THIELEMANS, K., BURGOS, N., WESTON, P. S., SCHOTT, J. M., ATKINSON, D., ARRIDGE, S. R., HUTTON, B. F. & MARKIEWICZ, P. J. I. T. O. M. I. 2016. Direct parametric reconstruction with joint motion estimation/correction for dynamic brain PET data. 36**,** 203-213.

[110] DE BOER, A., HARTEVELD, A. A., STEMKENS, B., BLANKESTIJN, P. J., BOS, C., FRANKLIN, S. L., FROELING, M., JOLES, J. A., VERHAAR, M. C. & VAN DEN BERG, N. J. J. O. M. R. I. 2020. Multiparametric Renal MRI: An Intrasubject Test–Retest Repeatability Study.

[111] Parameter file database. Available: http://elastix.bigr.nl/wiki/index.php/Par0039 [Accessed].

[112] PATHAK, R., RAGHEB, H., THACKER, N. A., MORRIS, D. M., AMIRI, H., KUIJER, J., DESOUZA, N. M., HEERSCHAP, A. & JACKSON, A. J. S. R. 2017. A data-driven statistical model that estimates measurement uncertainty improves interpretation of ADC reproducibility: a multi-site study of liver metastases. 7**,** 1-10.

[113] CALLAGHAN, M. F., JOSEPHS, O., HERBST, M., ZAITSEV, M., TODD, N. & WEISKOPF, N. 2015. An evaluation of prospective motion correction (PMC) for high resolution quantitative MRI. *Front Neurosci,* 9**,** 97.

[114] HAO, L., HUANG, Y., GAO, Y., CHEN, X. & WANG, P. 2017. Nonrigid Registration of Prostate Diffusion-Weighted MRI. *J Healthc Eng,* 2017**,** 9296354.

[115] JANSEN, M. J. A., KUIJF, H. J., VELDHUIS, W. B., WESSELS, F. J., VAN LEEUWEN, M. S. & PLUIM, J. P. W. 2017. Evaluation of motion correction for clinical dynamic contrast enhanced MRI of the liver. *Phys Med Biol,* 62**,** 7556-7568.

[116] XIANG, C., ANDRES, D.-P., NISHANT, R. & ALEJANDRO, F. 2020. Deep learning in medical image registration. *Progress in Biomedical Engineering*.